ABSTRACT

Title of dissertation: ON THE GENESIS AND PREDICTABILITY OF HURRICANE JULIA (2010)

Stefan Francis Cecelski, Doctor of Philosophy, 2014

Dissertation directed by: Professor Da-Lin Zhang
Department of Atmospheric and Oceanic Science

Tropical cyclogenesis (TCG) continues to be one of the least understood processes in tropical meteorology today. While a robust theoretical framework for TCG within African Easterly Waves (AEWs) has recently been developed, little work explores the mesoscale processes and interactions with the AEW during TCG. This study investigates the TCG of Hurricane Julia from the 2010 north Atlantic hurricane season using a series of high-resolution model simulation with the finest grid size of 1 km. In addition to a control simulation used to study the mesoscale processes during TCG, 20 ensemble simulations are conducted to identify key dynamical and thermodynamical processes taking place during TCG. These ensembles also serve to quantify the predictability of TCG while determining the processes responsible for ensemble solution disagreements.

It is found that the TCG of Hurricane Julia is triggered by the pronounced upper-tropospheric warming associated with organized deep convection. The upper-level warming is able to intensify and become a meso-α-scale feature due to a storm-scale outflow beyond the Rossby radius of deformation. The simulation confirms

previous ideas by demonstrating that the intersection of the AEW's trough axis and critical latitude is a preferred location for TCG, while supplementing such work by illustrating the importance of upper-tropospheric warming and meso-α-scale surface pressure falls during TCG. Ensemble simulations further elaborate on the mechanisms by depicting substantial parametric differences between the stronger and weaker members. The dominant pattern of mean sea-level pressure (MSLP) ensemble differences is associated with the intensity of the pre-tropical depression (pre-TD), explaining nearly half of the total variance at the time of TCG. Similar patterns of differences are found for the low-level absolute vorticity and upper-tropospheric temperature anomalies.

An additional sensitivity simulation removing the latent heat of fusion associated with deposition results in significant changes to the TCG process. It is shown that the fusion heating occurring during deposition is important for the upper-tropospheric thermodynamic changes occurring during TCG and thus, yields fundamental changes to structure and intensity of deep convection. Overall, removing fusion heating from deposition results in a weaker MSLP disturbance and one that is not self-sustaining.

ON THE GENESIS AND PREDICTABILITY OF HURRICANE JULIA (2010)

by

Stefan Francis Cecelski

Dissertation submitted to the Faculty of the Graduate School of the
University of Maryland, College Park in partial fulfillment
of the requirements for the degree of
Doctor of Philosophy
2014

Advisory Committee:
Professor Da-Lin Zhang, Chair/Advisor
Dr. Takemasa Miyoshi, Co-Advisor
Professor Kayo Ide, Co-Advisor
Professor Xin-Zhong Liang
Professor James Carton
Professor Kaustubh Agashe, Dean's Representative

Dedication

My thesis is dedicated to my father, Mark Cecelski, my mother, Kim Cecelski, and my sister, Rachel Cecelski. You have been nothing but supportive and proud of me since I began my academic endeavors.

Any struggles I have had during my academics pale in comparison to what my father has been through. It is his strength, passion, hope, and love that kept me pressing forward through any tough times in my life. I love you, dad, and am proud to be your son.

Whenever I would feel discouraged during my doctoral work, I'd think of my mother. She has always been there for me, helped me stay the course, and has been nothing but the best mother a son could ask for. I love you, mom.

I'd also like to dedicate this work to my grandparents, Dorothy and Arthur Cecelski, and Stanley and Hovey Klainer. I know that Dorothy, Arthur and Stanley would have given anything to be here for this moment.

My thesis is also dedicated to Christina Liaskos for all of her help and support through my doctoral work. I am truly lucky to have her in my life.

Ending things on a happier note, I also dedicate this body of work to my rabbit, Rayleigh. While I slaved away at my desk the past five years, he was sitting right behind me waiting for me to be done. I'm done now buddy!

Acknowledgments

The most influential, and by far, greatest supporter of the work encapsulated herein is my adviser, Professor Da-Lin Zhang. I am forever indebted to him for the countless hours of revisions, advice, and ideas that helped make this research possible. His passion for his research and his students is unmatched, and has certainly been a motivator through the ups and downs of my journey through doctoral research. I have learned so much from Da-Lin. Not only did he advise my doctoral work, he has prepared me for a prosperous and successful career for what lies beyond graduate school. Thank you Dr. Zhang, for all that you have done for me.

I would also like to thank Dr. Takemasa Miyoshi for his help in making a large portion of this research possible. His ideas and advice helped tremendously when preparing and creating the high-resolution ensemble forecasts of my research.

Finally, I would like thank the National Aeronautics and Space Administration (NASA) for funding my research. The generosity of the Earth and Space Science Fellowship enabled the scientific discoveries in various ways, including funding and computational resources. Without the computational resources obtained through NASA, none of my research would have been possible. This work was supported by NASA Headquarters under the NASA Earth and Space Science Fellowship Program - Grant NNX11AP29H and NASA's Grant NNX12AJ78G. The numerical weather simulations were performed at the NASA High-End Computing Program through the NASA Center for Climate Simulation at Goddard Space Flight Center.

Table of Contents

List of Tables

List of Figures

List of Abbreviations

α	alpha
β	beta
η	eta (used for absolute vorticity)
γ	gamma

AEW	African Easterly Wave
BC	Boundary Condition
CAPE	Convective Available Potential Energy
CB	Convective Burst
CIN	Convective Inhibition
CRTM	Community Radiative Transfer Model
EOF	Empirical Orthogonal Function
ERA–Interim	European Centre for Medium-Range Weather Forecasts Re-Analysis
GDAS	Global Data Assimilation System
GRIP	Genesis and Rapid Intensification Processes Project
H	Scale Height
IC	Initial Condition
IR	Infrared
ITCZ	Intertropical Convergence Zone
JMA	Japan Meteorological Agency
LETKF	Local Ensemble Transform Kalman Filter
LLV	Low-level Vortex
$\mathrm{L_R}$	Rossby Radius of Deformation
MCS	Mesoscale Convective System
MCV	Mesoscale Convective Vortex
MDR	Main Development Region
MSLP	Mean Sea-level Pressure
NAMMA	NASA African Monsoon Multi-disciplinary Analyses
NCEP	National Centers for Environmental Prediction
NHC	National Hurricane Center
NOAA	National Oceanic and Atmospheric Administration
NWP	Numerical Weather Prediction
OI	Optimal Interpolation
$\mathrm{P_{MIN}}$	Minimum Central Mean Sea-level Pressure
PBL	Planetary Boundary Layer
PC	Principal Component
PREDICT	Pre-Depression Investigation of Cloud-systems in the Tropics Project
Pre-TD	Pre-tropical Depression
PV	Potential Vorticity
PW	Precipitable Water
RH	Relative Humidity
RRTM	Rapid Radiative Transfer Model
SI	Significant Intensification

SST	Sea-surface Temperature
TC	Tropical Cyclone
TCG	Tropical Cyclogenesis
TD	Tropical Depression
TRMM	Tropical Rainfall Measuring Mission
TS	Tropical Storm
UPP	Unified Post Processor
V_{MAX}	10-meter maximum sustained wind speed
VHT	Vortical Hot Tower
VWS	Vertical Wind Shear
WISHE	Wind-induced Surface Heat Exchange
WPS	Weather Research and Forecasting Model Pre-processor
WRF	Weather Research and Forecasting Model
WSM	Weather Research and Forecasting Single-Moment Microphysics Scheme
YSU	Yonsei University

Chapter 1: Introduction

Tropical cyclogenesis (TCG), the transition of a non-developing tropical disturbance into a developing one, continues to be one of the least understood processes in tropical meteorology today. The formation of tropical depressions (TDs), which under favorable conditions grow into tropical storms (TSs), has many different routes, ranging from large-scale attributes such as African Easterly Waves (AEWs) to small-scale features taking place in mesoscale convective systems (MCSs). In particular, roughly 20% of tropical waves in the north Atlantic and eastern Pacific basin become TSs (Frank 1970). Our ability to distinguish the 20% of developing disturbances from the remaining non-developing disturbances in terms of factors responsible for their development is limited due partly to the lack of high-resolution observations at the birthplace and partly to the deficiencies in current numerical weather prediction models. Numerous theories exist to describe the multi-scale interactions that take place during TCG, but unfortunately, it has not been until recently that such theories could be validated with field campaigns and high-resolution models.

1.1 Dynamics and thermodynamics of tropical cyclogenesis

Previous studies have referred to TCG as a two-stage problem: a) the preconditioning of a meso-α and synoptic environment and b) the construction and organization of a meso-β-scale tropical cyclone (TC) vortex (Karyampudi and Pierce 2002; Wang et al. 2010a). While these two stages might seem disjoint, they actually can occur simultaneously. The first stage involves the general environmental characteristics being favorable, such as weak vertical wind shear (VWS), warm sea surface temperatures (SSTs), sufficient column moisture content and a low-level cyclonic rotation (Gray 1968). A vast number of synoptic-scale phenomena can provide favorable conditions for the development of TDs, ranging from equatorial waves (Schreck et al. 2012) to westerly wind bursts (Hogsett and Zhang 2010), intertropical convergence zone (ITCZ) breakdowns (Kieu and Zhang 2009), monsoon depressions (Harr et al. 1996), and AEWs (Dunkerton et al. 2009; Vizy and Cook 2009). The north Atlantic basin is dominated by storms forming from AEWs in the main development region (MDR), even though a slim number of AEWs spawn named TSs.

A growing number of previous studies have attempted to examine the second stage of TCG with higher quality observations and modeling data. Recent studies in the Atlantic and east Pacific basins have found an intimate relationship between TCG and AEWs (Dunkerton et al. 2009; Montgomery et al. 2010; Vizy and Cook 2009; Wang et al. 2010a) and conclude that AEWs appear to be a common type of precursor disturbances for north Atlantic TCs. However, such formation is still somewhat a mystery given the lack of understanding of multi-scale interactions taking place during TCG. The role of the AEW has recently been shifted to “parent”, incubating the growth of mesoscale convective vortices (MCVs) (Dunkerton et al. 2009). The concept revolves around the notion that the pre-depression perturbation is protected dynamically from adverse environmental conditions such as dry air or large VWS.

This theory has been further advanced by the marsupial pouch paradigm (Dunkerton et al. 2009; Montgomery et al. 2010; Wang et al. 2010a), which succinctly theorizes the preferred TCG location within an AEW. For this location to be identified using the paradigm, the AEW must be put into a co-moving reference frame in which the intersection of its trough axis with its critical latitude, defined as the latitude where the zonal wind equals the phase speed of the AEW, marks the AEW’s approximate pouch center and the preferred location for development. Mesoscale perturbations that can enter this area defined by the pouch can undergo favorable development, thus providing a link between the AEW and the mesoscale perturbations. The depth and vertical alignment of the pouch is also important for development, as shown by Wang et al. (2012). Since the horizontal structure and center of the pouch depend on the phase speed of the AEW, the variance of this phase speed with height has significant implications on the growth of disturbance.

While the role of the AEW in TCG has been well described via the marsupial pouch paradigm, the links between the AEW and mesoscale perturbations have been less described in the literature. It has been hypothesized that the low-level critical latitude of an AEW is a preferred location for mesoscale development (Dunkerton et al. 2009). This postulation has been investigated in limited fashion, but recent work has shown promising results on the multi-scale interactions taking place during TCG (e.g., Braun et al. 2013; Montgomery et al. 2012; Wang et al. 2010a,b).

Other studies have focused on AEWs and their complex structures in relation to TCG. These structures include dynamical instabilities (Berry and Thorncroft 2005; Burpee 1972), wave structures (Burpee 1972; Hopsch et al. 2010; Thorncroft and Hodges 2000) and convective development within AEWs, e.g., convectively generated potential vorticity (PV) anomalies (Berry and Thorncroft 2005). It has been found that distinct differences between developing and non-developing AEWs include tropospheric moisture content, low-level vorticity growth and the strength (and persistence) of deep convection within the AEW (Hopsch et al. 2010). Additionally, Wang et al. (2012) have shown that a coherent vertical structure is an important discriminating factor between developing and non-developing AEWs. The characteristics of developing versus non-developing waves lend insight into whether or not the waves are able to protect and sustain developing low-level vortices (hereafter LLVs) into TDs. The LLV is defined herein, following Zhang and Fritsch (1987), as significant concentration of cyclonic vorticity of at least the order of magnitude of the local Coriolis parameter.

The meso-β-scale low-level cyclonic vorticity development during TCG has been described by both the top-down (Bister and Emanuel 1997; Ritchie and Holland 1997) and bottom-up paradigms (Hendricks et al. 2004; Montgomery et al. 2006; Zhang and Bao 1996), contrasting each other in how low-level cyclonic vorticity arises. Within the top-down theory, the low-level cyclonic circulation is an extension of a preexisting mid-tropospheric cyclonic vortex, which may be reconstituted downward to create the surface circulation. The bottom-up theory suggests that the low-level vorticity is spun up via deep convection, which through up-scale aggregation, becomes an LLV. The bottom-up theory has been invigorated with the concept of vortical hot towers (VHTs), which were first identified by Riehl and Malkus (1958) as "hot towers" and further conceptualized by Simpson et al. (1998) as non-rotating protected deep convective cores. Hendricks et al. (2004) and Montgomery et al. (2006) revived VHTs with the addition of vortex-tube stretching in a rotating environment. This augmentation to the bottom-up theory allows for VHTs to be the "building blocks for TCG", in which individual VHTs can conglomerate to create or enhance the LLV. Recently, both modeling and observational studies alike have been able to elaborate on VHTs and their role in TCG (Hendricks et al. 2004; Houze et al. 2009; Montgomery et al. 2006; Sippel et al. 2006).

1.2 Predictability of tropical cyclogenesis

While there have been improvements in producing forecasts of mature TCs, virtually no improvements have been made in the prediction of TCG. More effort has been given for improving the track and intensity forecast errors of a mature TC using ensembles. These methods, unfortunately, have not been extended to forecast TCG in any robust operational manner. Previous work has demonstrated that moist convection has the highest uncertainty at all time and spatial scales in numerical weather prediction (NWP) models when compared to other precipitation processes

(Olson et al. 1995). Unfortunately, the underlying dynamics of TCG is cemented in moist convective processes (Hendricks et al. 2004; Montgomery et al. 2006) and thus, the predictability of TCG is rooted in the predictability of moist convection.

While the majority of the previous discussion has elaborated upon TCG through modeling and observational studies, very little work has investigated TCG using a particular niche of modeling studies: ensemble simulations. A notable study of Sippel and Zhang (2008), who conducted short-range ensemble forecasts on a non-developing tropical disturbance in the Gulf of Mexico during the 2004 North Atlantic hurricane season, assessed the differences between ensemble members using a linear correlation to generate statistical sensitivities of storm intensity changes to specific meteorological parameters. Dynamical differences between ensemble members were then inferred from these sensitivities. The work discovered that the presence of deep moisture and high convective available potential energy (CAPE) are the two most important factors in the initial conditions (ICs), which combine to yield a more active spin-up in the first 6-12 h of integration. Beyond this spin-up period, they demonstrated that the ensemble spread increased due to differences in convection and the wind-induced surface heat exchange (WISHE; Emanuel et al. 1994) mechanism that some members utilized. Snyder et al. (2010) investigated the National Centers for Environmental Prediction (NCEP) global ensemble forecast system in predicting the TCG and evolution of five TCs and two non-developing systems during the NASA African Monsoon Multidisciplinary Analyses (NAMMA). They found that the ensemble system predicted TCG of three strong storms that formed within AEWs, but failed to predict TCG for two weaker storms. Their study suggested that the accuracy of TCG forecasts from the global ensemble was 50% for forecasts initialized in the pre-genesis phase. In addition, Enomoto et al. (2010) found that the ensemble spread increased prior to TCG, as the ensemble solutions diverged in the intensity and timing of TCG.

Obviously, a statistical approach to making inferences on the dynamics and thermodynamics (e.g., surface changes) of TCG can provide a more holistic view of the ensemble forecasts. Sippel and Zhang (2008) employed a linear correlation analysis, following Hawblitzel et al. 2007, to generate statistical sensitivities of mean sea-level pressure (MSLP) changes and isolated variables that are responsible dynamically for the changes. More recently, studies have used ensemble sensitivity analyses (Ancell and Hakim 2007; Chang et al. 2013; Gombos et al. 2012; Torn and Hakim 2008; Zheng et al. 2013) to examine how a particular forecast metric depends on the ICs. Ensemble sensitivity uses a linear correlation between a chosen forecast metric and selected meteorological parameters to generate a statistical sensitivity of the forecast metric for previous forecast times and the ICs. Instead of using just an individual ensemble member, the analysis is able to use all ensemble members, yielding the ability to make inferences about what meteorological parameters the whole complement of ensemble forecasts are sensitive to. Ensemble sensitivity has been shown to be useful in short and medium range forecasts for mid-latitude applications (Chang et al. 2013; Zheng et al. 2013) as well as TC track forecasts (Gombos et al. 2012), even with the assumption of linearity. The selection of a forecast metric has varied across previous studies, ranging from selecting particular cyclone parameters (e.g., MSLP) to the principal components (PCs) of empirical orthogonal functions (EOFs), whose use has produced promising results (Chang et al. 2013; Gombos et al. 2012; Zheng et al. 2013). Recently, the use of ensemble sensitivity analyses via EOFs was extended by Torn and Cook (2013) for two TCG cases from the 2010 north Atlantic hurricane season. Their results depicted that the forecasts of TCG were sensitive to select, but different parameters. The first storm investigated, Danielle, was most sensitive to upper-level divergence and deep-layer (e.g., 850-200 hPa) VWS. In contrast, the second storm, Karl, was more sensitive to a coherent large-scale vortex structure in addition to a sensitivity to the magnitude of VWS. Such differences between two storms in the same hurricane season truly depict the complexity in understanding TCG and related processes across all spatial and time scales.

1.3 Objectives of this research

Our work herein focuses on investigating the AEW, multi-scale interactions, and mesoscale processes associated with TCG. Additionally, we investigate the predictability of TCG and what mechanisms are likely to dictate the predictability of a given TCG event. These topics for investigation are critical for understanding TCG more thoroughly and represent significant gaps in our current understanding. Specifically, our work aims to fill in the gaps on the current knowledge of TCG with the following overarching goals:

(i) Investigate the role of the AEW, mesoscale disturbances, and their interactions during tropical cyclogenesis in the context of the marsupial pouch paradigm;

(ii) Explore the connections between MSLP falls, low-level vorticity development, deep convection, the AEW, and upper-tropospheric processes;

(iii) Study the dominant mechanisms (e.g., triggers) that cause tropical cyclogenesis to occur;

(iv) Investigate the sensitivity of tropical cyclogenesis to ice cloud microphysics.

We explore the genesis of Hurricane Julia from the 2010 north Atlantic hurricane season to investigate the aforementioned goals. This storm represents a complex TCG case within an strong AEW, enabling the investigation of mesoscale processes within the protective nature of the AEW under the marsupial pouch paradigm. Naturally, our selection of this storm is influenced by the large collection observational data obtained through Genesis and Rapid Intensification Processes (GRIP; Braun et al. 2013) and the Pre-Depression Investigation of Cloud-systems in the Tropics (PREDICT; Montgomery et al. 2012), two major observational campaigns that occurred during the 2010 north Atlantic hurricane season. The objectives are achieved through the analysis of observational data, and most importantly, multiple 66-h cloud-resolving simulations of Julia during its pre-tropical depression (pre-TD) stage using the Weather Research and Forecasting (WRF; Skamarock et al. 2005) model with the finest 1-km horizontal resolution.

To achieve the goals, the following methods and objectives are used to examine the genesis of Hurricane Julia:

(i) Generate a high-resolution WRF simulation on the genesis of Hurricane Julia to:

  - Document the large-scale environments, including the SST distribution, VWS, cloud distribution, and the life cycle of the AEW, and the evolution of Hurricane Julia;
  - Analyze the development of meso-α-scale surface pressure falls and an LLV leading to TD Julia within an AEW;
  - Document the dynamic and thermodynamic changes to the upper troposphere during tropical cyclogenesis;
  - Demonstrate the interconnectedness of the AEW, deep convection, upper troposphere, surface pressure falls and the LLV during tropical cyclogenesis.

(ii) Create high-resolution ensemble forecasts on the tropical cyclogenesis of Hurricane Julia using the coupled WRF and local ensemble transform Kalman filter (LETKF) system (Hunt et al. 2007; Miyoshi and Kunii 2012) to:

  - Compare the ensemble forecasts with the control and observations;
  - Identify the fundamental synoptic-scale and mesoscale differences between developing and non-developing ensemble members with an emphasis on upper-level warming, the outflow layer, and convective development.
  - Quantify the disagreements between the ensemble members for several parameters such as MSLP, the upper-tropospheric outflow layer, and deep convection.
  - Use a series of EOFs to isolate the parametric patterns of ensemble vari-

ance for MSLP and low-level absolute vorticity;

  - Calculate ensemble sensitivities to provide statistical inferences about which meteorological processes might be responsible for the MSLP differences with a focus on upper-tropospheric thermodynamic changes versus WISHE;
  - Identify the dominant ensemble forecast patterns for disagreement of upper-tropospheric thermal anomalies
  - Diagnose the sensitivity of upper-tropospheric temperature variance to the upper-tropospheric divergent outflow layer and deep convection;
  - Analyze the ensemble variability of deep convection.

(iii) Conduct high-resolution microphysics sensitivity WRF simulations on the tropical cyclogenesis of Hurricane Julia to:

  - Determine the importance of depositional heating for the development of upper-tropospheric warming during TCG;
  - See to what extent homogeneous freezing contributes to the upper-tropospheric warming taking place during TCG;
  - Diagnose what impacts, if any, the changes in cloud microphysics has on the evolution of deep convection and the vertical motion field when compared to the control.

The thesis is organized as follows. Chapter 2 depicts the results on the genesis of Hurricane Julia utilizing a high-resolution control simulation to investigate the role of the AEW during TCG in addition to the evolution of mesoscale processes. Chapter 3 expands upon the results of chapter 2 by investigating TCG using the results of high-resolution ensemble forecasts on the TCG case. Chapter 4 elaborates on the sensitivity of TCG to ice cloud microphysics. Most of the above materials are re-organized based on the publications of Cecelski and Zhang (2013), Cecelski et al. (2014a), and Cecelski and Zhang (2014b). Some concluding remarks and future work are given in the final chapter.

Chapter 2: Genesis of Hurricane Julia

2.1 Storm overview

The National Hurricane Center (NHC) declared Julia a TD at 0600 UTC 12 September 2010 (hereafter 12/0600). Six hours after gaining TD status, Julia quickly became a TS. The genesis came as a surprise to NHC forecasters even with long-range guidance depicting Julia's formation several days prior (Beven and Landsea 2010). Hurricane Julia was the strongest north Atlantic hurricane east of 40°W when it reached a central minimum MSLP ($\mathrm{P_{MIN}}$) of 948 hPa at 15/1200. Even with this remarkable statistic, Hurricane Julia was a small, compact storm that was dwarfed by the much larger Hurricane Igor, which formed just days prior. Both storms took place during the GRIP and the PREDICT projects, which provided initial analysis resources for the investigation of Hurricane Julia from its pre-TD stage. The AEW that Julia formed within could be traced back to 8/0000 (96 h prior to genesis) as a well-defined circulation using 600-hPa relative vorticity (Fig. 2.1). The westward progression of the wave is estimated to have an average phase speed (C_p) of 8.0 m s^{-1}, which is used for the co-moving frame of reference for the rest of this investigation. The selection of this phase speed is calculated using the 600-hPa

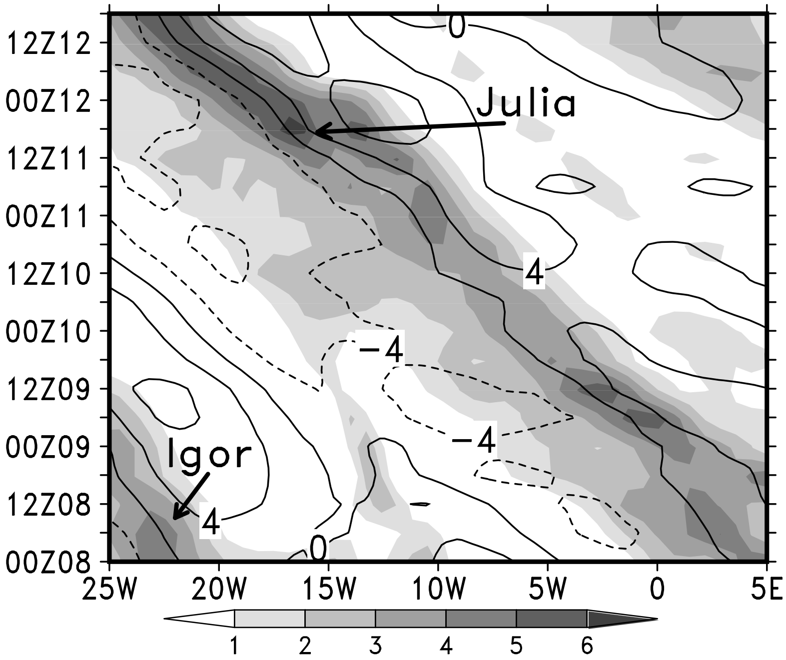

Figure 2.1: Hovmöller diagram of ERA-Interim 600-hPa relative vorticity (shaded, $\times 10^{-5}$ s^{-1}) and meridional wind (contoured at intervals of 4 m s^{-1}) averaged between 8° and 13°N during the period of 0000 UTC 8 - 1800 UTC 12 Sep 2010. The phase speed of the AEW is estimated as C_p = -8.0 m s^{-1}. "Julia" and "Igor" mark the cyclonic vorticity associated with Hurricanes Julia and Igor, respectively.

cyclonic vorticity Hovmöller analysis (Fig. 2.1) in conjunction with similar analyses from the WRF data (not shown). The most persistent closed circulation in the co-moving frame was found at 600 hPa, and thus, is level used for the phase speed calculation of the AEW. We define TCG as the time when the NHC declares Julia a TD in conjunction with satisfying the condition of a closed MSLP isobar on a standard 4 hPa contouring interval of sufficient size. The "sufficient size" constraint reassures that we don't declare TCG prematurely as a transient mesoscale feature with a closed isobar.

Hurricane Igor developed in close proximity to Julia, becoming a TD at 08/0600 (Fig. 2.1). An examination of Rossby wave energy dispersion using methods similar to Li and Fu (2006a) and Li et al. (2006b) indicates little impact of Igor on the genesis of Julia (not shown). Given the strength of the AEW, it is not surprising that Hurricane Igor did not produce significant impact on the genesis of Julia. Perhaps its only possible impact on the TCG of Julia involved oceanic upwelling causing cooler waters to the south-southeast of the Cape Verde Islands.

At 10/0000, the AEW exhibited a vertically tilted closed circulation in the co-moving frame as demonstrated by the circulation centers in Fig. 2.2. Namely, the circulation center at 600 hPa ("X") is seen being displaced well eastward from the upper-tropospheric circulation center ("X_{400}") where the cyclonic relative vorticity is maximized (Fig. 2.2b). Its closed circulation is identifiable down to 825 hPa ("X_{825}") with an open circulation below. The horizontal distance between the upper-tropospheric circulation ("X_{400}") and the lower-tropospheric disturbance ("X_{825}") is over 400 km, a testament to the complexity of the wave. The maximum cyclonic vorticity near 400 hPa is substantially higher than what has been previously observed for AEWs, which usually display maximum between 600 and 700 hPa for AEWs equator-ward of 15°N (Thorncroft and Hodges 2000). The westward tilt with height of the vorticity structure is accompanied by a similar thermodynamic profile, as marked the "W" ("C") representing the warming (cooling) above (beneath) the tilted cyclonic vorticity maximum (Fig. 2.2b). The 600-hPa cyclonic vorticity is mainly due to horizontal shear on the southern side of an African easterly jet ("AEJ", Fig. 2.2a,c). Baroclinic and barotropic instability can be inferred from the reversal in the meridional PV gradient maximized near 400 hPa and to a lesser extent in the lower troposphere (Burpee 1972; Charney and Stern 1962). The combined baroclinic-barotropic instability on the synoptic scale appears to be favorable for the amplification of any mesoscale disturbance within the AEW.

The AEW under study moved due west over the 54-h period prior to TCG, traversing over the Guinea Highlands before heading over the eastern north Atlantic ocean (Fig. 2.3). Before its coastal passage, the AEW was dominated by sporadic weak convection (Fig. 2.4a) which quickly aggregated to become a large MCS as it completely moved over water at 11/1200 (Fig. 2.4b). Concurrently, the Dakar (GOOY) rawinsonde showed strong easterly winds in excess of 25 m s^{-1} from 925 to 700 hPa (not shown) as the wave and related convection strengthened during passage. Julia quickly formed within the AEW, becoming a TD only 18 h after the wave traversed the west African coastline. By the TCG time the MCS evolved further, exhibiting a cyclonic cloud pattern (Fig. 2.4c) and a much more TS-like storm by 18/1200 (Fig. 2.4d).

Such a short period from wave to TD has also been noted by Hopsch et al. (2010), who found that fast TCG from easterly waves have higher tropospheric moisture content and larger low-level cyclonic vorticity than those of non-developing waves during coastal passage. A 500 km × 500 km area-averaged time series surrounding the storm center, given in Fig. 2.5, shows that Julia's formation is consistent with the characteristics of fast TCG from an AEW. The simulated pre-TD is initially tracked using the 600- and 700-hPa circulation in the co-moving framework with large absolute vorticity and later using the P_{MIN} center when a mesolow

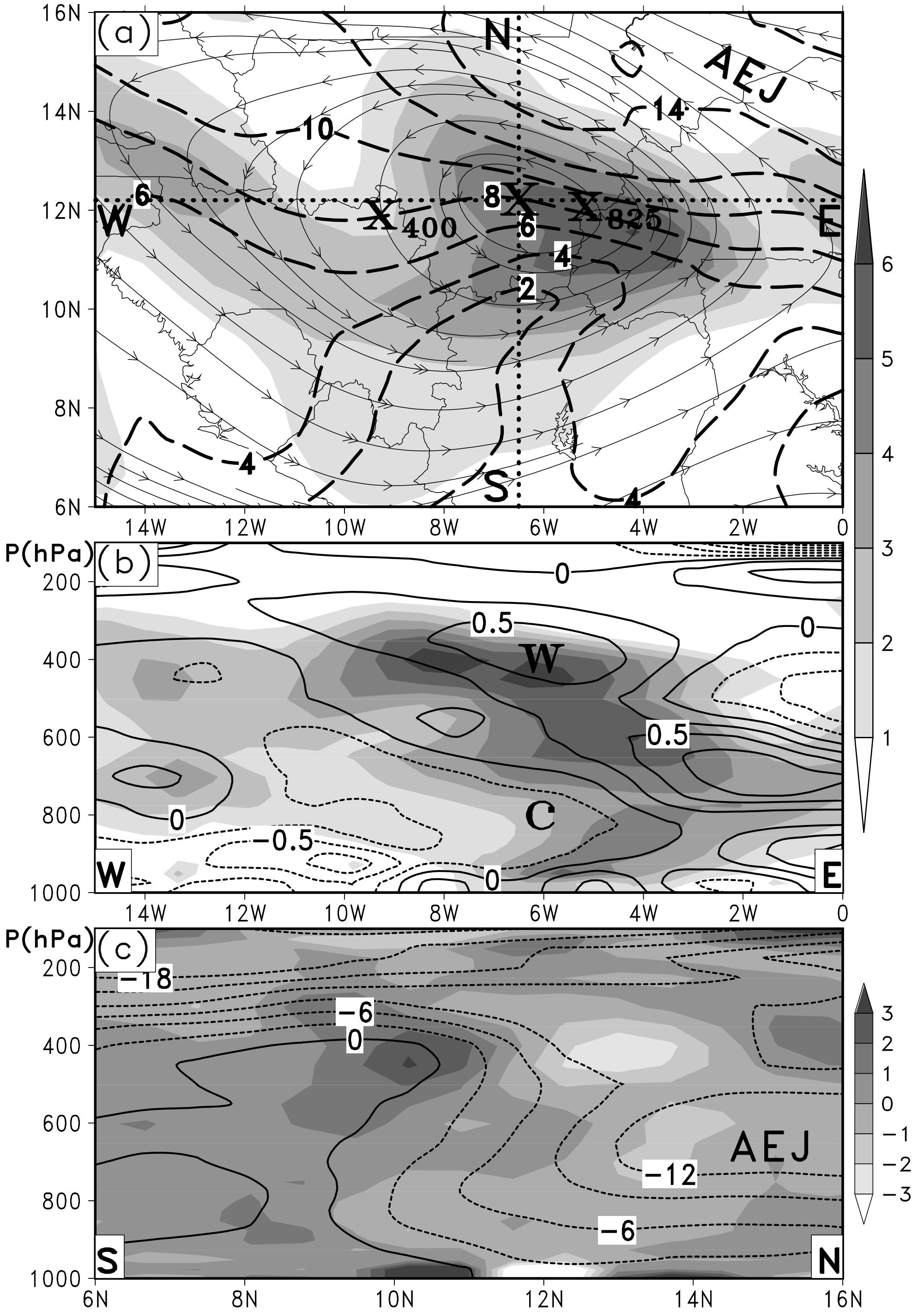
(a)
N
S
W
E
AEJ
X
X400
X825
14
10
8
6
4
2
16N
14N
12N
10N
8N
6N
14W
12W
10W
8W
6W
4W
2W
0
(b)
P(hPa)
W
C
0
0.5
-0.5
200
400
600
800
1000
(c)
-18
-6
0
-12
AEJ
S
N
6N
8N
10N
12N
14N
16N
1
2
3
4
5
6
3
2
1
0
−1
−2
−3

Figure 2.2: (a) ERA-Interim 600-hPa relative vorticity (shaded, $\times 10^{-5}$ s^{-1}), zonal wind (contoured at intervals of 2 m s^{-1}), and co-moving streamlines valid at 0000 UTC 10 Sep. "X" represents the intersection point of the 600-hPa trough axis and critical latitude. "X_{400}" and "X_{825}" represent the locations of the AEW circulation centers at 400 and 825 hPa. The dotted lines marked by W-E and S-N represent vertical cross sections shown in (b) and (c). The approximate location of the African easterly jet is marked by "AEJ". (b) Vertical cross section of cyclonic relative vorticity (shaded, $\times 10^{-5}$ s^{-1}) and temperature deviation (contoured at intervals of 0.25°C). The temperature deviation is calculated as the difference from the mean temperature at each respective level. The peak warmth and coldness associated with the AEW are marked with "W" and "C", respectively. (c) Vertical cross section of meridional potential vorticity gradient (shaded, $\times 10^{-12}$ m s^{-1} K kg^{-1}) and zonal wind (contoured at intervals of 4 m s^{-1}). AEJ represents the location of the African easterly jet.

becomes traceable. Specifically, precipitable waters (PW, Fig. 2.5a) steadily increased as the wave progressed off shore, with the strongest rises occurring when the storm is completely over water after 11/1200. Deep-layer VWS (850-200 hPa layer) weakened during the period and remained under 6 m s^{-1} for the 36 h leading up to TCG (VWS, Fig. 2.5a). Post-genesis, VWS increased again to above 8 m s^{-1}, possibly limiting the intensification of Julia somewhat. Cyclonic vorticity growth was predominately located at 600 hPa for the majority of the period prior to TCG, which is consistent with vorticity development in a baroclinically and barotropically unstable AEW (Hopsch et al. 2010). After 12/0000, the vorticity difference between 925 and 600 hPa changes sign, signifying the initiation of low-level cyclonic vorticity growth associated with the onset of TCG (Fig. 2.5b). Meanwhile, the AEW under study encountered sufficiently warm SSTs for tropical development, being at or above 27°C.

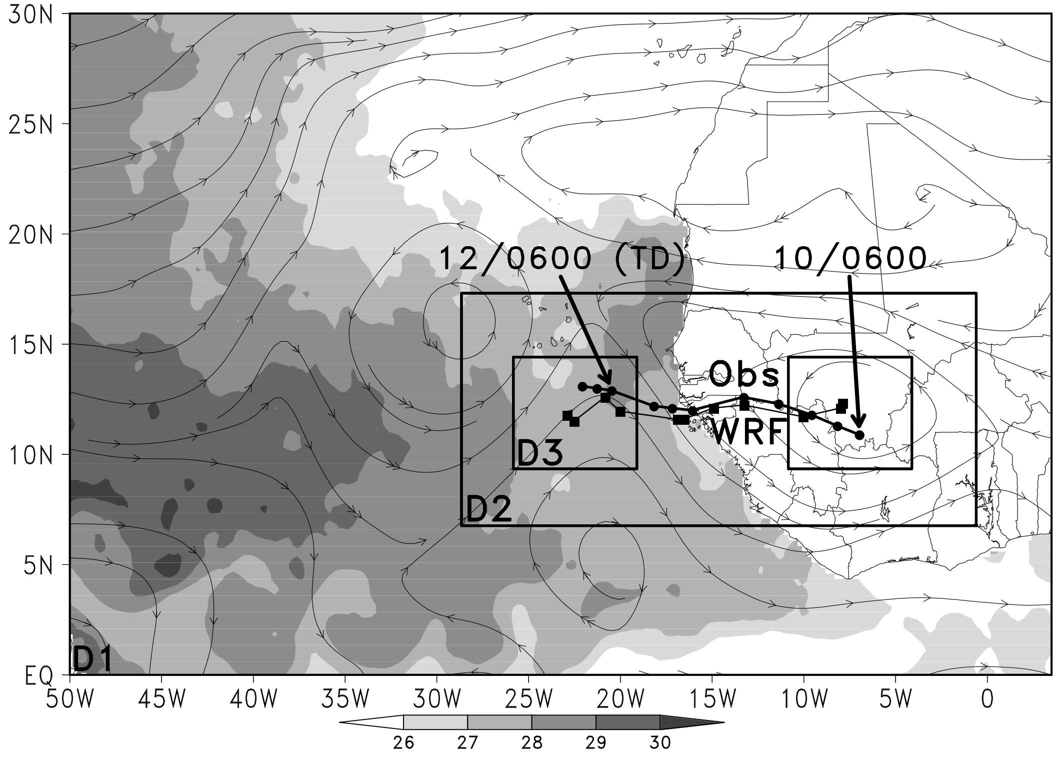

Figure 2.3: The WRF model domain configurations: boxes D1, D2 and D3 show the domain with the horizontal resolution of 9, 3 and 1 km, respectively, with the initial and final position of the moving domain D3 also given. The WRF-simulated track (square marks) versus the best fixes track (circle marks) from 0600 UTC 10 (10/0600) to 1800 UTC 12 Sep are overlaid. The NOAA OI SSTs (°C, shaded) and ERA-Interim 600-hPa co-moving streamlines at 0000 UTC 10 September are also overlaid.

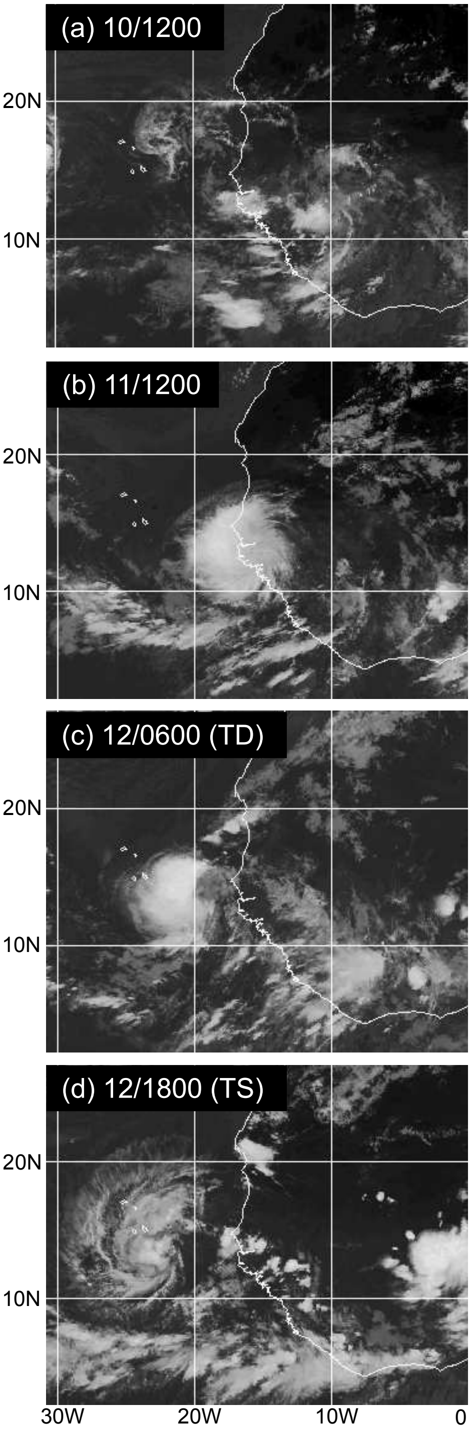

Figure 2.4: METEOSAT-9 IR imagery for four stages of Hurricane Julia: (a) sporadic convection within the AEW at 1200 UTC 10 Sep, (b) well-defined MCS within the AEW at 1200 UTC 11 Sep, (c) tropical depression (TD) at 0600 UTC 12 Sep and (d) tropical storm (TS) at 1800 UTC 12 Sep 2010.

2.2 Control model description

To investigate the mesoscale processes associated with TCG, a control simulation is conducted using Version 3.2.1 of the fully compressible, nonhydrostatic mesoscale WRF model with Advanced Research (ARW) core (Skamarock et al. 2005). Three nests with horizontal resolutions 9, 3, and 1 km, as depicted by the boxes given in Fig. 2.3 (D1, D2, and D3, respectively) are utilized. These nests have 36 vertical levels and a model top set of 50 hPa with enhanced resolutions in the lower and upper troposphere to gain greater resolution where the confluent and diffluent motions are most present during TCG. The WRF 66-h simulation is initialized at 10/0000, i.e., 54 h prior to the named TD of Julia, and ends 12/1800, when the storm became a TS. Such an initialization time 54 h prior to TCG enables the control to capture the evolution of atmospheric flow from being mainly mid-tropospheric (i.e., the AEW) to lower-tropospheric (i.e., the developing MSLP disturbance) with minimal likelihood of inaccurately capturing the TCG event. The lateral boundary and initial conditions are supplied by the European Centre for Medium-Range Weather Forecasts Re-Analysis (ERA-Interim) reanalysis except for SSTs that are initialized by the National Oceanic and Atmospheric Administration (NOAA) Optimal Interpolation high-resolution SST data set (Reynolds et al. 2007)[1]. It should be noted that the simulation includes the NOAA OI SST data in order to gain higher spatial resolution information associated with the passage of Hurricane Igor as Julia

---

[1] NOAA OI SSTs remain fixed for the integration as the SSTs remain nearly constant over the 66 h period.

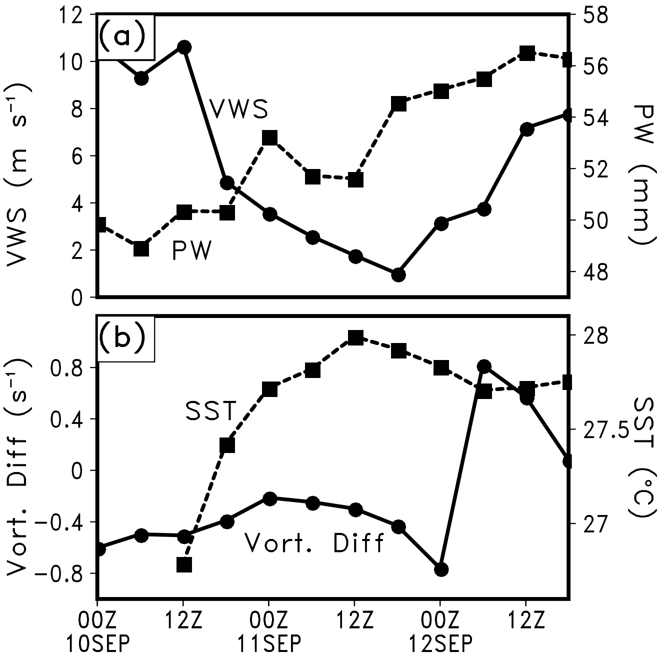

Figure 2.5: Time series of (a) deep-layer vertical wind shear (VWS) between 200 and 850 hPa and precipitable water (PW) and (b) 925-600 hPa relative vorticity difference ($\zeta_{925} - \zeta_{600}$) and SST during the 66-h period from 0000 UTC 10 Sep to 1800 UTC 12 Sep. Each variable is calculated by averaging its field within a 500 km × 500 km area from the storm center using ERA-Interim data.

passed over water previously traversed by Igor. Without using high-resolution SST data, the simulated Julia is too strong post-TCG given the coarser-resolution SST data not being able to resolve the cooler SSTs to the south-southeast of the Cape Verde Islands associated with Igor's passage. This indicates the importance of air-sea interactions (e.g., strengthening by WISHE) for Julia when it intensifies into a TS by the end of the simulation. Obviously, the air-sea interactions prior to and at the time of TCG are limited given the weakness of the low-level winds.

The 9- and 3-km resolution domains incorporate simultaneously the Kain-

Fritsch convection parameterization scheme (Kain 2004; Kain and Fritsch 1990) and a cloud micro-physics scheme, while the former is bypassed in the 1-km resolution domain. Upon initial experimentation, we came to the conclusion that there were very little differences between two simulations with the 3-km domain having respective convection parametrized and explicitly represented. The simulation utilizes the Thompson graupel 2-moment micro-physics scheme (Thompson et al. 2008, 2004), the Rapid Radiative Transfer Model (RRTM) longwave radiation scheme (Mlawer et al. 1997), the Dudhia (1989) shortwave radiation scheme, and the Yonsei University (YSU) planetary boundary layer (PBL) scheme (Noh et al. 2003).

The 1-km is a moving domain with 570 preset moves starting 9 h after the initialization time. Easterly moves are conducted every 6 minutes to follow the AEW and involves no movement of the domain latitudinally. Preset moves are used since the vortex-following tool associated with the WRF has trouble following the AEW with tracking levels at 600 hPa even given the relatively strong AEW.

2.3 Model validation

Overall, the WRF control simulation reproduces reasonably well the observed track over the 66-h integration (Fig. 2.3). On average, the simulated track error is 173 km, but its operational 36-h forecast did significantly better than the NHC official (OFCL) forecast track error for the same time (Beven and Landsea 2010), with a track error of 94 km compared to the OFCL forecast error of 133 km. The intensification of pre-TD Julia was unremarkable, reaching a P_{MIN} of 1007 hPa at

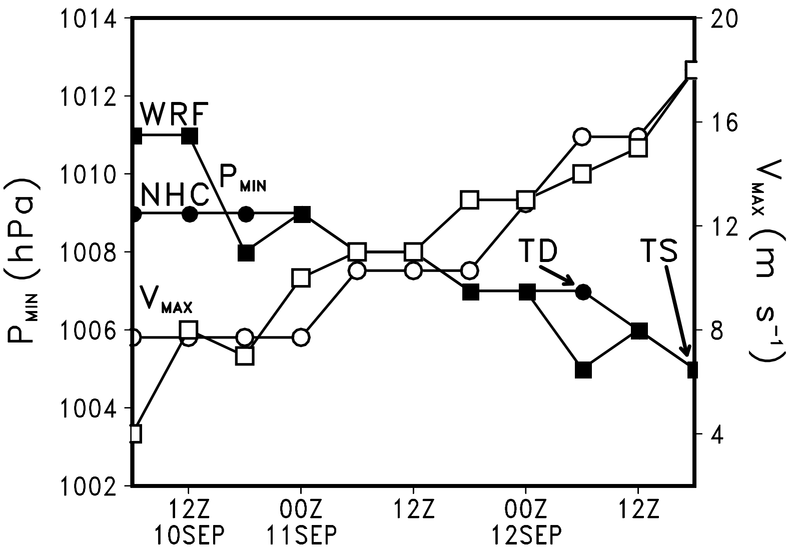

Figure 2.6: Time series of the WRF-simulated storm intensity (square marks) and the NHC best estimates (circle marks) for the minimum MSLP (P_{MIN}, closed marks) and z = 10-m maximum wind speed (V_{MAX}, open marks) from 0600 UTC 10 to 1800 UTC 12 Sep.

the TCG time as seen in observed P_{MIN} estimates (Fig. 2.6). The simulated P_{MIN} and maximum wind speed at z = 10 m (V_{MAX}) both agree well with the observed, although they are not without discrepancies. One difference is that the simulated surface vortex is 2 hPa weaker than the observed during the first 12 h of integration and is 2 hPa stronger at TCG.

Two development stages can be identified from the P_{MIN} changes: (i) TCG; and (ii) significant intensification (SI) prior to and after 12/0600, respectively. Specifically, the P_{MIN} of the disturbance during TCG barely changes, with an average deepening rate of 1 hPa day^{-1}. In contrast, the SI phase begins with the deepening rate increasing to 4 hPa day^{-1} until the storm becomes a TS, similar to the results of Nolan (2007). The simulated MSLP prematurely enters SI at 12/0000, with a deepening of 2 hPa for the 6 h prior to the storm becoming a named TD. Later in the SI stage, the simulated P_{MIN} shows brief weakening before restrengthening at 12/1800. This reprieve is supported by the decrease in SSTs and increase in VWS shown in Fig. 2.5, which inhibit further intensification. While these developmental stages are evident in P_{MIN}, they cannot be seen from the 10-m maximum wind speed as both the observations and simulation show a nearly consistent increase during the 66-h integration.

Fig. 2.7 shows the simulated cloud patterns of the AEW (and Julia) that should be compared to the observed *METEOSAT-9* Infrared (IR) imagery given in Fig. 2.4. The simulated brightness temperatures are calculated using the Unified Post Processor (UPP), which invokes the Community Radiative Transfer Model (CRTM) to produce brightness temperatures at the top of the atmosphere. After 12 h into the integration, the model reproduces the locations of deep convection along the coastline, indicating reasonable forcing within the AEW. However, the simulated cloud field associated with the AEW appears to be weaker and more fragmented than the observed (cf. Figs. 2.4a and 2.7a), due partly to the lack of precipitation spin-up and partly to the simulated upper-level cloud ice content that may be much less than that in nature. The differences between the simulated and observed cloud patterns decrease afterward. By 11/1200 (cf. Figs. 2.4b and 2.7b), the simulated brightness temperatures show well the convective development along the coastline, although it does not look like the round-shaped MCS as seen in *METEOSAT-9* IR imagery. The WRF nearly reproduces the observed brightness temperatures of TD Julia at 12/0600. Even with the slow convective development during the early stages, the WRF simulates a TS-like cloud pattern at 12/1800 that compares favorably with the observed (Fig. 2.7d).

Since we are concerned with mesoscale development in addition to the AEW, Fig. 2.8 compares the simulated hourly precipitation rates (mm h^{-1}) to the Tropical Rainfall Measuring Mission (TRMM) data during two times during TCG. The TRMM data consists of precipitation rate estimates generated every 3 h on a $0.25° \times 0.25°$ grid between 50°S and 50°N. The overall spatial characteristics of the TRMM-estimated precipitation rates compare favorably with the simulated, although some minor discrepancies on the location of heavy precipitation rates are evident.

At 12/0300, the TRMM estimate depicts a more coherent, MCS-like structure while the simulated shows two distinct precipitation areas with little convective development in between (Fig. 2.8a). Even with this disagreement, the intensity of the simulated rates fares well with the TRMM, highlighting small regions of intense precipitation in excess of 30 mm h^{-1}. By 12/0600, the simulated rates reproduce the MCS-like structure shown in TRMM estimates with little spatial disagreement. However, the simulation seems to be overestimating the precipitation rates on the southern end of the feature with a broad swath of 30 mm h^{-1} or greater rates (Fig. 2.8b). This discrepancy is contrasted by a reasonable estimate of the heavy precipitation rates on the northern portion of the feature shown in TRMM estimates. Overall, the characteristics of the TRMM precipitation rates are reasonably reproduced by the simulation for the 3-h period between when discounting minor spatial displacements and the differences in resolution between the two data sets.

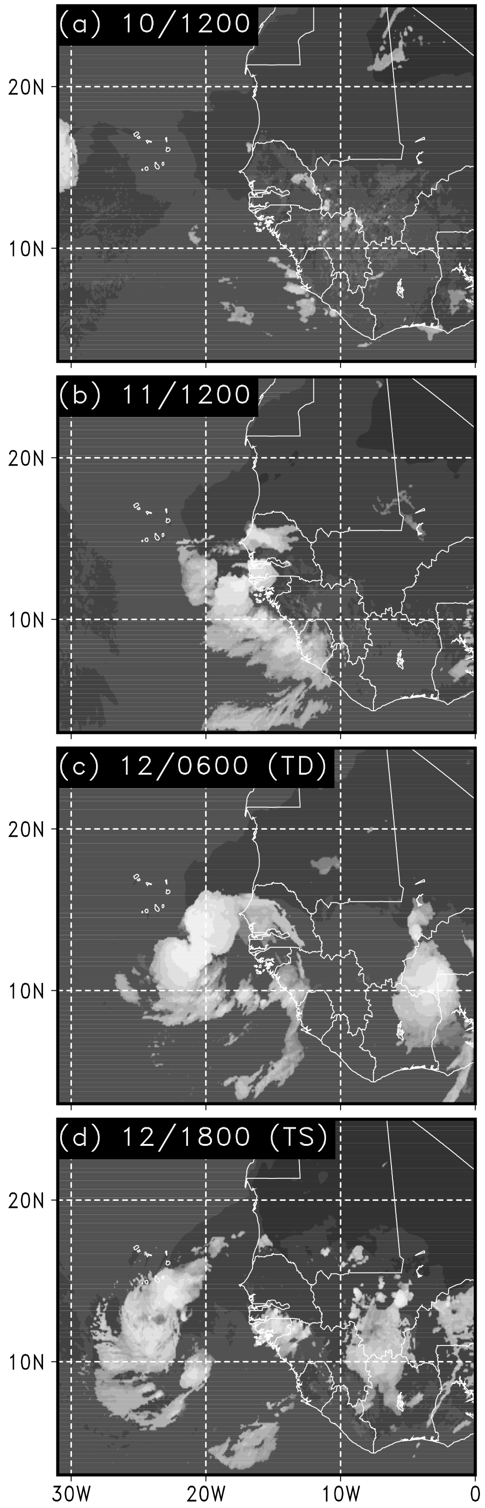

Figure 2.7: As in Fig. 2.4, except for the WRF-simulated brightness temperature (K).

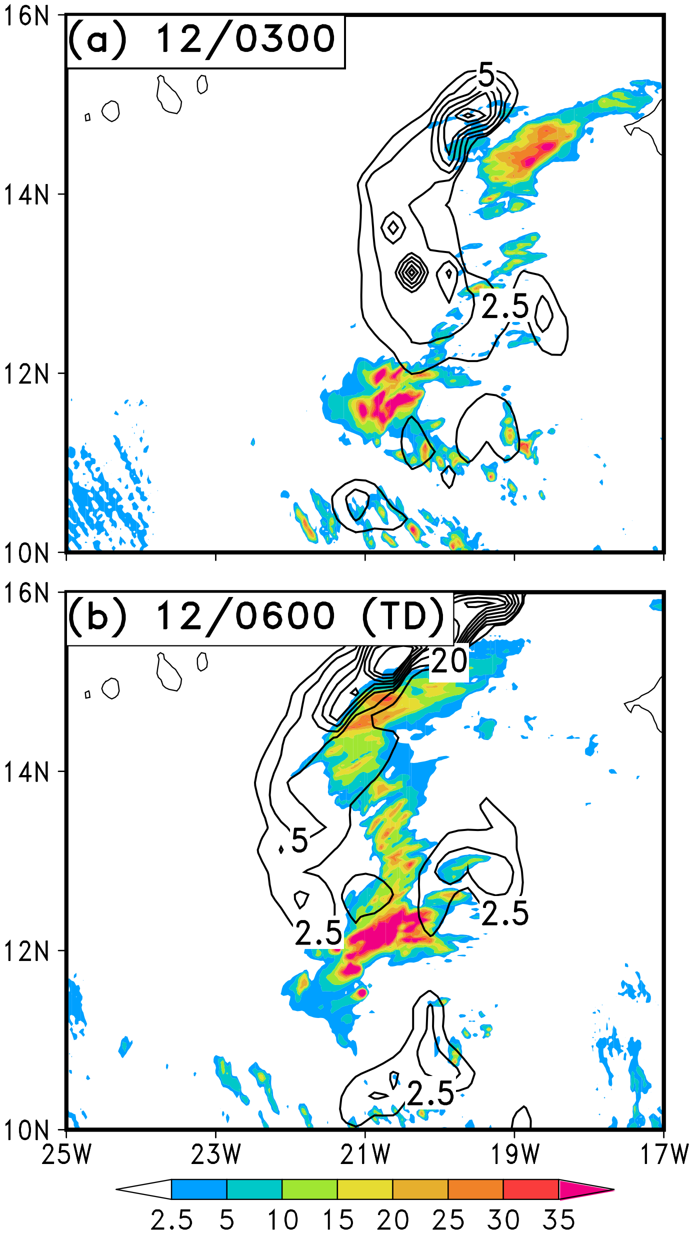

Figure 2.8: Comparison of the WRF-simulated hourly precipitation rate (shaded, mm h^{-1}) and TRMM-adjusted merged-infrared precipitation rate (contoured at intervals of 2.5, 5, 10, 15, 20, 25, 30 and 35 mm h^{-1}) for (a) 0300; and (b) 0600 UTC 12 Sep. The 3-km horizontal resolution WRF data is used while the TRMM data has a horizontal resolution of 0.25 degrees × 0.25 degrees.

2.4 Low-level development and upper-level processes

After verifying the simulated storm against the observed, we can use the high-resolution simulation data to examine the development of some non-observable features, especially the meso-β-scale LLV that becomes TD Julia. In this section, we show that the LLV develops within the parent AEW, but they are not directly collocated until into the simulated storm's SI stage. In particular, we show that the LLV formation results from persistent deep convection and its generated vortices, upper-tropospheric warming and vorticity growth in the lower troposphere. The AEW serves as the parent in a deep layer, which is similar to that described by the marsupial pouch paradigm (Dunkerton et al. 2009; Montgomery et al. 2010; Wang et al. 2010a), protecting the upper-level warming and the LLV from adverse environmental conditions while providing a preferred location for mesoscale development.

2.4.1 Connecting the AEW to MSLP falls, upper-level warming and the LLV

Fig. 2.9 presents the evolution of meso-α-scale MSLP falls, a meso-β surface low (marked by "L"), the LLV, and AEW. A closed MSLP isobar ("L") first appears within the AEW at 12/0000 (Fig. 2.9a). This closed isobar, however, is considered to be a meso-β low rather than TD Julia, since its size is comparable to other meso-β features. Even though the simulated storm is not a TD-scale disturbance until 12/0600 (Fig. 2.9c), the remainder of our discussion will refer to the simulated

SI starting at 12/0000 since an intensifying surface low is identifiable. Initially, the mesolow and the AEW center (marked by "X") are separated by a distance of approximately 150 km (Fig. 2.9a), remaining at this distance until 12/0600 as the surface low deepens. After 12/0600, the distance between the two centers shrinks to roughly 100 km (Fig. 2.9c) with the features becoming completely collocated at 12/0900 (Fig. 2.9d).

The change in distance between the disturbances over the 9-h period can be more clearly seen from the vertical vorticity structures depicted by Figs. 2.9e-h. Initially, the dominant vorticity feature is that of the AEW (its peak denoted by "A"), maximizing in strength between 700 and 400 hPa at 12/0000 (Fig. 2.9e). At 12/0300, a deep upright column of cyclonic vorticity associated with the meso-β surface low emerges at the edge of the tilted vorticity column associated with the AEW with a peak magnitude quickly dwarfing that of the AEW (Fig. 2.9f). Given the magnitude of the cyclonic vorticity associated with the mesolow, it is evident that the vorticity structure can be considered an LLV. In contrast, the AEW's vorticity exhibits little change during the hours prior to TCG, let alone the past 54 h (cf. Figs. 2.2b and 2.9e-h). While the LLV is intensifying with time, it begins to merge with the vertically tilted AEW vortex, beginning in the mid-to-upper troposphere. Although the mesolow signifies the beginning of the SI stage at 12/0000 (Fig. 2.6), the LLV completely merges into the AEW vortex center by 12/0900 (Figs. 2.9d and 2.9h).

Even with the near constant intensity of the AEW over the 54-h period, its MSLP field and intensity show significant changes due to the development of deep

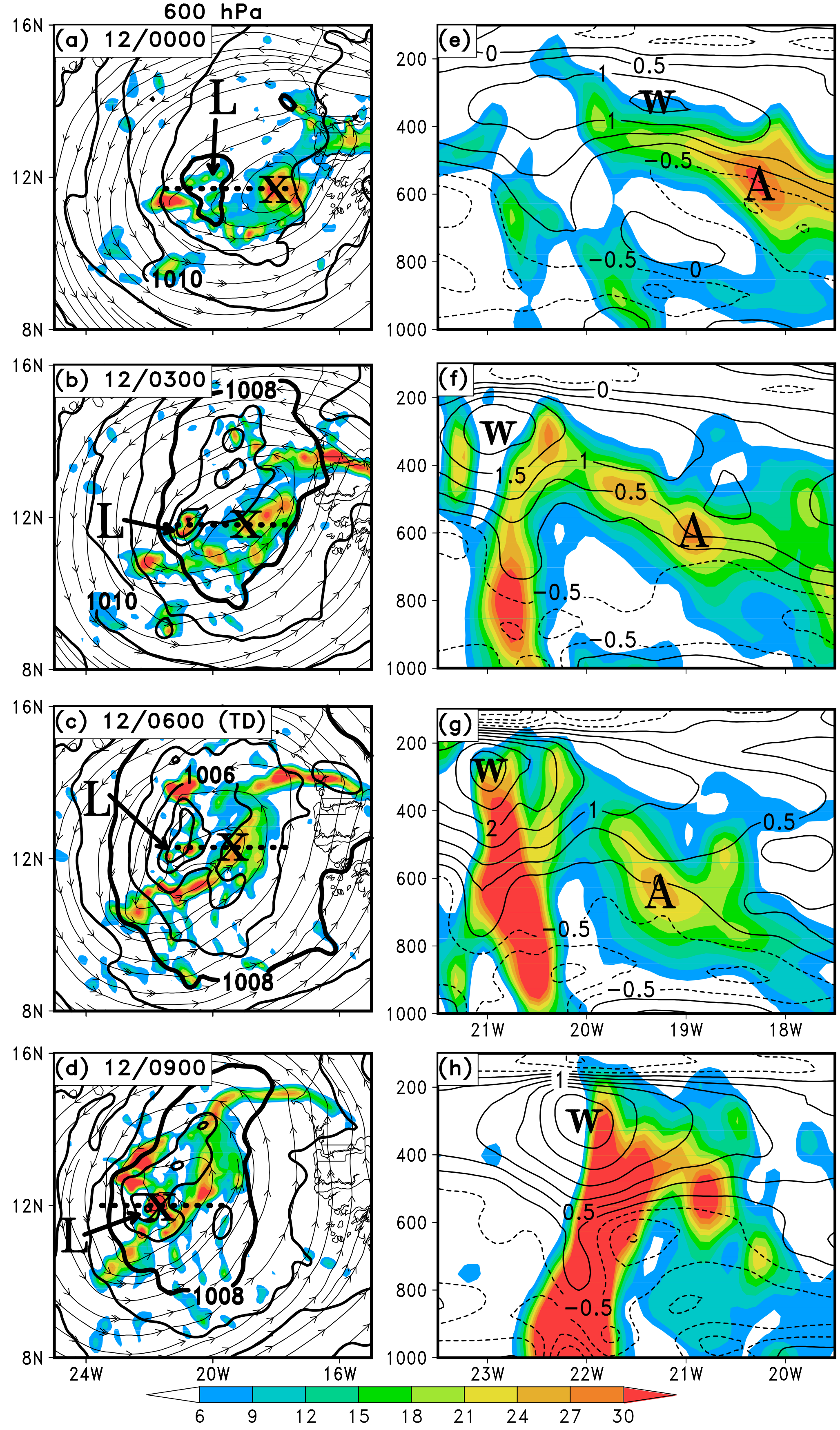
600 hPa
(a) 12/0000
(b) 12/0300
(c) 12/0600 (TD)
(d) 12/0900
(e)
(f)
(g)
(h)
L
X
W
A
1010
1008
1006
16N
12N
8N
24W
20W
16W
200
400
600
800
1000
23W
22W
21W
20W
19W
18W
0
0.5
1
1.5
2
-0.5
6
9
12
15
18
21
24
27
30

Figure 2.9: (a)-(d) The simulated 600-hPa cyclonic relative vorticity (shaded, $\times 10^{-5}$ s^{-1}), co-moving streamlines and MSLP (contoured at intervals of 1 hPa). "L" represents the center of a developing mesolow while the intersection of the 600-hPa trough axis and critical latitude is marked with the "X". The dotted line designates the west-east cross sections shown in (e) through (h). (a)-(d) span the same longitudes listed below (d). (e)-(h) Longitude-height cross sections of cyclonic relative vorticity (shaded, $\times 10^{-5}$ s^{-1}), and temperature deviations (contoured at intervals of 0.5°C) that are calculated by subtracting the mean temperature at each level of the cross-section. "A" represents the location of the peak cyclonic vorticity associated with the AEW while "W" marks the location of the upper-level warming. The cross section length in (e) through (h) is approximately 400 km starting at 21.5°W and ending at 17.5°W, with the exception of (h), which extends from 23.5°W to 19.5°W. The cross sections are created using a 3-slice average. Data from the WRF 9-km resolution domain is used to create (a) through (h).

convection (to be shown later), with the majority of changes taking place between 12/0000 and 12/0900. In addition to the local MSLP falls associated with the meso-β surface low ("L"), one can see spatial expansion of the MSLP falls with time from the meso-β to meso-α scale. This is easily exemplified by the 1008-hPa isobar in Figs. 2.9a-d, which continually expands until 12/0600 before contracting slightly at 12/0900.

Further, Figs. 2.9e-h show that the intensification of the meso-β surface low and meso-α MSLP falls are accompanied by thermodynamic changes in the upper troposphere. Initially, the only evident thermodynamic profile is that of the AEW, with a tilted warm layer above the mid-level vortex marked by "W" in Fig. 2.9e. This tilted profile quickly diminishes as warmth in excess of 2°C takes place directly above the developing LLV ("W", Fig. 2.9f), connecting with the warm layer above the mid-level vortex associated with the AEW. As the warming intensifies at 12/0900, it continues to merge with the thermodynamic profile associated with the AEW until the AEW profile is no longer identifiable and the upper tropospheric warmth exceeds 2.5°C (Fig. 2.9h).

2.4.2 Meso-α and meso-β MSLP falls and their relationship to upper-level warming and deep convection

While the preceding subsection demonstrates some relationship between the AEW, the meso-β surface low, LLV, and upper-tropospheric warming, an obvious question to ask is: how do these features interact? The following will answer this question in addition to determining what role, if any, the warming seen in Figs. 2.9e-h has on meso-α and meso-β MSLP falls. In this regard, we note the observational study of Hoxit et al. (1976) showing that upper-level warming (in the 100- to 500-hPa layer) associated with deep convection in mid-latitude MCSs could produce surface pressure falls of 2 to 4 hPa h^{-1}. They attributed meso-β-scale surface lows to the hydrostatic warming aloft. Similarly, Zhang and Zhu (2012) have shown the importance of the upper-tropospheric warming in TCG, demonstrating that the warming prior to TCG accounts for the majority of the MSLP falls. They hypothesize that the upper-tropospheric warming is produced by widespread deep convection which detrains just below the tropopause and then by outward advection through divergent flows. The following will only focus on the 3 h between 12/0300 and 12/0600, when the MSLP falls are the greatest at approximately 0.67 hPa h^{-1} (Figs. 2.9a-d) and the development of the LLV occurs.

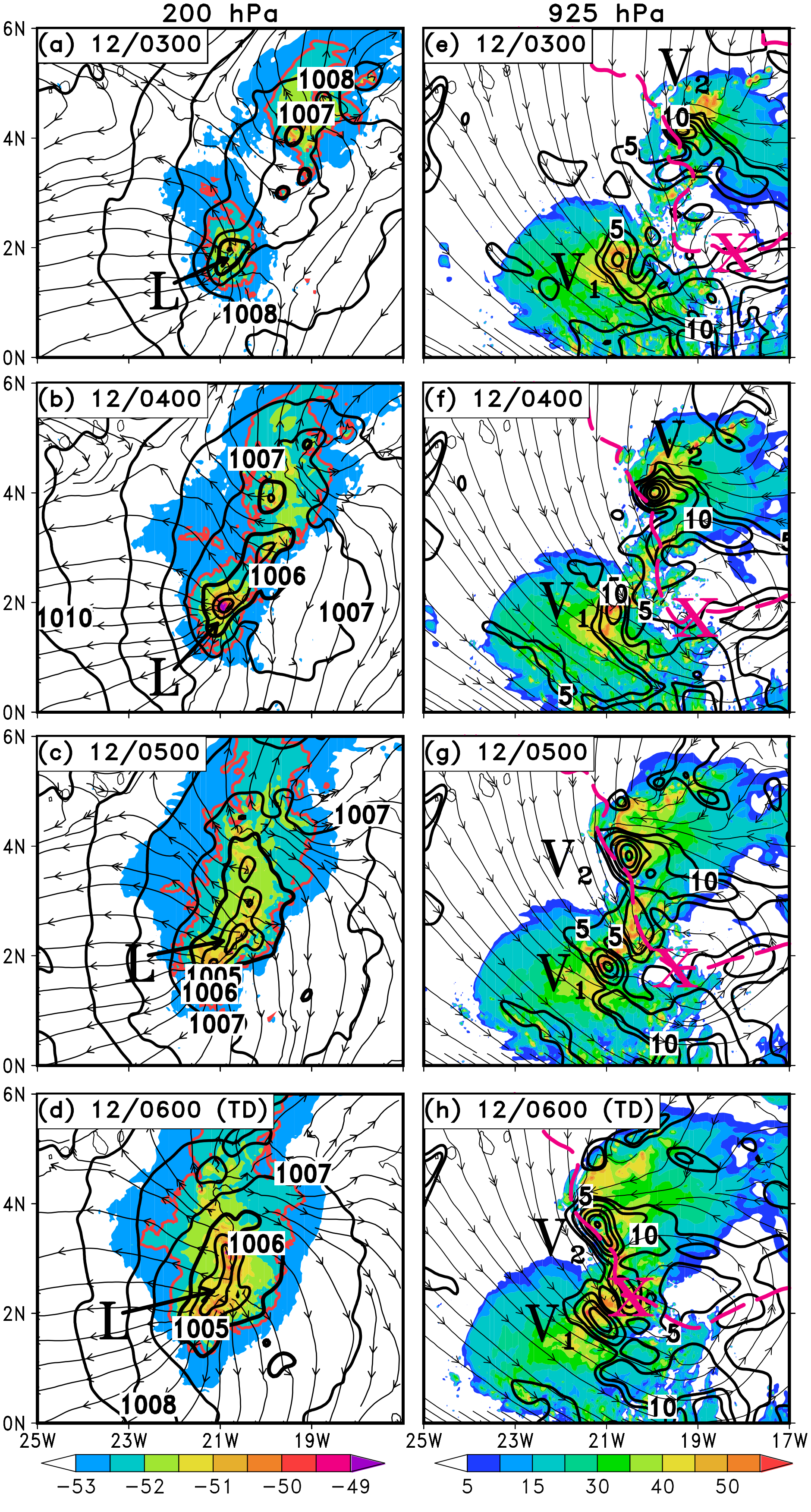

200 hPa
925 hPa
(a) 12/0300
(b) 12/0400
(c) 12/0500
(d) 12/0600 (TD)
(e) 12/0300
(f) 12/0400
(g) 12/0500
(h) 12/0600 (TD)
1008
1007
1006
1005
1010
L
V_1
V_2
X
5
10
16N
14N
12N
10N
25W
23W
21W
19W
17W
−53
−52
−51
−50
−49
15
30
40
50

Figure 2.10: (a)-(d): The simulated 200-hPa temperature (shaded, °C), co-moving streamlines and MSLP (contoured at intervals of 1 hPa) from the 51-54 h integrations, valid at 0300, 0400, 0500 and 0600 UTC 12 Sep, respectively. The -52.5°C isotherm is outlined in bold red to show the expansion of the warmth while the 1006-hPa isobar is thickened to demonstrate the expansion of the mesolow. "L" represents the center of a developing meso-β surface low. (e)-(h): The simulated composite radar reflectivity (shaded, dBz), 925-hPa cyclonic relative vorticity (contoured at intervals of 5×10^{-5} s^{-1}), co-moving streamlines, and AEW critical latitude (magenta dashed line) for the same times as (a) through (d). V_1 and V_2 represent the two main meso-β-scale vortices that become the LLV. The intersection of the 925-hPa AEW trough axis with its respective critical latitude is marked with the magenta "X". Data from the WRF 3-km resolution domain is used to create (a) through (h).

Figs. 2.10a-h show that the MSLP falls are consistently collocated with the warmer air at 200 hPa that also resides along the AEW's critical latitude at 925 hPa for the 3-h period. Further, these features are collocated with a region of active convection shown in Fig. 2.8. We use the 1006-hPa isobar and the -52.5°C isotherm to help elucidate the relationship between changes in surface pressure and upper-tropospheric warming. As the -52.5°C isotherm expands outward over the period into a meso-α-scale feature, so does the 1006-hPa isobar which nearly takes the same shape and size as the warmer temperatures at 200 hPa. Within the meso-α-scale MSLP falls, smaller meso-β and meso-γ P_{MIN} centers reside beneath the warmest temperatures at 200 hPa, with examples marked by "L" in Figs. 2.10a-d. An exceptional occurrence of such a feature occurs at 12/0400 when a 1004-hPa MSLP closed contour develops directly beneath 200-hPa temperatures in excess of -49°C (Fig. 2.10b). The concurrent development of the 200-hPa warming and the meso-α MSLP falls supports the notion that the warming may be hydrostatically responsible for the intensity and size of the MSLP disturbance. These features can be linked to the development, intensification and aggregation of convection along the AEW low-level critical latitude, as is explained next via Figs. 2.10e-h.

It is seen in the composite radar reflectivity that the development of deep convection occurs in the same regions as the warming at 200 hPa as well as along the AEW's low-level critical latitude (Figs. 2.10e-h). Since deep convection (either as individual convective cells or an MCS) tends to move with the AEW when it resides on the AEW low-level critical latitude (Dunkerton et al. 2009), it is able to persistently detrain in the upper troposphere allowing for the warming to intensify and advect radially outward as a storm-scale outflow develops. The streamline analyses in Figs. 2.10a-d support the outward expansion of the warming in time, with a storm-scale outflow developing by 12/0600. Initially, this outflow is less coherent (e.g., at 12/0300) resulting in similar patterns of upper-level warming and surface pressure falls. Once deep convection becomes organized along the AEW low-level critical latitude, a storm-scale outflow develops, expanding the upper-tropospheric warming and allowing for MSLP falls on the meso-α scale.

Figs. 2.10e-h show the relationship between the meso-β-scale surface pressure falls and the development of low-level cyclonic vorticity. Initially, two noticeable mesovortices ("V_1" and "V_2", respectively) reside within meso-β-scale MSLP lows and consequently, in regions where the PBL convergence is enhanced as evidenced by the co-moving streamline analysis (Fig. 2.10e). The mesovortices intensify via vortex stretching, noted by the presence of convection and related upward motions (Figs. 2.10e-h). A notable characteristic of V_2 is its radial movement along the low-level critical latitude (Figs. 2.10e-h). This vortex starts off nearly 200 km from the AEW center at 12/0300, but cascades towards the AEW center along the critical latitude as it begins to merge with V_1 at 12/0600. The interaction of these two vortices at 12/0600 represents the conglomeration and homogenization of the 925-hPa cyclonic vorticity field resulting in the creation of the meso-β-scale LLV. Additionally, the enhancement of the vortices is consistently along the critical latitude of the 925-hPa AEW circulation near the pouch center (Figs. 2.10e-h), validating the connection between the meso- and larger-scale circulations postulated by Dunkerton et al. (2009). Further, the LLV at 12/0600 also starts to take the shape of the meso-β-scale surface low encompassed by the 1006-hPa isobar (Fig. 2.10h), hinting that its amplification is partly explained by the surface pressure falls induced by the warming aloft.

To further analyze the evolution of the upper-tropospheric warming, Fig. 2.11a presents a 100 km × 100 km area-averaged time series following the storm center of cyclonic vorticity and relative warming with respect to the vertical temperature profile at 11/0600[2]. Two distinct warming periods are evident in Fig. 2.11a: (i) a shallow intense warming event in the layer above 250 hPa during the first 18 h with a peak intensity near 1.25°C at 11/1500; and (ii) a deep layer warming event in association with the onset of SI after 12/0000. The first warming period is in good agreement with the early sporadic convection within the AEW when the latter moves across the coastline (Figs. 2.7a,b) and the system is dominated by

---

[2] A 100 km × 100 km average is used to accurately capture the critical information related to TCG as noted by Wang (2012).

the mid-level cyclonic vortex ("AEW" in Fig. 2.11a). The localized nature of the deep convection is relatively less efficient at generating larger-scale warming in the upper-troposphere since a coherent storm-scale outflow is not present. Clearly, the period of second warming period occurs with the onset of SI. This period is denoted by steady warming in the 375- to 150-hPa layer (Fig. 2.11a), in agreement with the warming shown above the developing meso-β surface low and LLV in Figs. 2.10e-h and 2.9a-d. The magnitude and depth of the upper-tropospheric warming continues to increase with an amplitude exceeding 1.5°C at and after 12/0600. The evolution of the upper troposphere is complemented by concurrent development of the LLV as evidenced by the cyclonic vorticity development between 950 and 700 hPa at and after 12/0300.

Quantifying the importance of the upper-level warming for surface pressure falls, Fig. 2.11b is plotted following the procedures similar to those described in Chen and Zhang (2013), in which (a) the MSLP is obtained by calculating the hydrostatic equation from the tropopause downward using the total temperature (i.e., the sum of the temperature profile at 11/0600 and the warming, curve WUW); and (b) repeating (a) but excluding the upper-level warming enclosed by the dashed lines, curve NUW. The control-simulated time series of MSLP (curve CTL) is also given to facilitate the comparison between the two different calculations. Obviously, the NUW time series struggles to reproduce the MSLP of the control simulation and diverges from the other solutions after 11/0900. The differences between NUW and CTL maximize after 12/0000 when the convective activity becomes more coherent and the resulting warming begins to hydrostatically induce more pronounced MSLP

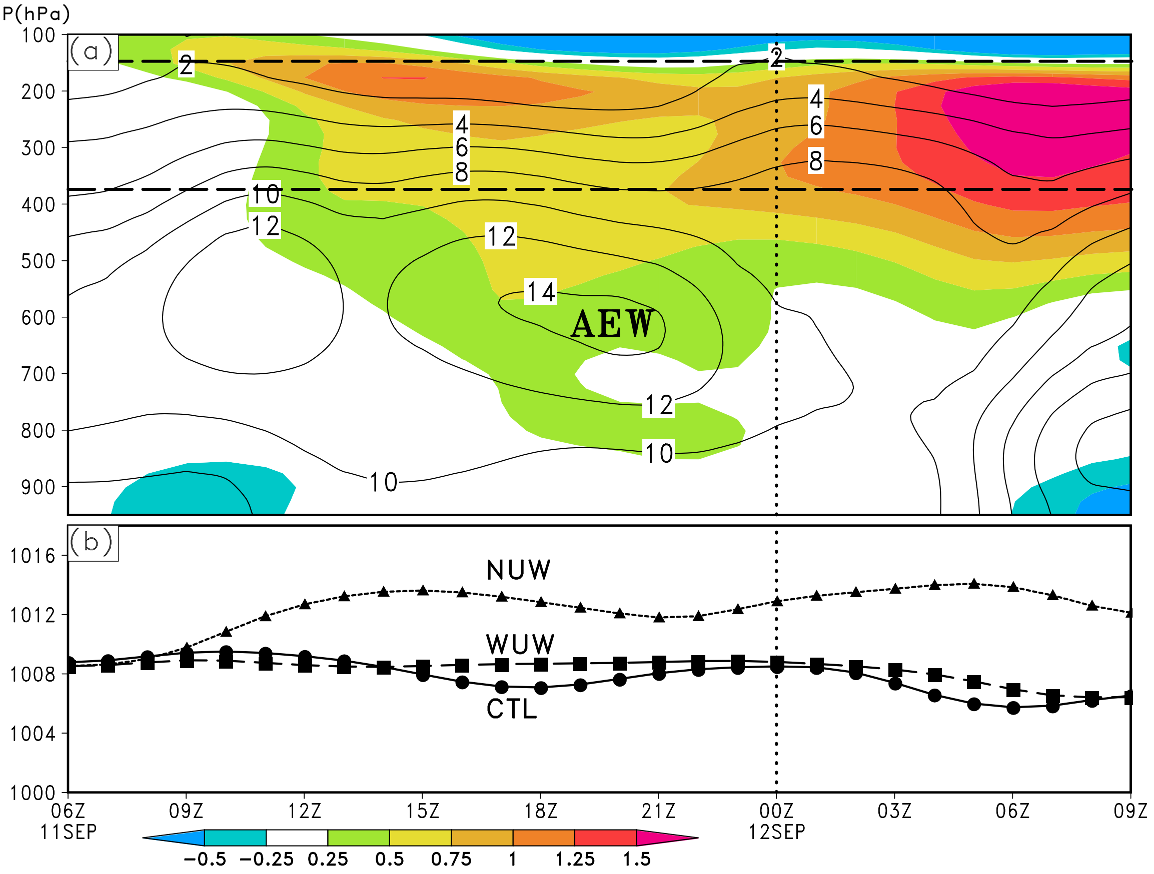

Figure 2.11: (a) Time-height cross section of the simulated temperature difference from the 30-h simulated (valid at 0600 UTC 11 Sep, shaded, °C) and cyclonic relative vorticity (contoured at intervals of 2×10^{-5} s^{-1}) that are obtained using a 100 km × 100 km average surrounding the storm center. Dashed lines represent the core of the upper-level warming and "AEW" marks the peak cyclonic vorticity associated with the AEW. (b) Time series of the 100 km × 100 km area-averaged MSLP (hPa) from the WRF simulation (CTL) and two hydrostatic calculations (NUW and WUW). The NUW hydrostatic calculation uses the vertical temperature profile from 0600 UTC 11 Sep between the dashed lines in (a) while WUW utilizes the 0600 UTC 11 Sep profile plus the temperature perturbations between the dashed lines seen in (a). The dotted line in both (a) and (b) represent the time SI begins for the simulated storm, 0000 UTC 12 Sep. Data from the WRF 1-km resolution domain is used to create both (a) and (b).

falls. The difference between the two reaches a peak of nearly 10 hPa as the NUW time series never develops a TD. Contrasting its counterpart, the WUW hydrostatic calculation is nearly able to fully reproduce the CTL time series. The difference between the CTL and WUW is never greater than 2.5 hPa, implying the importance of the upper-tropospheric warming for MSLP falls and the intensification of the meso-β surface low.

2.4.3 Development of the upper-level warming

After seeing a connection between upper-level warming, the meso-α-scale MSLP falls, the meso-β-scale surface low and the LLV in the preceding subsections, we show below how the upper-level warming forms. Chen and Zhang (2013) showed that adiabatic subsidence resulted in the development of an upper-level warm core during the rapid intensification stage of Hurricane Wilma. While large-scale adiabatic subsidence warming might be true for a mature TC, it remains unanswered how the upper-tropospheric warming during TCG forms. Of particular interest herein are the meso-γ-scale features, namely, convective bursts (CBs) and their influence on the upper-level warming. Traditionally, CBs are defined as intense meso-γ convective cells with updrafts maximized in the upper troposphere. The method by which a CB is defined is rather arbitrary, with the updraft velocity threshold being anywhere from 8 to 15 m s^{-1}, as used in Chen and Zhang (2013). For our investigation, we will designate a convective cell a CB when it is characterized by an updraft in excess of 8 m s^{-1} at or above the freezing level (approximately 600 hPa).

Focusing on 12/0000 (onset of SI, Figs. 2.12a,b), the meso-β-scale surface low is characterized by embedded meso-γ-scale structures beneath upward motions aloft (red shadings). An example of such a meso-γ-low and its associated upward vertical motion is marked by "U_1". Applying our definition of CBs, it is clear that many of the meso-γ structures are CBs, with some cells characterized by upward velocities in excess of 10 m s^{-1} in the 275-175 hPa layer. Surrounding these CBs, compensating subsidence (blue shadings) occurs in nearly indistinguishable storm-scale outflow. Directly collocated with the CBs are large cloud ice mixing ratios and warm temperatures within the 275-175 hPa layer (Fig. 2.12b). This collocation suggests that these warm temperatures are associated with the latent heat of freezing and deposition as cloud water freezes after being transported upward across the 0°C level and more water vapor is deposited on cloud ice particles aloft[3]. However, these heating elements are localized to the outflow generated by individual CBs, which are sporadically located within the meso-β surface low.

Vertical cross sections through the surface mesolow show that CBs transport cloud water above the freezing level with heating in their cores (Figs. 2.13a,b). At the intersection of the two cross sections ("I_1"), a CB extending from the 0°C level (thick black line) to 100 hPa with upward velocities in excess of 10 m s^{-1} is transporting large ice content to the upper troposphere. This characteristic is also found in the core region of CB U_1, but with cloud ice mixing ratios much larger

---

[3] Note that herein we distinguish that diabatic heating, which tends to accelerate updrafts, from the warming caused by compensating subsidence since the former is often more transient than the latter.

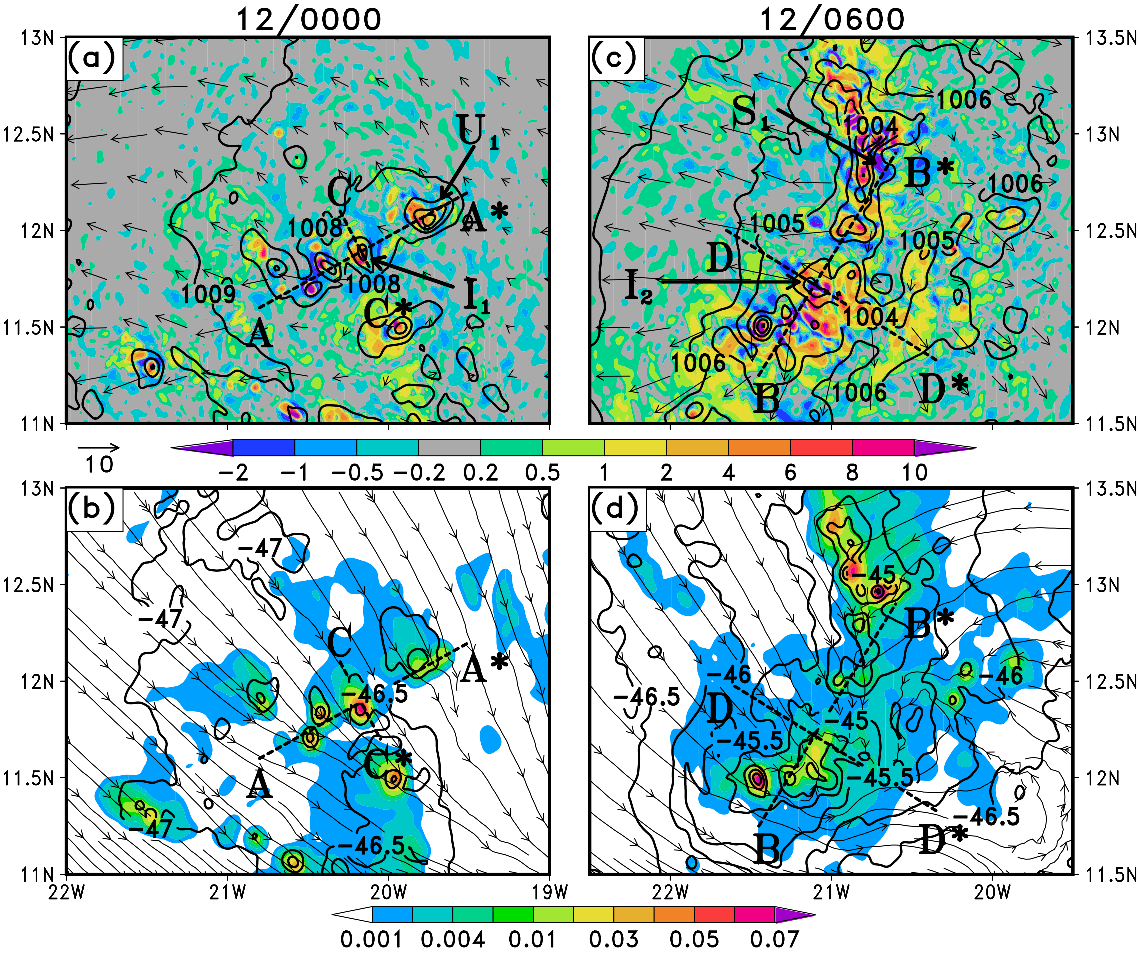

Figure 2.12: (a) and (c): Simulated 275-175 hPa layer-averaged vertical velocity (shaded, m s^{-1}) and co-moving wind vectors (m s^{-1}) with MSLP (contoured at intervals of 1 hPa) overlaid for 0000 and 0600 UTC 12 Sep, respectively. (b) and (d): Simulated 275-175 hPa layer-averaged cloud ice mixing ratio (shaded, g kg^{-1}) and temperature (contoured at intervals of 0.5°C) with 925 hPa co-moving streamlines overlaid for the same times as in (a) and (c), respectively. Dashed lines labeled A-A*, B-B*, C-C* and D-D* represent the locations of vertical cross sections shown in Fig. 2.13. Cross sections A-A* and B-B* are created along the main axis of the MSLP disturbance while C-C* and D-D* are created along the short axis of the MSLP disturbance. The other letters in (a) and (c) represent the intersection of the respective cross sections (I_1 and I_2), the location of a CB and related P_{MIN} (U_1), and a location of compensating subsidence warming (S_1). I_2 also represents an area of compensating subsidence warming associated with a P_{MIN}. Data from the WRF 1-km resolution domain is used to create (a) through (d).

in the 275 to 150 hPa layer. The presence of such high cloud ice content near the tropopause suggests that the heating in this layer is more a result of the depositional growth of ice rather than freezing, which is more efficient at heating the environment (i.e., 2839 J g^{-1} for the former vs. 333 J g^{-1} for the latter, Rogers and Yau 1989). This heating tends to accelerate updrafts and reduce the static stability of the upper troposphere (which also reduces the Rossby radius of deformation). While heating due to freezing is certainly taking place, this heating will be confined closer to the 0°C level and has a smaller impact (but still important) on the thermodynamic changes in the upper troposphere.

Fig. 2.12c shows the deepening and expansion of the meso-α MSLP falls and meso-β surface low within a much more broad area of alternating upward and downward motions in the upper troposphere at 12/0600. Embedded within the meso-β-scale surface low are meso-γ-scale P_{MIN} associated with both CBs as well as compensating subsidence warming. An example of surface pressure falls induced by subsidence warming is marked by "S_1" in Fig. 2.12c while an example of a closed low induced by subsidence warming occurs at the intersection of the two cross sections ("I_2"). The aggregation of individual convective cells into an MCS along the low-level critical latitude (Figs. 2.10e-h) has generated a meso-α-scale outflow (cf. Figs. 2.10d and 2.12c), which expands the cloud ice particles over a meso-α-scale area (Fig. 2.12d). This allows for deposition and freezing to occur over a larger area, expanding the upper-level warming into the feature seen in Figs. 2.10d and 2.12d. The storm-scale outflow is compensated by the development of a closed circulation at 925 hPa with pronounced convergence taking place into the center of

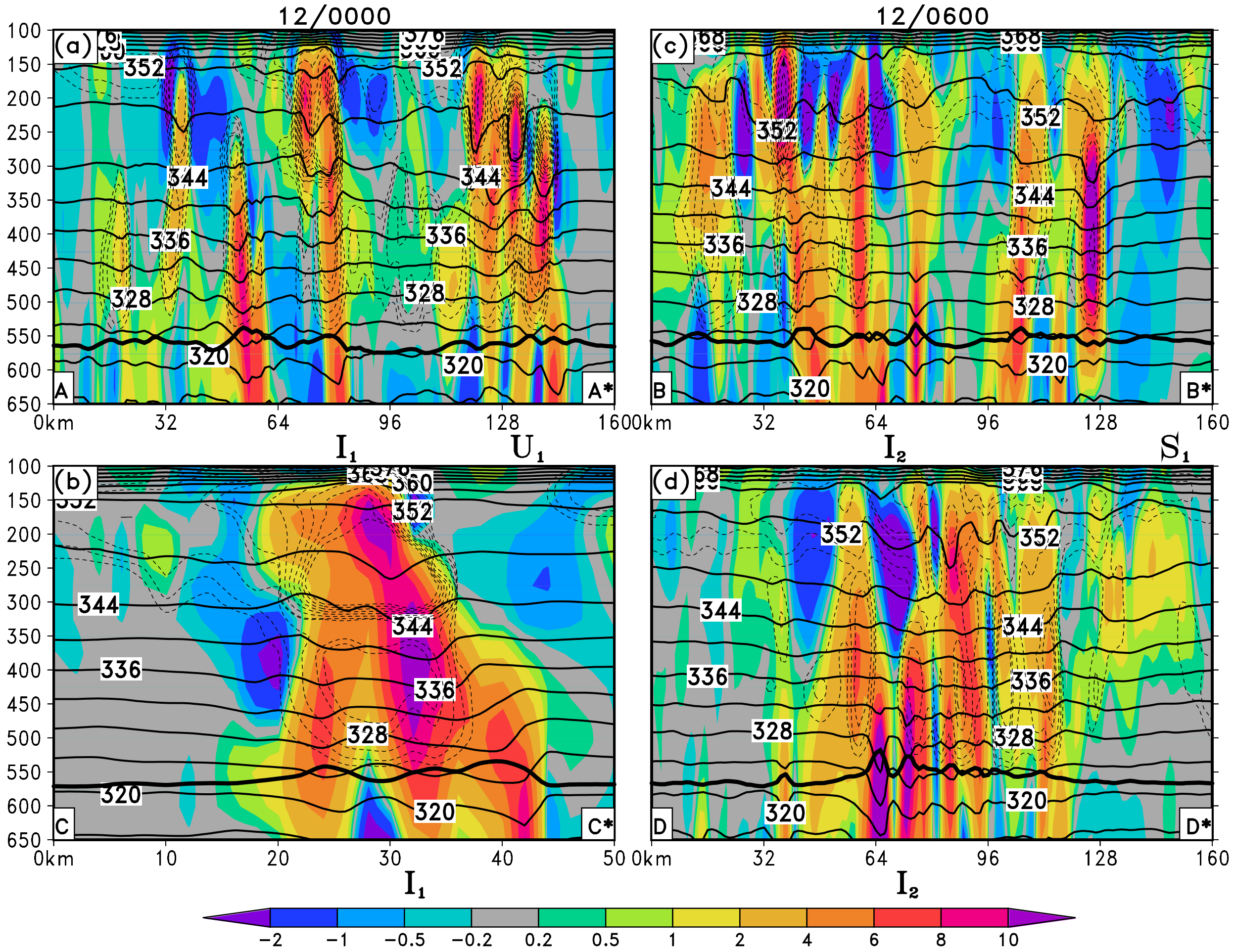

Figure 2.13: (a)-(d) Vertical cross sections of simulated vertical velocity (shaded, m s^{-1}), potential temperature (black contours at intervals of 4K), cloud ice mixing ratio (dashed contours at intervals of .001, .002, .004, .008, .01, .02, .03, .04, .05, .06 and .07 g kg^{-1}) and freezing level (thick black line) for 0000 (a, A-A* and b, C-C*) and 0600 (c, B-B* and d, D-D*) UTC 12 September with the cross section locations given in Fig. 2.12 for their respective times. The letters have the same meaning as in Fig. 2.12, representing the approximate locations of the respective feature. Data from the WRF 1-km resolution domain is used to create the vertical cross sections.

the circulation (Fig. 2.12d). Comparing Figs. 2.12c and 2.12d, one can easily see the similar spatial patterns between the warming in the 275-175 hPa layer and the developing meso-β surface low. Given the prior evidence (Figs. 2.9-2.12), it is not a stretch to believe that the warming aloft is responsible for the meso-β-scale low and meso-α-scale surface pressure falls during the early hours of the simulated SI.

Figs. 2.13c and 2.13d show the same fields as those in the left column, except for 12/0600. Large magnitudes of cloud ice mixing ratios continue to be prevalent in concurrence with notable warming in the 275-150 hPa layer. This warming is further exemplified by the changes to the vertical location of the 352K isentropic contour, which initially resides approximately near 150 hPa at 12/0000, but dips to near 200 hPa as the static stability of the upper troposphere reduces at 12/0600 (Figs. 2.13c,d). While individual CBs are still evident at 12/0600, the notable change from 12/0000 is near the center of the storm (“I_2”) with compensating subsidence in excess of 2 m s^{-1} inducing warming (Figs. 2.13c,d). A second region of compensating subsidence warming is seen on the flank of the meso-β surface low, as marked by “S_1” in Fig. 2.13c. This characteristic hints at the increasing role of subsidence warming associated with an organized MCS.

It is evident that the majority of the upper-tropospheric warming is resultant from latent heating due to deposition and freezing during the early stages of simulated SI. While we attribute the upper-tropospheric warming to a combination of diabatic heating and compensating subsidence warming, with the prior more important than the latter, the obvious rebuttal to this notion is the transient nature of the heating. Certainly, latent heating is a transient feature that is realized through con-

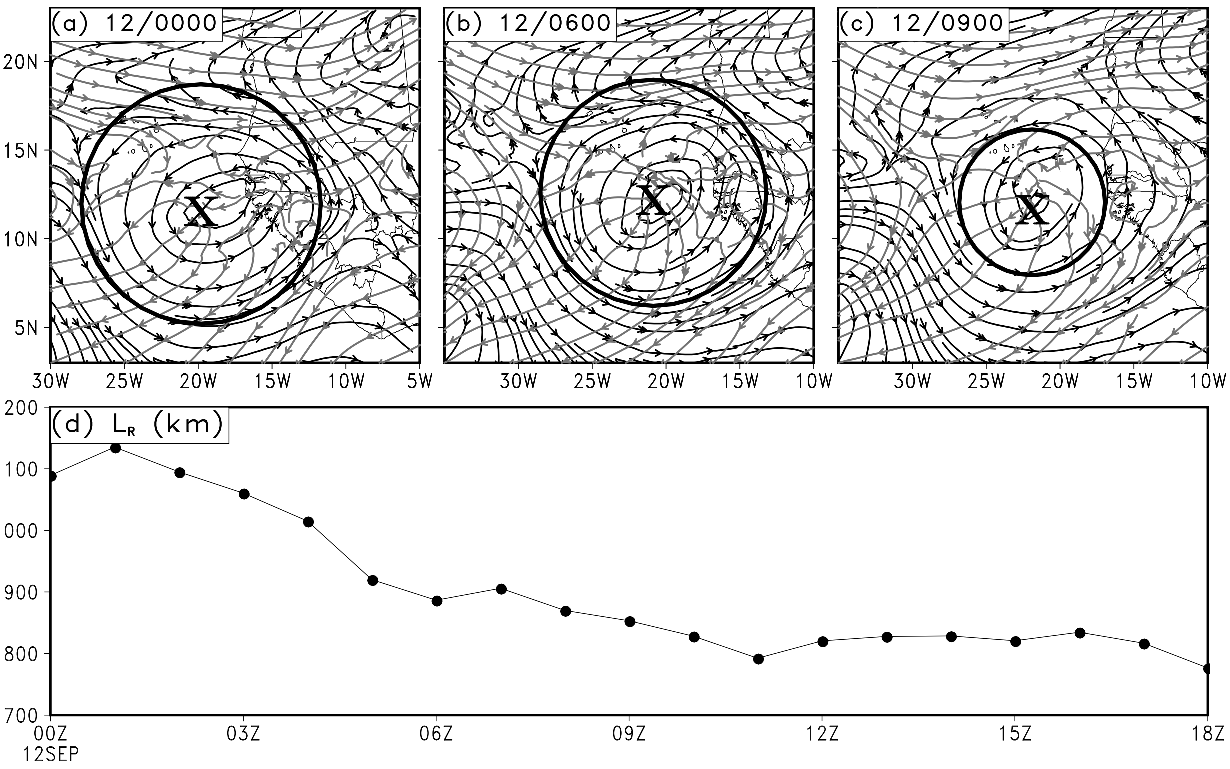

Figure 2.14: (a)-(c) Simulated 600-hPa co-moving streamlines (black) and layer-averaged 275-175 hPa co-moving streamlines (gray) with the Rossby radius of deformation (black circle) and storm center ("X") overlaid for 0000, 0600 and 0900 UTC 12 Sep, respectively. (d) Time series of the Rossby radius of deformation ($\mathrm{L_R} = NH/\eta$) from 0000 to 1800 UTC 12 Sep calculated using 100 km × 100 km area-averaged data from the 3-km resolution WRF simulation. (η is calculated using the layer-averaged absolute vorticity between 1000 and 400 hPa, capturing nearly all the vorticity growth of the developing disturbance as shown in Fig. 2.11. N is calculated using $N = \sqrt{\frac{g}{\bar{\theta}}\frac{d\theta}{dz}}$, where $\bar{\theta}$ is the area-averaged 1000 hPa potential temperature, $\frac{d\theta}{dz}$ is given by the differential of 150 and 1000 hPa potential temperatures and height surfaces, and g is the gravitational constant. H is calculated using $H = R\bar{\mathrm{T}}/g$, where $\bar{\mathrm{T}}$ is the average temperature between 1000 and 150 hPa, R is the gas constant for dry air and g is the gravitational constant.) Data form the WRF 9-km resolution domain were used to create (a) through (c).

vection, its positive buoyancy and the initial gravity wave response to disperse the heating. However, it is quite evident that regardless of an "adjustment period" by which gravity waves try to disperse the heating initially, the warming survives any adjustment period that results in the system-scale signature as shown in Figs. 2.10 and 2.11. Elaborating on this, Fig. 2.14a-c shows the 600-hPa co-moving streamlines (black), 275-175 hPa layer-averaged co-moving streamlines (gray), and the Rossby radius of deformation (circle). In addition, a time-series of the Rossby radius of deformation, $\mathrm{L_R} = NH/\eta$, where N is the Brunt Väisälä frequency, H is the scale height, and η is the absolute vorticity, is given in Fig. 2.14d, showing a decrease in $\mathrm{L_R}$ takes place just prior to and after 12/0600. This reduction is consistent with the intensification of low-level cyclonic vorticity (Fig. 2.11a, Frank 1987) and the reduction of static stability in the upper-troposphere (Fig. 2.13).

For the entire 9-h period in Figs. 2.14a-c, the 600-hPa co-moving circulation is on the order of or greater than the circumference created by $\mathrm{L_R}$. More importantly, the storm-scale outflow in the upper-troposphere extends beyond $\mathrm{L_R}$, allowing for the accumulation of the warming seen in Figs. 2.10-2.13 as the velocity field adjusts to the mass perturbations. It is evident that near the $\mathrm{L_R}$, the outflow shows geostrophic adjustment, with a bend of the streamlines to the right. At 12/0000, when the system-scale outflow is less prevalent and $\mathrm{L_R}$ is at its largest of the three times compared, the warming struggles to become a system scale signature (Figs. 2.12a,b). This quickly changes as an MCS becomes well organized (Figs. 2.10e-h) and a system-scale outflow begins to extend to near $\mathrm{L_R}$ in the hours prior to the simulated TD Julia (Fig. 2.14b). While the storm-scale inertial stability is low (as evidenced in the streamline analyses in Figs. 2.10a-d and 2.14a-c), the reduction of L_R enables the accumulation of the upper-level warming in the core region. It is important for a storm-scale outflow to be present to expand the warming outward over a meso-α-scale area since larger-scale warming is able to induce meaningful, similar sized surface pressure falls. This, however, must be complemented by a reduction of L_R (or an L_R already smaller than the system-scale outflow) to ensure the warming is not dispersed away from the storm center.

2.5 Summary and discussion

The preceding examined the genesis of Hurricane Julia (2010) within an AEW having an initially vertically-tilted closed circulation. This AEW could be traced back to 96 h prior to genesis as a well-defined mid-level circulation. The genesis of Julia occurred shortly after the AEW moved offshore, and was characterized by significant deepening (within 9 h) in MSLP and the rapid growth of an LLV. The generation of the LLV can be tied to the concurrent development of deep convection and its generated vortices, upper-tropospheric warming, a meso-β-scale surface low and meso-α-scale MSLP falls. These features are protected by the AEW through ideas similar to the marsupial pouch paradigm and its low-level critical latitude.

Our model results validate the previous hypotheses that the low-level critical latitude is a preferred location for the initiation and organization of deep convection (including CBs), and the development of meso-β-scale surface lows and vortices. It is shown that convective cells and CBs reside along the AEW critical latitude during the onset of the simulated SI. They rapidly transport water vapor and cloud hydrometeors above the 0°C level, heating the upper troposphere via the latent heat of freezing and deposition. The localized diabatic heating associated with individual convective cells appears to account for the formation of numerous meso-β and meso-γ scale vortices and surface lows. As the convective cells and mesovortices aggregate, a meso-β-scale surface low and an LLV become the dominant mesoscale features within the AEW. The LLV forms through vortex stretching as a result of the presence of deep convection, enhanced PBL convergence associated with the meso-β surface low, and the conglomeration of mesovortices along the low-level AEW critical latitude.

As deep convection intensifies and aggregates into an MCS along the AEW critical latitude, a storm-scale outflow develops aloft, resulting in a meso-α-scale area of high cloud ice content and upper-level warming. The outward expansion of the warmth during the early stages of SI is made possible by latent heating due to deposition and freezing being expanded by the storm-scale outflow beyond L_R. Furthermore, L_R decreases with time as a result of reduced static stability in the upper troposphere and increased cyclonic vorticity in the lower troposphere. With the widespread upper-tropospheric warming, meso-α-scale MSLP falls are hydrostatically induced, creating a low-level cyclonic disturbance needed for stage one of TCG development described in the introduction. It is evident that the meso-α-scale MSLP falls are closely tied to the thermodynamic changes and divergent outflows in the upper troposphere, which in turn, are inherently tied to the development of deep convection along the low-level critical latitude of the AEW. Clearly, the meso-α-scale MSLP falls tend to enhance the PBL convergence for the bottom-up growth of TC-scale rotation.

To summarize, the key elements to this sequence of events are: (i) the initiation, intensification and aggregation of deep convection and its generated vortices along the AEW low-level critical latitude; and (ii) the development of the upper- or high-level warmth, a storm-scale outflow beyond the Rossby radius of deformation, and meso-α-scale MSLP falls. Without either of these, the genesis of the simulated Julia may not occur.

Chapter 3: Ensemble simulations

3.1 Introduction

In chapter 2, the TCG of Julia was explored through the interactions of the large-scale “parent” AEW and mesoscale processes within the AEW circulation. In addition to demonstrating the multi-scale interactions, the importance of upper-tropospheric warming for the development of a mesoscale MSLP disturbance into a TD was explored, alluding to the importance of persistent deep convection and resultant storm-scale outflow.

Even though the previous succinctly demonstrated these features and their connections during the TCG of Julia, it is worthwhile to investigate if the series of events are reproducible using a series of ensemble simulations via perturbed ICs. To further investigate the processes described in chapter 2, 20 66-h cloud-resolving ensemble simulations of the TCG of Hurricane Julia are created using the finest 1-km horizontal resolution. The following will describe the methodology for the ensemble generation, the parametric differences between ensemble members, and dominant disagreements of the ensemble as characterized by ensemble spread and sensitivity.

3.2 Ensemble methodology and setup

The WRF-LETKF system (Miyoshi and Kunii 2012) is used herein because of the successful applications of the LETKF system to other numerical weather prediction models, including the Japan Meteorological Agency (JMA) operational model (Miyoshi et al. 2010). While creating the ensemble forecasts from the perturbed initial conditions, we strive for consistency with the control simulation and its parameterizations, as described previously in chapter 2.

Fig. 3.1 shows the step-by-step approach to generating the ensemble forecasts of Hurricane Julia. The first step is referred to as the "perturbation spin-up", which creates randomly perturbed ICs for the WRF-LETKF system. Specifically, ERA-Interim analyses from 0000 UTC for 20 randomly selected days in the month of August 2010 are used to initialize this spin-up period in order to keep the dynamical consistency with the large-scale flows characteristic of the 2010 north Atlantic hurricane season. Each of the 20 random analyses is treated as "the analysis" of 1/0000, which is 96 h before the WRF-LETKF cycle begins. Using these random ICs, 20 separate WRF forecasts are integrated forward from 1/0000 to 5/0000, creating randomly perturbed initial conditions for ingestion into the WRF-LETKF system. This approach follows closely that used by Miyoshi and Kunii (2012), whose randomly created ICs showed promising results with a similar length spin up.

The second step in Fig. 3.1 is the WRF-LETKF assimilation cycle, which begins at 5/0000 and is run for 120 h until 10/0000, at which time the initialization of the control simulation is valid. Note that an assimilation cycle is needed here

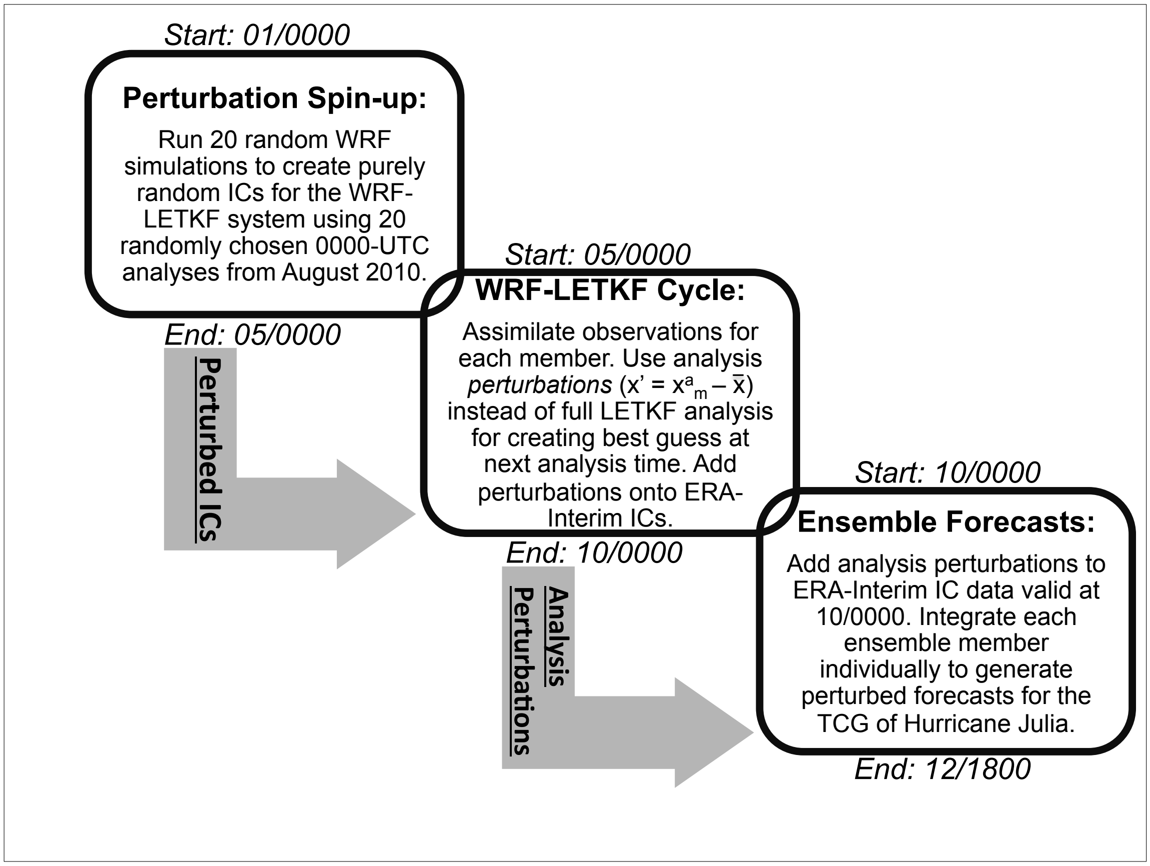

Figure 3.1: Flow chart of the major steps of the ensemble forecast process. The perturbed ICs are created by the "Perturbation Spin-up" step, which starts and ends at 01/0000 and 05/0000, respectively. The WRF-LETKF assimilation cycle is then run for 96 h, terminating at 10/0000. At this time, the 10/0000 analysis perturbations (x') are created by calculating the differences between the ensemble mean ($\overline{x}$) and each member's analysis (x^a_m, where "a" represents analysis and "m" represents each ensemble member, ranging from 1 to 20). The 66-h ensemble forecasts are independently integrated forward to 12/1800, at which time Julia is declared a TS.

because the “analyses of 5/0000” from Step 1 are obtained by integrating from 20 randomly selected ICs. In this study, the assimilation cycle uses observational data from NCEP’s operational global data assimilation system (GDAS); see Appendix A for more details. The main goal here is to generate realistic perturbations of the atmospheric state at a time just prior to the TCG of Julia. Using these perturbations, ensemble forecasts will yield a spread of solutions of TCG, which are then investigated to identify the fundamental processes (and related perturbations) responsible for the evolution of the disturbance into TD Julia.

For Step 2, a single 27-km resolution domain is centered on the region of interest (“LETKF”; Fig. 3.2) with the WRF-LETKF system creating analyses every 6 h over the 96-h period. The relevant WRF model parameterizations used in the assimilation cycle include: (i) the WRF Single-Moment Microphysics Scheme (WSM) 5-class cloud-microphysics scheme (Hong et al. 2004); (ii) the Kain-Fritsch convective scheme (Kain 2004); (iii) the Rapid Radiative Transfer model (RRTM) longwave radiation scheme (Mlawer et al. 1997); (iv) the Dudhia shortwave radiation scheme Dudhia (1989); and (v) the Yonsei University (YSU) PBL scheme (Noh et al. 2003). All 20 members are given the same boundary conditions, which come from 6-hourly ERA-Interim analyses. Even though the members are identical at the boundaries using this method, substantial differences between the members do exist in the central region of the domain, as was also found by Miyoshi and Kunii (2012).

A significant difference between the assimilation cycle used herein and by Miyoshi and Kunii (2012) revolves around how the WRF-LETKF ensemble analyses are used in the cycle. Miyoshi and Kunii (2012) overwrites the initial conditions from

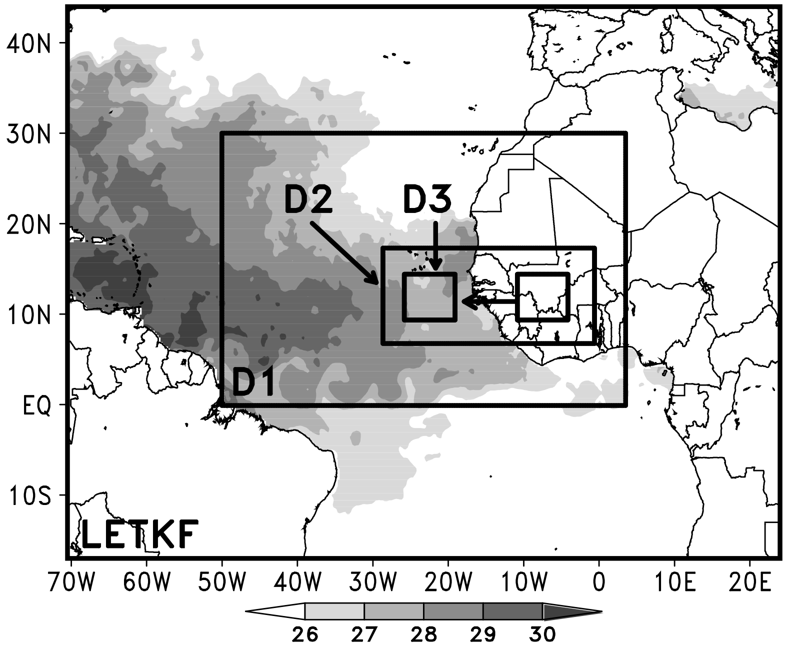

Figure 3.2: WRF domain setup for both the WRF-LETKF cycle ("LETKF") with the horizontal resolution of 27 km and the subsequent nested forecast domains of D1, D2, and D3 respectively, with the horizontal resolutions of 9, 3 and 1 km. D3 is a moving domain with the starting and ending positions marked by the respective boxes. NOAA OI SST data is shaded at intervals of 1°C valid at 0000 UTC 10 Sep.

the WRF pre-processing system (WPS) with the WRF-LETKF system analyses, leaving the WPS-created boundary conditions intact for each assimilation period. In contrast, the current study creates initial and lateral boundary conditions from ERA-Interim analyses using the WPS system, but only uses the analysis perturbations for each ensemble member (e.g., $x_t^{\prime(m)} = x_t^{a(m)}$ - $\overline{x}_t^a$, where m is the ensemble member, a stands for analysis and t represents the analysis time) from the WRF-LETKF system. These perturbations are added to the WPS-processed ERA-Interim initial conditions (which are deterministic in nature), creating perturbed initial conditions for the next assimilation period. Given that the main goal of running the WRF-LETKF cycle is to generate realistic perturbations of the atmospheric state, it is unnecessary to keep the full analysis of each ensemble member. This rationale results in the ensemble perturbations being added to the ERA-Interim data for each 6 hourly analysis period. Obviously, the ensemble perturbations at 10/0000 are of the utmost importance since these perturbations create a spread of perturbed initial conditions centered on the control simulation, which is initialized from the 10/0000 ERA-Interim data. Our method "re-centers" the ensemble perturbations about the ERA-Interim analysis every 6 h, and thus, the perturbations are nearly in balance with ERA-Interim analyses in addition to the ensemble mean. To ensure proper balance (and centering) of the perturbations, the ensemble mean analysis was compared to the ERA-Interim analysis at various times, including 10/0000 (not shown). These comparisons revealed that both analyses were nearly identical with horizontal resolution being the only notable difference (e.g., 27 km versus 0.7° for the WRF-LETKF and ERA-Interim analyses, respectively).

The WRF-LETKF-generated (perturbed) ICs are integrated 66 h forward to 12/1800 to produce ensemble forecasts for the TCG of Hurricane Julia, whose output can be compared with the control simulation discussed in chapter 2. These ensemble forecasts are made using the same domain and model physics setup as the control, but with the addition of the 27-km resolution domain. The WRF-LETKF domain ("LETKF", Fig. 3.2) supplies the initial and lateral boundary conditions to the inner domains, having the same 9-, 3- and 1-km horizontal resolutions as the control simulation (D1, D2, and D3, respectively; Fig. 3.2). The lateral boundary conditions of the 27-km resolution domain are supplied by the ERA-Interim analysis, like the assimilation cycle. SSTs are supplied by the NOAA OI high-resolution SST data set (Reynolds et al. 2007) valid at 10/0000, keeping consistency with the control simulation. The only difference in the WRF model setup from the WRF-LETKF assimilation cycle is the use of the Thompson Graupel 2-moment (Thompson et al. 2008) microphysics scheme, the same scheme used in the control simulation.

3.3 WRF-LETKF cycle and ensemble forecast results

Before examining in depth the results from the ensemble forecasts, it is fruitful to examine some characteristics of the WRF-LETKF cycle in addition to the track and intensity results from the ensemble as a whole. For the remainder of this paper, TCG is defined in the same fashion as that described in chapter 2, i.e., the time at which a closed MSLP isobar of sufficient size and intensity on the standard 4 hPa contouring interval occurs. This time will be assessed in comparison to the time the NHC declared Hurricane Julia a TD, 12/0600. Prior to this time is referred herein to as TCG while after is referred to as the SI period. Because of the above definition for TCG, MSLP rather than the relative vorticity field (unlike previous studies) will be used to examine the intensity of the ensemble-simulated storms. The term "predictability" is defined in terms of how well the ensemble solutions capture the TCG event in comparison to the NHC estimates, and by the mechanisms that yield any ensemble disagreements at the time of TCG. That is, predictability is not thought of in its common form, which is in terms of how much lead time a particular forecast alerts that TCG is going to occur.

3.3.1 Results from the WRF-LETKF cycle

Unlike other data assimilation studies which strive to quantify and thoroughly describe the performance of the data assimilation system, we are more concerned with the creation of realistic ensemble perturbations. To this end, Fig. 3.3 shows the domain-averaged analysis spread at $\sigma = 0.59712$ (approximately 600 hPa) for u, v, T, and q_v from 05/0600 to 10/0000. This level is used to examine ensemble spread because near it the AEW cyclonic vorticity and related circulation field are maximized prior to TCG (see chapter 2). The ensemble spread of all variables decreases rapidly during the first 12 h of integration and then remains nearly constant, with further decreases during the last 6-h assimilation period, alluding to the creation of reasonable flow-dependent ensemble perturbations. The ensemble spread of approximately 0.4 m s^{-1} for u (Fig. 3.3a) is consistent with experiments using both

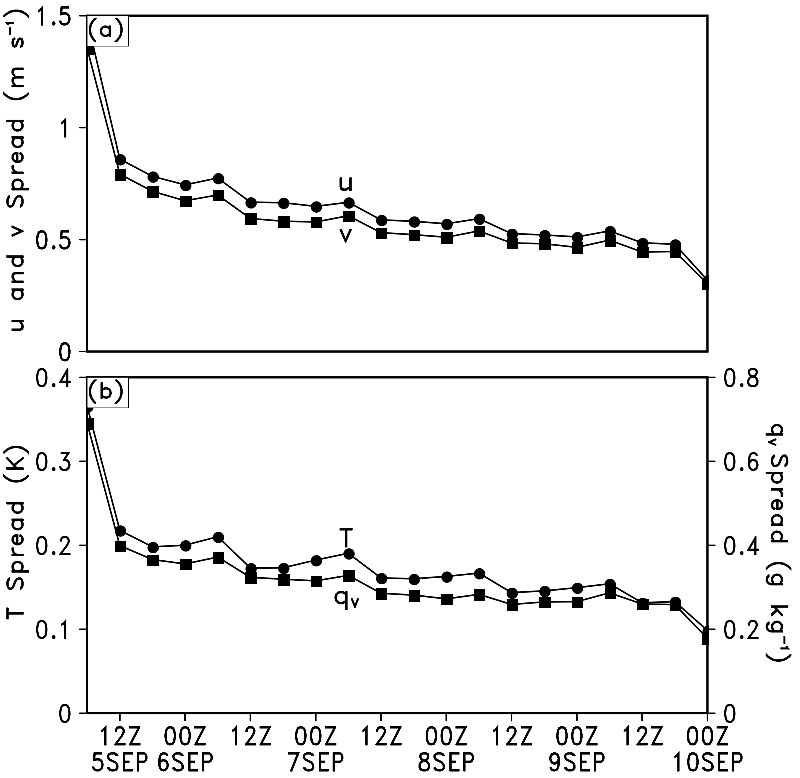

Figure 3.3: Time series of ensemble spreads during the period of 0600 UTC 5 to 0000 UTC 10 Sep for (a) the zonal wind (u, m s^{-1}) and meridional wind (v, m s^{-1}); (b) temperature (T, °C) and water vapor mixing ratio (q_V, g kg^{-1}) at $\sigma = 0.59712$, approximately 600 hPa, that are averaged over the entire WRF-LETKF domain shown in Fig. 3.2.

adaptive and globally constant multiplicative inflation in Miyoshi and Kunii (2012).

3.3.2 Ensemble forecast track and intensity

The tracks from the 20-member ensemble forecasts are shown in Fig. 3.4, as compared to the control simulation (black, squares) and best fixes from the NHC (black, circles). The same tracking methodology as that in chapter 2 is used, with the track initially being generated using 600- and 700-hPa circulation centers in conjunction with large absolute vorticity. The tracking is then shifted to the P_{MIN} center of sufficient spatial size once it forms. This transition varies between ensemble members and could lend to some of the track spread seen in Fig. 3.4.

Overall, the track of the AEW prior to coastal transition is well agreed upon by nearly all members, with the majority of the track differences occurring near the end of the 66-h simulation. Interestingly, the outlying southern-most solution after coastal transition is the control simulation, with an overall track error of 173 km as compared to the best fixes. The ensemble mean track improves upon the control simulation by over 40 km, with a mean track error of 131 km, while the member with the best track has an average track error of just 106 km. Substantial variability in the track exists after 12/0600, which is in agreement with the strength differences of the forecast storms among the ensemble members to be shown in the next. Fig. 3.5 shows the time series of the storm intensities in terms of P_{MIN} and V_{MAX} from the 20 ensemble members, control simulation (black, squares) and NHC estimated intensity (black, circles). Additionally, the ensemble spreads for P_{MIN} and V_{MAX} are also plotted in terms of sample standard deviation (dashed lines). Obviously, the ensemble spread of each parameter increases as the integration progresses, reaching maximums of approximately 2.5 hPa and 4 m s^{-1}, respectively, at 12/1800. Eighteen out of the 20 members produce P_{MIN} below 1007 hPa from the NHC estimated P_{MIN} at 12/0600, while the remaining 2 members simulate a storm with P_{MIN} of 1007 hPa, agreeing with the NHC estimated intensity. This large bias for a stronger storm at 12/0600 (with an ensemble mean P_{MIN} of 1004 hPa), hints at the possibility that the NHC estimated intensity is too weak by 2 – 3 hPa, but such a difference is probably

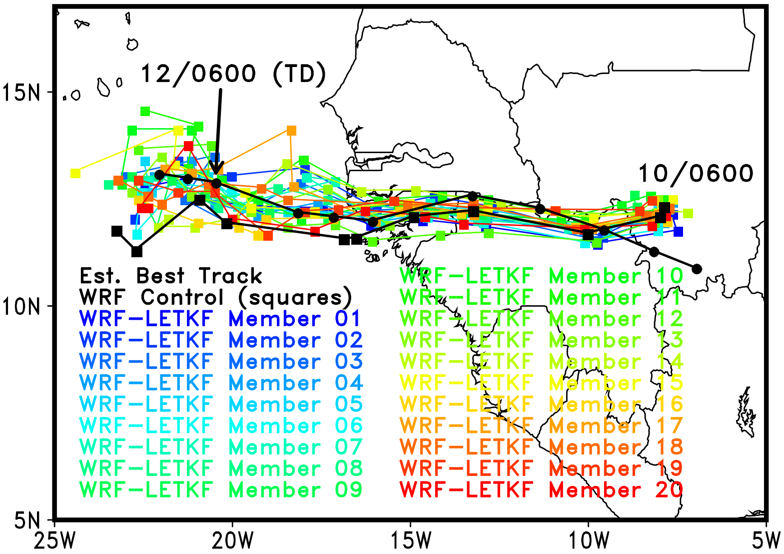

Figure 3.4: Tracks of each WRF-LETKF ensemble member (colored by member) as compared to the control simulation (black, squares) and best NHC estimated (black, circles) tracks valid from 0600 UTC 10 to 1800 UTC 12 Sep.

within the range of accepted error. About 16 out of the 20 members are stronger than 1005 hPa at 12/1800, with the strongest member reaching a P_{MIN} of 999 hPa. In contrast, 2 out of the 20 members are weaker than 1005 hPa at 12/1800, while the final two members have the same NHC estimate of 1005 hPa. Thus, we may state that the TCG of Hurricane Julia is highly predictable in terms of P_{MIN}, with nearly all members depicting a TD-like intensity at 12/0600 and a TS-like intensity at 12/1800. It is worth noting that the true "predictability" of the TCG event could be found by running simulations using the perturbed ICs created without any data assimilation. By doing so, the theoretical upper and lower bounds of P_{MIN} could be identified, painting a clearer picture for how predictable the ensemble with data assimilation is.

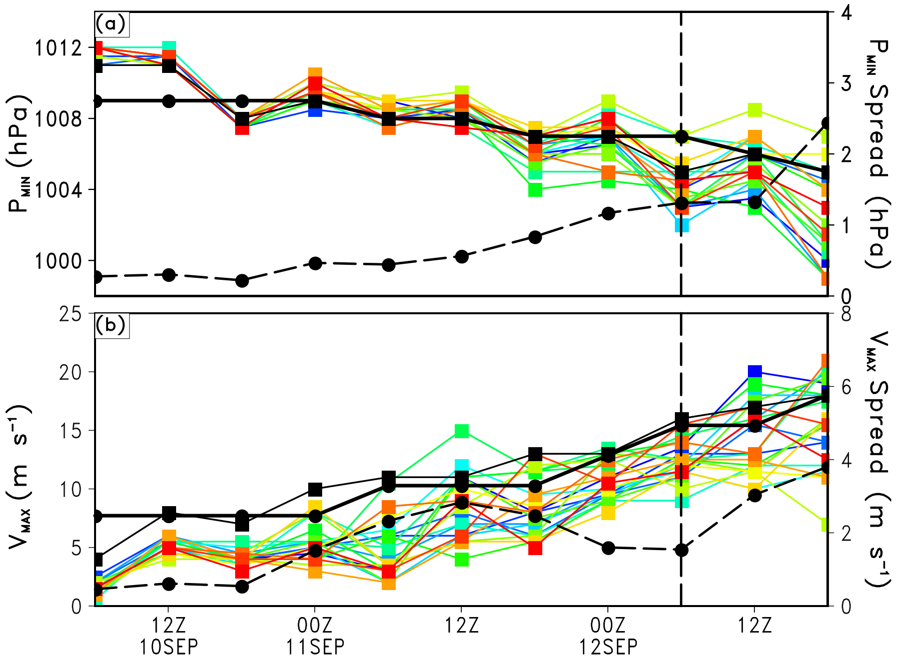

Figure 3.5: Time series of the intensity of Hurricane Julia in terms of (a) P_{MIN} (hPa) and (b) V_{MAX} (m s^{-1}) from each WRF-LETKF member, the control simulation (black, squares) and the NHC estimated (black, circles). Dashed lines in (a) and (b) represent the ensemble spread (i.e., sample standard deviation) of P_{MIN} and V_{MAX}, respectively, while the colored lines have the same meaning as in Fig. 3.4. The vertical dashed lines in (a) and (b) represent the time of TCG as determined by NHC.

3.3.3 Selection of developers and non-developers

Given the spread among the 20 members, it is desirable to examine which member reproduces the TCG of Julia too strongly or weakly, as well as which members have the best and worst track. Here, the best (and worst) track is selected using the overall average track error when comparing to the NHC estimated track. Similarly, the best (and worst) members for intensity are based purely on the members' $\mathrm{P_{MIN}}$, as compared to the NHC estimated $\mathrm{P_{MIN}}$, in addition to the storm intensity when declared a TD and a TS. We decide to use $\mathrm{P_{MIN}}$ rather than $\mathrm{V_{MAX}}$ to identify these members since its time series best defines the schism between developers and non-developers (see Fig. 3.5a). More attention will be given to the intensity of individual members rather than the track because TCG marks a distinction between intensity changes, not track changes.

Fig. 3.6 shows the tracks and intensities for the member with the best track (member 4, orange), the best intensity (member 7, green), as well as the member with the strongest storm (member 10, red) and weakest storm (member 14, blue). Member 7 compares favorably to the NHC (black circles), with an average absolute intensity error in $\mathrm{P_{MIN}}$ of 0.95 hPa. Further supporting its selection as the member who best replicates NHC estimates, member 7 has the same $\mathrm{P_{MIN}}$ as the NHC estimate at TD and TS times in conjunction with a total track error of 140 km.

In contrast to the "best" members, the member with the worst track error is also the member with the strongest overall storm (member 10, red line in Fig. 3.6). The overall track error of 246 km is significantly above the ensemble mean and

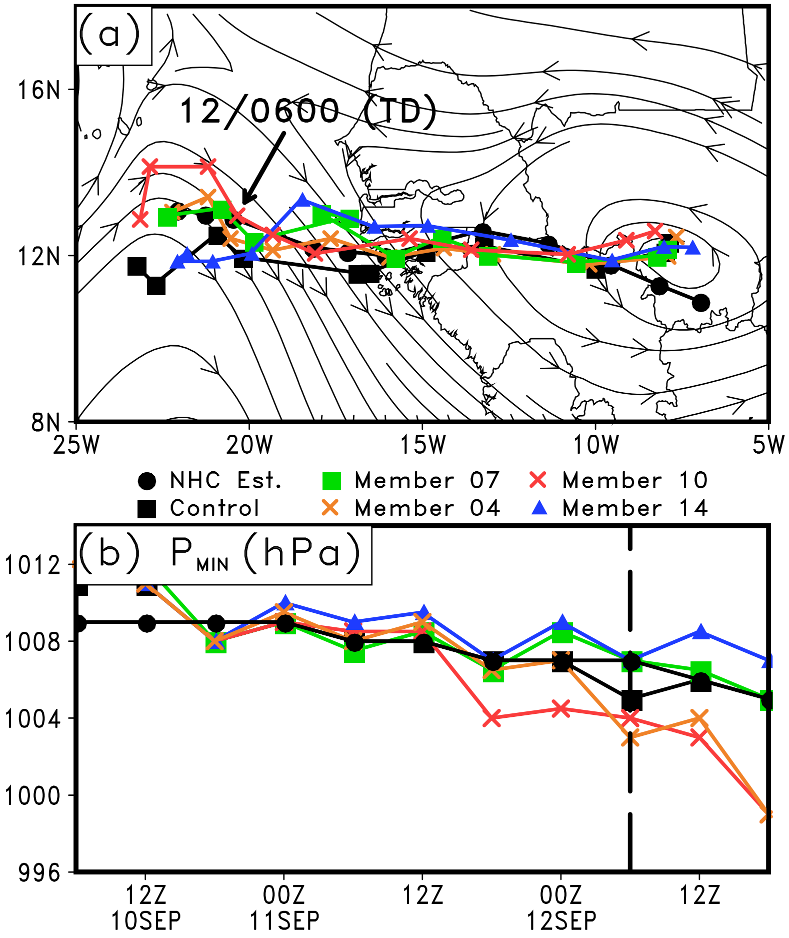

Figure 3.6: (a) The tracks from the member with the best track (member 4, orange), best intensity (member 7, green), the weakest storm (member 14, blue), and the strongest storm (member 10, red) in comparison to the WRF control simulated (black, squares), and NHC estimated (black, circles) superimposed with ERA-Interim 600-hPa co-moving streamlines valid at 0600 UTC 10 Sep. (b) Time series of the P_{MIN} (hPa) of each of the members in relation to the WRF control simulated and NHC best estimates. Colored lines in (b) have the same meaning as in (a). The dashed line in (b) represents the time of TCG as estimated by NHC.

control track errors, with most of this track error occurring later in the integration. Of interest is the time series of $\mathrm{P_{MIN}}$ given in Fig. 3.6b, showing that member 10 (red) deepens 4.5 hPa between 11/1200 and 11/1800, reaching a $\mathrm{P_{MIN}}$ of 999 hPa at 12/1800. Contrasting member 10 is member 14, a non-developer (blue line), which never develops into a TD and ends the 66-h integration with a $\mathrm{P_{MIN}}$ of 1007 hPa at 12/1800. Both members 10 and 14 are used in conjunction with member 7 and the control simulation to assess the dynamic and thermodynamic differences taking place during TCG.

The members of interest (7, 10, and 14) show differences with respect to spatial cloud patterns when compared to the observed *METEOSAT-9* IR imagery (cf. Figs. 2.4 and 3.7). After 12 h into the integration (Figs. 3.7a,e,i,m), little differences exist between the members with minimal convective initiation. By 11/1200 (Figs. 3.7b,f,j,n), differences between the members start to emerge, but all fail to capture the large, round-shaped MCS found in the observed IR (Fig. 2.4b). At the time of TCG (Figs. 3.7c,g,k,o), only member 10 (the strongest developer) and the control simulation compare favorably with the observed *METEOSAT-9* IR image (Fig. 2.4c). This supports our initial postulation that the NHC $\mathrm{P_{MIN}}$ estimate at 12/0600 might be too weak since (i) the strongest member compares favorably to the observed cloud spatial patterns; and (ii) the member with comparable $\mathrm{P_{MIN}}$ to the NHC estimate (member 7) depicts weak, sporadic convection at the same time. By 12/1800, the two weaker members (Figs. 3.7d,l) depict a more coherent MCS, but do not exhibit the cyclonic circulation in the cloud fields seen in member 10 (Fig. 3.7h), the control simulation (Fig. 3.7p) and the observed (Fig. 2.4d). Overall,

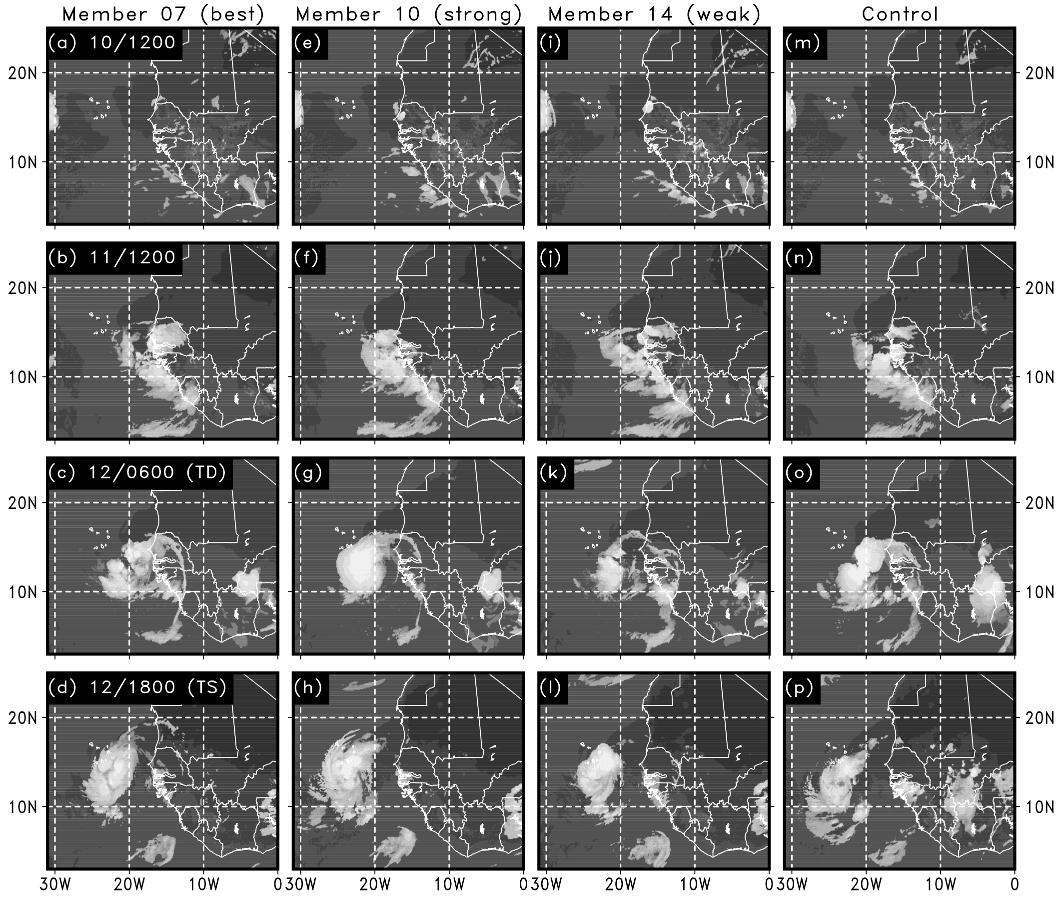

Figure 3.7: Comparison of WRF-derived brightness temperature (K) from members 7 (a-d, best intensity), 10 (e-h, strongest developer), 14 (i-l, non-developer) and the control simulation (m-p) at the same times as in Fig. 2.4. Data from the 9-km resolution simulation were used.

member 10 and the control simulation have the most realistic representation of the cloud field associated with the AEW and subsequent TS.

3.4 Parametric differences between ensemble members

In order to isolate what causes the intensity differences shown in the preceding section, we examine the differences between the developers and non-developers from a synoptic and mesoscale viewpoint. Of particular interest is the initiation of deep convection and its persistence during TCG, which have previously been studied by Sippel and Zhang (2008) and Hopsch et al. (2010) in terms of CAPE and tropospheric moisture content. In addition, we investigate the differences in upper-tropospheric processes, including upper-level warming and changes to the outflow layer, as previously emphasized by Zhang and Zhu (2012) and the work presented in chapter 2.

3.4.1 Differences in the upper-level warming

Following Chen and Zhang (2013) and Zhang and Zhu (2012), Fig. 3.8 presents the time series of the area-averaged cloud ice content and relative warming with respect to the vertical temperature profile at 11/0600, at which time, all members have a distinct midlevel circulation associated with AEWs over land. The relationship between the warming aloft and MSLP pressure changes are shown in Fig. 3.9, with the 200-hPa temperatures greater than -53°C shaded, and the MSLP field overlaid.

It is obvious that the two stronger storms have a burst of warming exceeding 1.5°C just before and at the onset of TCG (Figs. 3.8b,d). Prior to this burst, warming in excess of 0.5°C exists in the 500-150 hPa layer, beginning just after 11/1200. This warming layer deepens and intensifies in both member 10 and the control approaching their respective TCG times, with member 10 exhibiting warming in excess of 1.5°C at 11/1800 (Fig. 3.8b). The 11/1800 time also marks the first time when

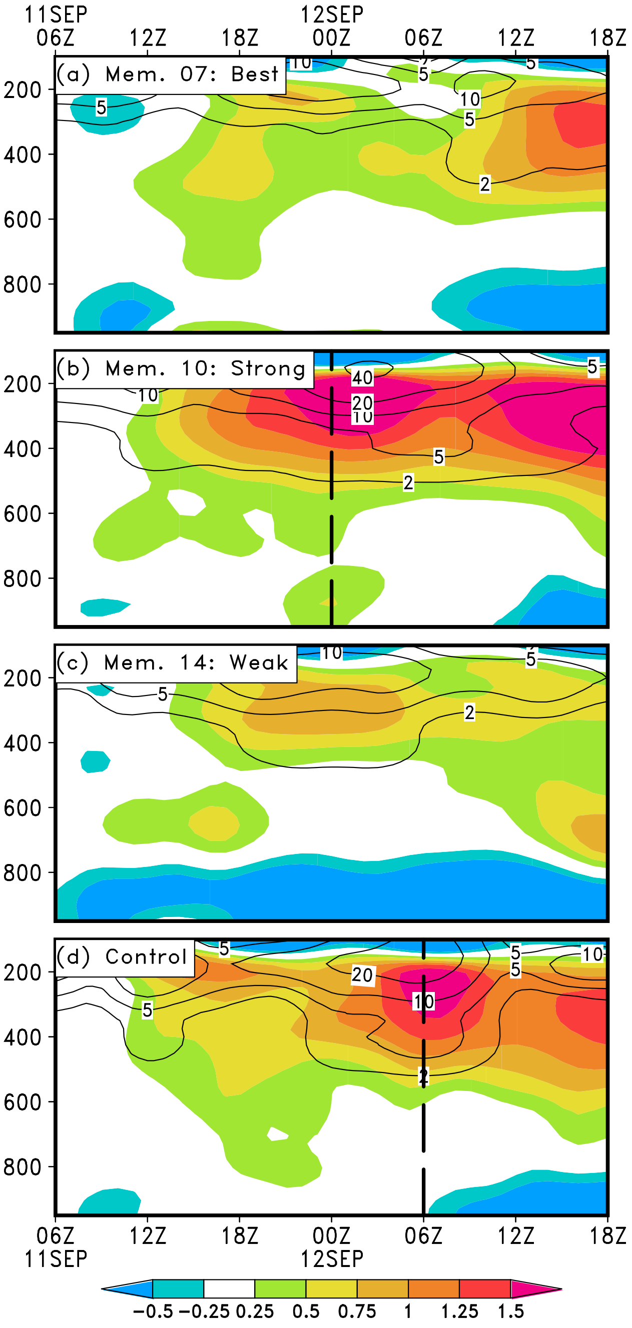

Figure 3.8: Time-height cross section of the temperature differences from the 30-h simulated values (valid at 0600 UTC 11 Sep, shaded, °C) and cloud ice mixing ratio (contoured at 2, 5, 10, 20, and 40 $\times 10^{-4}$ g kg^{-1}) averaged over an area of 100 km × 100 km surrounding the storm center from hourly 3-km resolution domains associated with members 7 (a, best), 10 (b, strongest developer) and 14 (c, non-developer) and the control simulation (d). Vertical dashed lines represent the time of TCG in ensemble member 10 and the control; member 7 undergoes TCG at 1800 UTC 12 Sep.

a distinguishable P_{MIN} is found in member 10, directly beneath a meso-β-scale area of temperatures exceeding -52.5°C at 200 hPa (Fig. 3.9b). In contrast, the control simulation shows a broad area of lower MSLPs over the ocean with no appreciable concentration of warmth at 200 hPa (Fig. 3.9d). Member 10 undergoes TCG first, warming over 0.5°C with an accumulation of high cloud ice content between 11/1800 and 12/0000 (Fig. 3.8b). During this period, an expansion of the warmth at 200 hPa over the meso-α scale occurs due to the development of a storm-scale outflow. This meso-α area of warmer temperatures hydrostatically induces similar sized MSLP falls, while directly beneath the warmest 200-hPa temperatures the meso-β P_{MIN} seen in Fig. 3.9b intensifies into the TD in Fig. 3.9f.

The control simulated storm undergoes TCG between 12/0000 and 12/0600, with an increase in the upper-level warming from 0.75°C to in excess of 1.5°C, combined with an accumulation of large cloud ice content (Fig. 3.8d). In a fashion similar to member 10, the control also shows the development of a meso-β-scale P_{MIN} beneath 200-hPa temperatures between -53 and -52.5°C (Fig. 3.9h). This warming expands markedly in a region characterized by storm-scale outflow, inducing MSLP falls on a meso-α-scale area in addition to generating the meso-β surface low (TD Julia) at 12/0600 (Fig. 3.9l).

After their respective TCG, both member 10 and the control simulation depict a weakening of warming within 100 km of the storm center, followed by a re-strengthening toward the end of the simulations (Figs. 3.8b,d). This weakening is more apparent in the control, with the 200-hPa temperatures in excess of -52.5°C contracting between 12/0600 and 12/1800 (Figs. 3.9l,p,t). An increase in VWS to

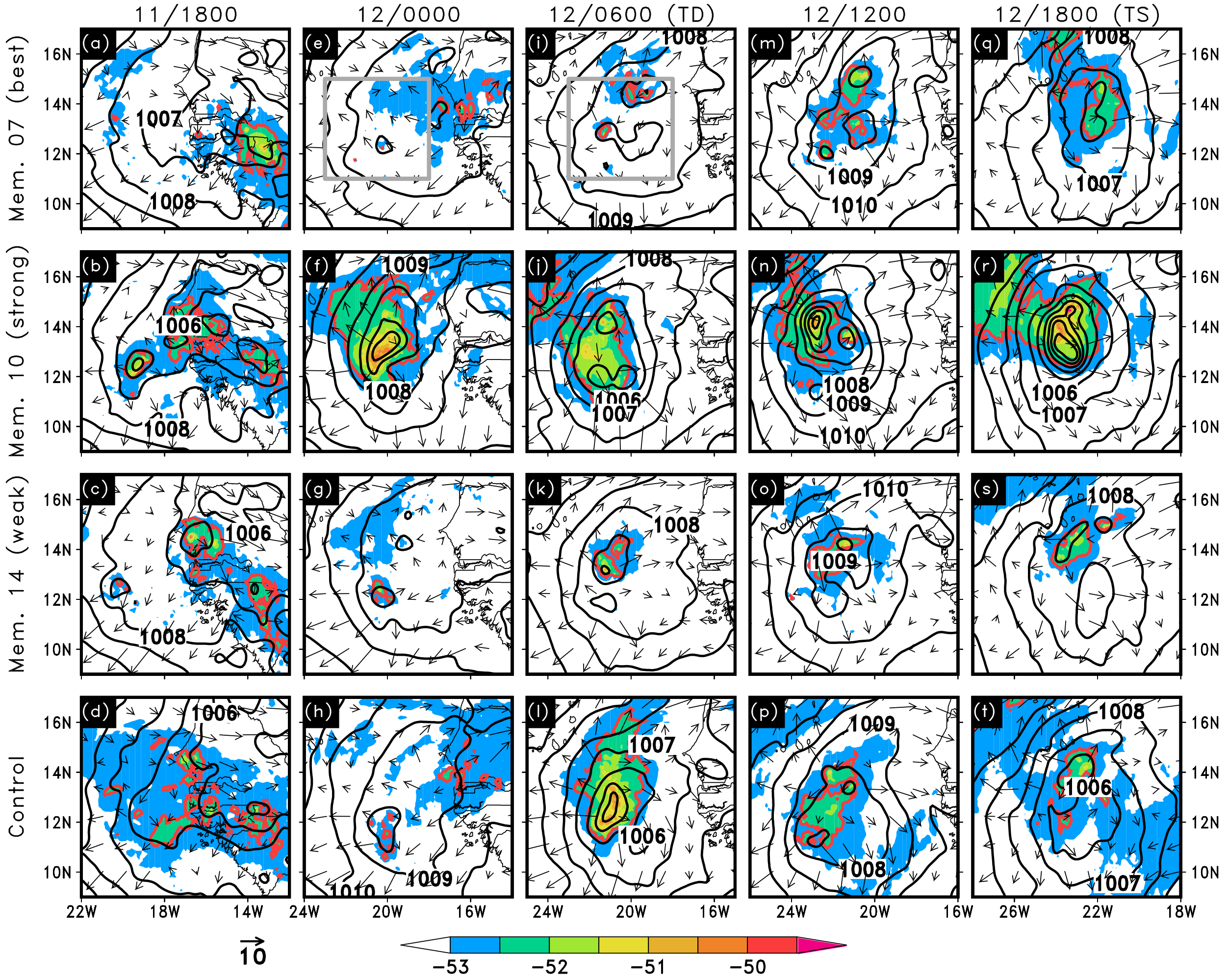

Figure 3.9: Comparison of the 200-hPa temperature (shaded, °C), MSLP (contoured at intervals of 1 hPa), and co-moving wind vectors (reference vector is 10 m s^{-1}) from ensemble members 7 (first row), 10 (second row), 14 (third row) and the control simulation (fourth row) that are valid at 1800 UTC 11, 0000 UTC, 0600 UTC, 1200 UTC, and 1800 UTC 12 Sep, respectively. The -52.5°C isotherm at 200 hPa is contoured bold red to show areal changes of the warming with time. The gray boxes in (e) and (i) represent the area used for the averages in Figs. 3.10 and 3.12. Data from the 9-km resolution simulation are used.

between 8 and 12 m s^{-1} in the 400-150-hPa layer (Fig. 3.11c) in the control can partially explain the weakening of the warming. Meso-α MSLP falls at the surface continue between 12/1200 and 12/1800 in member 10, with the warmest regions at 200 hPa characterized by a meso-β-scale surface low present directly beneath (Figs. 3.9n,r). At 12/1800, temperature differences again intensify to greater than 1.5°C (Fig. 3.8b), with a 999-hPa TS-like meso-α surface low directly beneath the warm region at 200 hPa (Fig. 3.9r).

On the other hand, the two weakest members struggle to develop such significant upper-level warming (Figs. 3.8a,c). For example, the majority of the time series of member 7, which is the best as compared to NHC estimates, is dominated by sporadic meso-β-scale warming less than 1.0°C with cloud ice content less than half that of the strongest developer. It is not until just prior to 12/1200 that persistent warming develops in a layer between 600 and 150 hPa, with a notable increase in cloud ice content over the same depth. This warming intensifies by the end of the simulation, finally reaching 1.25°C between 12/1200 and 12/1800, undergoing TCG. Such sporadic warming prior to 12/1200 supports the lack of a persistent P_{MIN} center (Figs. 3.9a,e,i), since the warming is unable to hydrostatically induce mesoscale MSLP falls. This inability can be attributed to the lack of a storm-scale outflow in contrast to the stronger developers, among other attributes shown in following sections (cf. Figs. 3.9e and 3.9f).

Member 14 is unique in that persistent warming in excess of 0.5°C in association with moderate cloud ice content between 500 and 200 hPa exists for just over a 24-h period, but a TD never develops (Fig. 3.8c). The core of this warming exceeds 0.75°C from approximately 11/1800 to 12/0600 (Fig. 3.8c) with an identifiable meso-β-scale P_{MIN} evident beneath the warmest temperatures at 200 hPa (Figs. 3.9c,g,k). The warmest temperatures are localized however, inhibiting the growth of a TD-scale P_{MIN}. The presence of a weak storm-scale outflow suppresses the expansion of the warmth resulting in minimal meso-α-scale MSLP falls. After 12/0600, the warming near the storm center weakens below 0.75°C (Fig. 3.8c) with a similar response seen in the 200-hPa temperature field (Figs. 3.9o,s).

Since we have identified meaningful differences in MSLP and upper-tropospheric temperatures from the 4 selected simulations, it is worthwhile to see if the differences also exist in the ensemble as a whole. To this end, Fig. 3.10 compares the area-averaged 400-150 hPa layer-averaged temperatures and MSLP among all the ensemble members; the former parameter is chosen based on the general depth of the warming layer of the 4 storms in Fig. 3.8. It is evident that the majority of members at 12/0000 have area-averaged MSLP between 1010 and 1009 hPa with corresponding upper-tropospheric temperatures at or below -37°C (Fig. 3.10a). A clear negative relationship, with correlation coefficient of -0.768, exists between the parameters, alluding to members with warmer upper-tropospheric temperatures also having lower area-averaged MSLP. This correlation, however, has been influenced by the outlying members, although the general negative trend still exists within the ensemble cluster. As more ensemble members strengthen, the negative correlation becomes more robust, with a Pearson's correlation of -0.937 (Fig. 3.10b). Such a strong negative correlation implies that the fast developers (e.g., those undergoing TCG) have prominent upper-tropospheric warming. This is supported by the in-

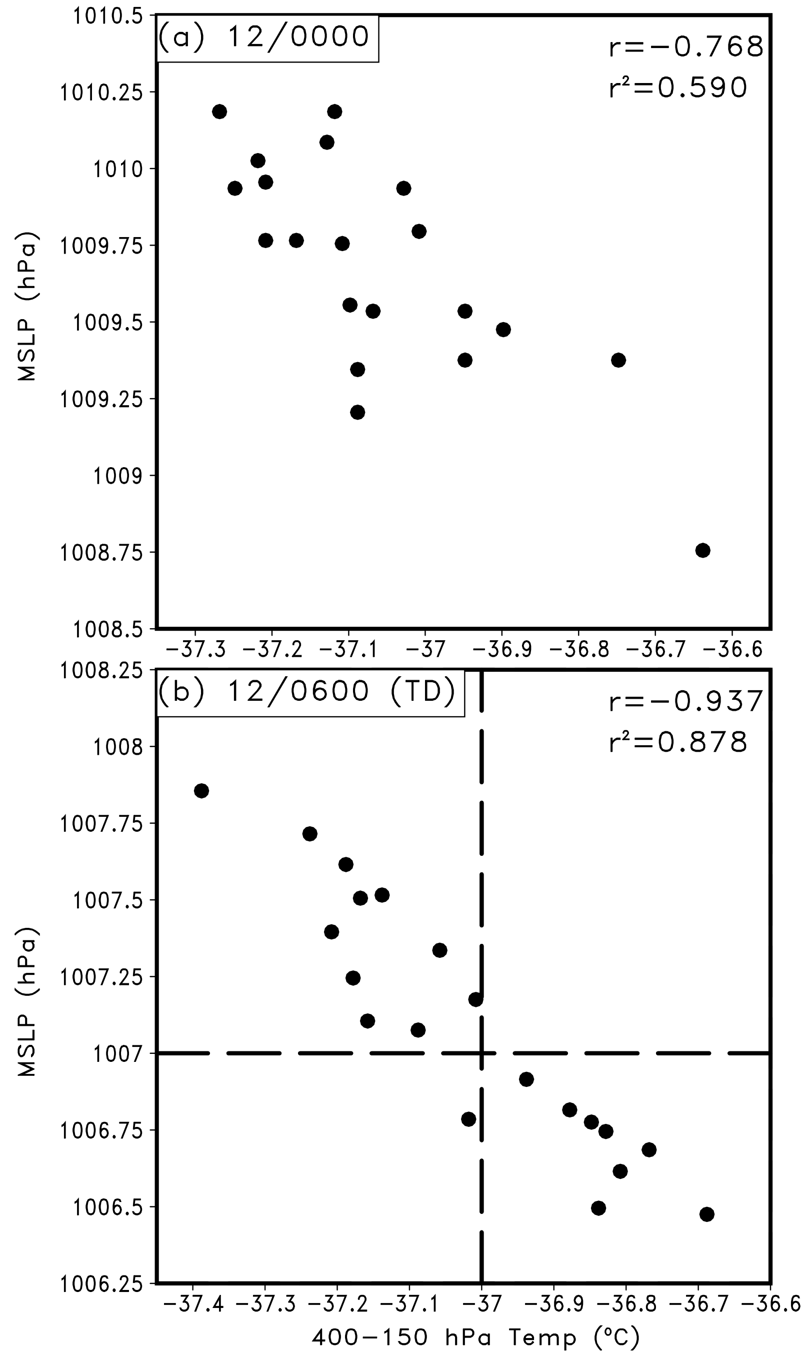

Figure 3.10: Scatter plots of the 500 km × 500 km area-averaged 400-150 hPa layer-averaged temperature (°C; x-axis) versus MSLP (hPa; y-axis) from each ensemble member at (a) 0000 and (b) 0600 UTC 12 Sep, respectively (see Figs. 3.9e,i for the areas used for averaging). The Pearson's correlation coefficient (r) and the coefficient of determination (r^2) are calculated at each time. The vertical and horizontal dashed lines in (b) represent the schism between fast- and slow-developing ensemble members. Data from the 3-km resolution simulation are used in the averaging.

creased spread in both area-averaged upper-tropospheric temperatures and MSLP, as a large cluster of members has area-averaged MSLP below 1007 hPa and 400-150 hPa layer-averaged temperatures of above -37°C. A clear schism between the developers and non-developers at 12/0600 can easily be identified, as indicated by the vertical and horizontal dashed lines in Fig. 3.10b. Thus, the impact of upper-level warming on MSLP changes can be seen from the entire ensemble, with notable differences between faster and slower (or non-) developing members. This is especially evident at 12/0600, as a cluster of members undergo or are in the process of TCG. Obviously, this strong linear relationship is just hydrostatic balance, though such a relationship between the upper and lower troposphere has not been depicted before during TCG.

The difference in upper-tropospheric warming between the members is also consistent with observations taken during PREDICT, although the warming may sometimes occur in the midtroposphere (Zhang and Zhu 2012). Komaromi (2012) investigated composite dropsondes during PREDICT for developing and non-developing storms in comparison to the mean temperature profile from the campaign. The work shows that 1.0 to 2.0°C warm anomalies in developing storms occur 0-24 h prior to TCG within 200 km of the storm center. The work also states that negative anomalies of 0.5 to 1.0°C occur for non-developing storms when compared to the mean profile, which are also consistent with those shown in Fig. 3.8.

3.4.2 Differences in the outflow layer

Given the obvious differences in the upper-tropospheric warming, it is worthwhile to examine the characteristics of how the warm air is able to accumulate in developer versus the non-developers. Chapter 2 demonstrated that the accumulation of the upper-level warmth results from a storm-scale outflow developing beyond L_R, within which, the velocity field tends to adjust to the mass field, with significant reduction in energy dispersion by gravity waves. Further, high VWS in the warming layer inhibits the formation of the upper-level warming (Zhang and Zhu 2012), as the warming is "sheared apart".

To investigate the key differences in the outflow layer, Fig. 3.11 shows the 100 km × 100 km area-averaged L_R, 400-150 hPa layer-averaged divergence, and 400-150 hPa layer-averaged VWS for the same time period as Fig. 3.8. The upper-level warming seen for member 10 (Figs. 3.8 and 3.9) becomes a system-scale feature due to a significant reduction in L_R below 800 km, a potent divergent outflow extending beyond L_R, and low VWS in the warming layer (red lines, Figs. 3.11a-c). As the upper-tropospheric warming takes place, local static stability is reduced, causing L_R to shrink. As will be shown later, the large divergent outflow in member 10 results from the maintenance of deep convection near the AEW pouch center and its up-scale aggregation into an MCS. Unlike member 10, the non-developer (member 14) shows minimal reduction in L_R, weak divergent outflow, and a steady increase in 400-150 hPa layer VWS to above 18 m s^{-1} (blue lines, Figs. 3.11a-c). Given the combination of these characteristics, it is not surprising that significant warmth

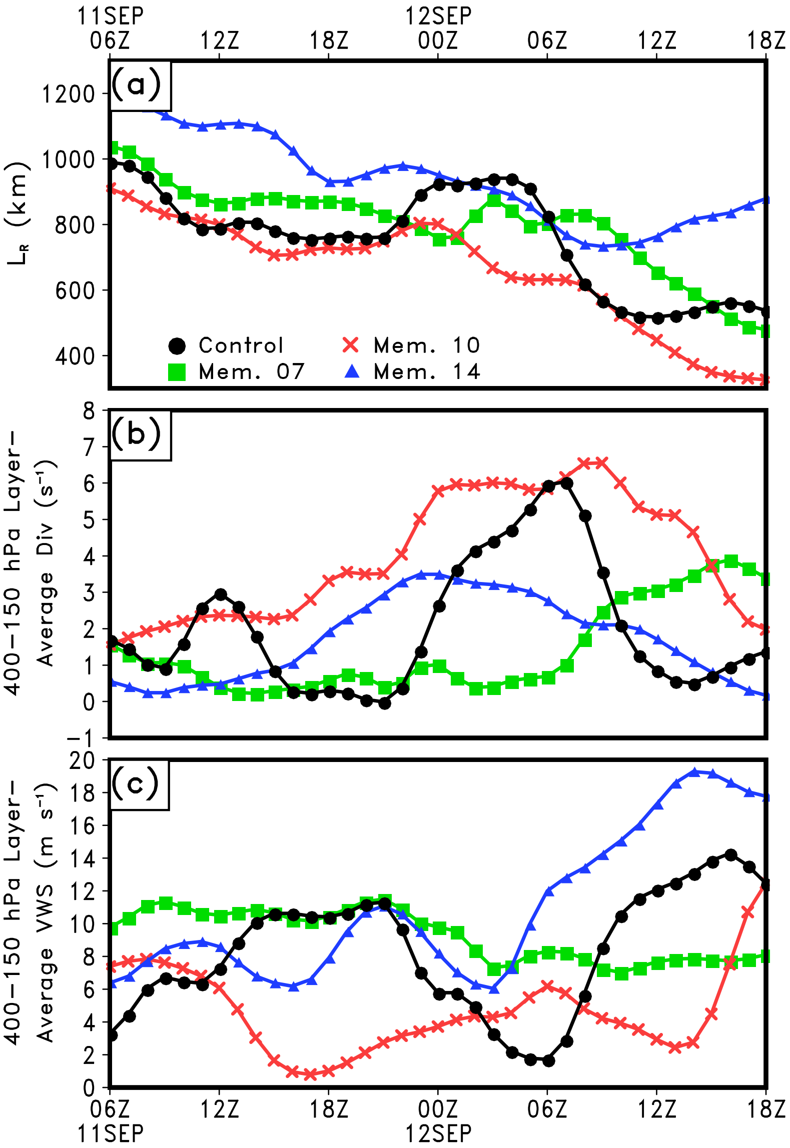

Figure 3.11: Time series (0600 UTC 11 to 1800 UTC 12 Sep) of the 100 km × 100 km area-averaged (a) Rossby radius of deformation ($L_R = NH/\eta$, where η is the 1000-400 hPa layer-averaged absolute vorticity, $N = \sqrt{\frac{g}{\bar{\theta}}\frac{d\theta}{dz}}$ is calculated using the area-averaged 1000 hPa potential temperature ($\bar{\theta}$), the vertical differential potential temperatures and heights between 150 and 1000 hPa ($\frac{d\theta}{dz}$), and g is the gravitational constant. H is calculated using $H = R\bar{T}/g$, where $\bar{T}$ is the average temperature between 1000 and 150 hPa, and R is the gas constant for dry air); (b) 400-150 hPa layer-averaged divergence (s^{-1}); and (c) 400-150 hPa layer-averaged VWS (m s^{-1}) from the selected 4 members using 3-km resolution domain data.

could not accumulate on the storm scale. It is very likely that the weak warming seen for member 14 in Fig. 3.8c diminished as a result of the large increase in the outflow layer VWS, in a fashion similar to the control. Thus, the system-scale warming is reliant on the outflow layer being cooperative with weak VWS. Otherwise, even if a storm-scale outflow beyond L_R is present, the warming will be "torn apart" by the VWS. An interesting topic for future work of ours will be *why* the VWS differences exist, as the results herein do not elucidate such differences.

Further elaborating on the upper-tropospheric warming in the outflow layer, Fig. 3.12 compares the area-averaged 400-150 hPa layer-averaged relative divergence and temperature between each ensemble member at 12/0000 and 12/0600. A clear positive correlation (with a correlation coefficient of 0.733) exists at 12/0000, with members having greater divergence in the 400-150 hPa layer and warmer area-averaged upper-tropospheric temperatures. A very similar pattern, though an opposite correlation, can be seen when comparing Fig. 3.12a with Fig. 3.10a, alluding to the interconnectedness of the parameters investigated. Most ensemble members have area-averaged divergence below 1.6×10^{-5} s^{-1} in conjunction with upper-tropospheric temperatures below -37°C. By 12/0600, a more definitive ensemble spread occurs as fast developers depict a more pronounced divergent outflow in addition to the warmer upper-tropospheric temperatures (Fig. 3.12b). The difference between slower and faster developing members can also be easily identified by the vertical and horizontal dashed lines in Fig. 3.12b, marking the intersection of -37°C upper-tropospheric temperatures and 2.3×10^{-5} s^{-1} divergence. Obviously this relationship is simply hydrostatic balance, though these relationships have not been alluded to in previous studies regarding the development of the TD-scale MSLP disturbance. These results support our initial findings that a prominent divergent outflow aids in the expansion of the upper-tropospheric warming over a meso-α-scale area as $\mathrm{L_R}$ shrinks due to reduced static stability in the upper troposphere.

3.4.3 Differences in convective initiation

The development of persistent deep convection can help precondition the tropospheric column with sufficient moisture, an important factor for the occurrence of TCG within an AEW (Hopsch et al. 2010). TCG has also been shown to have ties to deep convection and its area coverage by Sippel and Zhang (2008) through high tropospheric moisture content and CAPE. In addition, upper-level warming development (Figs. 3.8 and 3.9) relies on persistent deep convection and a storm-scale outflow within the AEW (chapter 2, Zhang and Zhu 2012). The latent heating in the upper troposphere due to deposition and freezing has been shown to be related to the intensification and aggregation of deep convection (or convective bursts, CBs through associated low-level vortical circulations) into an MCS along the low-level AEW critical latitude (see chapter 2). As the MCS becomes organized, the storm-scale outflow expands beyond the shrinking $\mathrm{L_R}$, enabling the accumulation of meso-α-scale warming in the upper troposphere. Fig. 3.13 shows the time series of surface-based convective inhibition (CIN), simulated composite radar reflectivity, 550-500 hPa layer-averaged relative humidity, and surface-based CAPE that are area-averaged around each members' respective storm center. In addition, Fig. 3.14

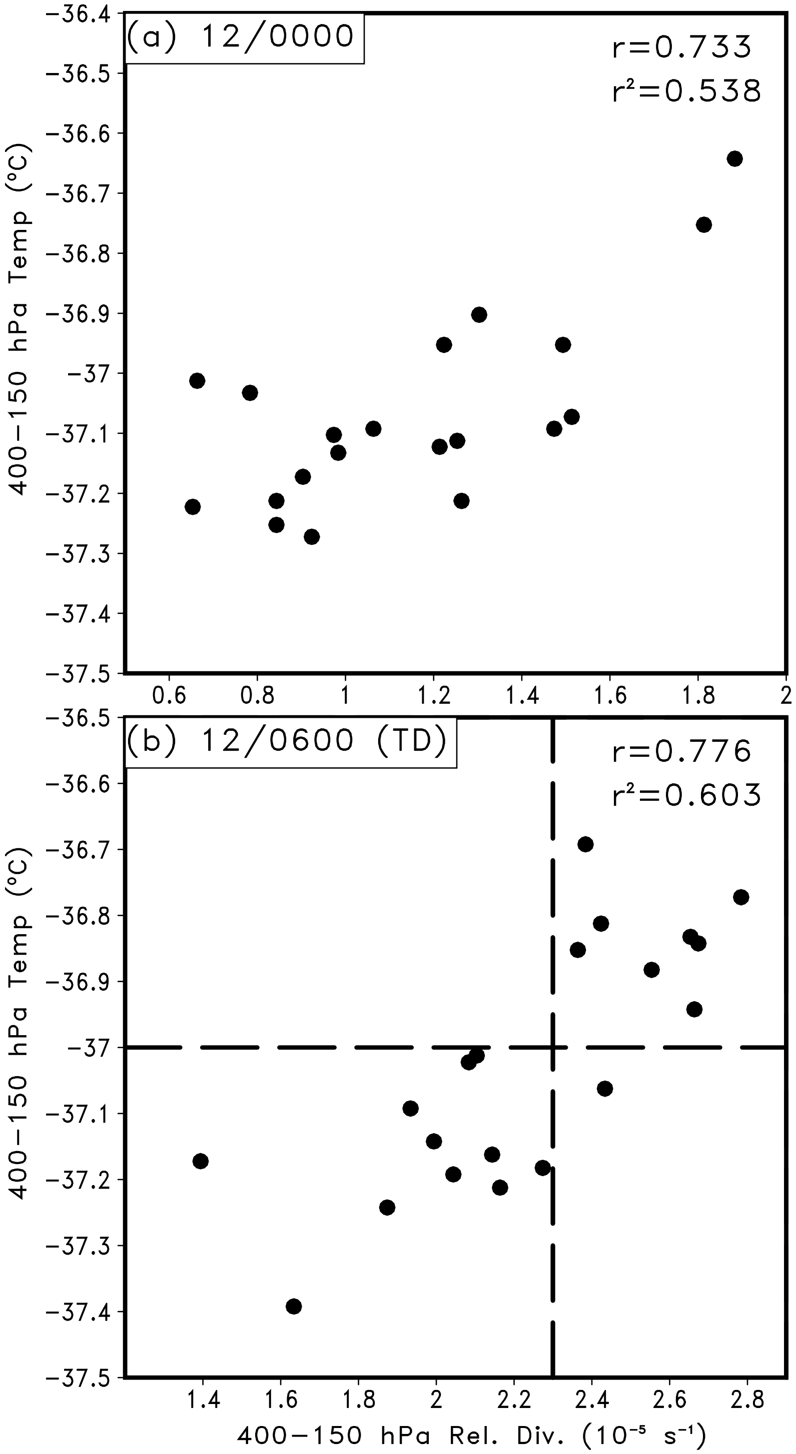

Figure 3.12: As in Fig. 3.10, except for 400-150 hPa layer-averaged relative divergence ($\times 10^{-5}$ s^{-1}; x-axis) and 400-150 hPa layer-averaged temperature (°C; y-axis). The vertical and horizontal dashed lines in (b) represent the schism between fast- and slow-developing ensemble members.

shows the spatial distribution of composite radar reflectivity and surface-based CIN. Further, Figs. 3.14q-t show the 200-hPa -52.5°C isotherm valid at 11/1800, the time at which member 10 first develops a meso-β-scale P_{MIN}.

The surface-based CIN (Fig. 3.13a) shows one distinct period of member differences between 10/1800 and 11/1200, as encompassed by the dashed lines. Before 10/1800, CIN values are agreed upon in all members, averaging around 10 J kg^{-1} (Fig. 3.13a) with no convection in the core region (Fig. 3.13b). CIN quickly increases in members 7 and 14 after 10/1800 (green and blue lines in Fig. 3.13a) reaching 55 and 45 J kg^{-1}, respectively, at 11/0600. In contrast, member 10 has a much slower increase in CIN values, reaching 25 J kg^{-1} at 11/0600, nearly half that of the other members. The development of CIN in all members takes place to the north and west of each member's AEW pouch center between 10/1800 and 11/0600 (Figs. 3.14a-l), reaching a maximum just before sunrise when the nocturnal inversion is the strongest (11/0600). Such a finding alludes to the possibility that radiational cooling is contributing to the enhanced CIN values. The CIN suppresses convective development between 11/0000 and 11/0900 in all ensemble members and the control, with average composite radar reflectivity returns below 15 dBz near the storm centers (Figs. 3.13b and 3.14).

After 11/0600, all members show a large reduction of CIN (Fig. 3.13a), with member 10 beginning to initiate more convection near the storm center (Fig. 3.14n). In general, the suppression of deep convection due to CIN during the 18-h period of 10/1800 and 11/1200 has a lasting impact on the spatial coverage of convection near the storm centers of all the members. At local noon (i.e., 11/1200), vertical

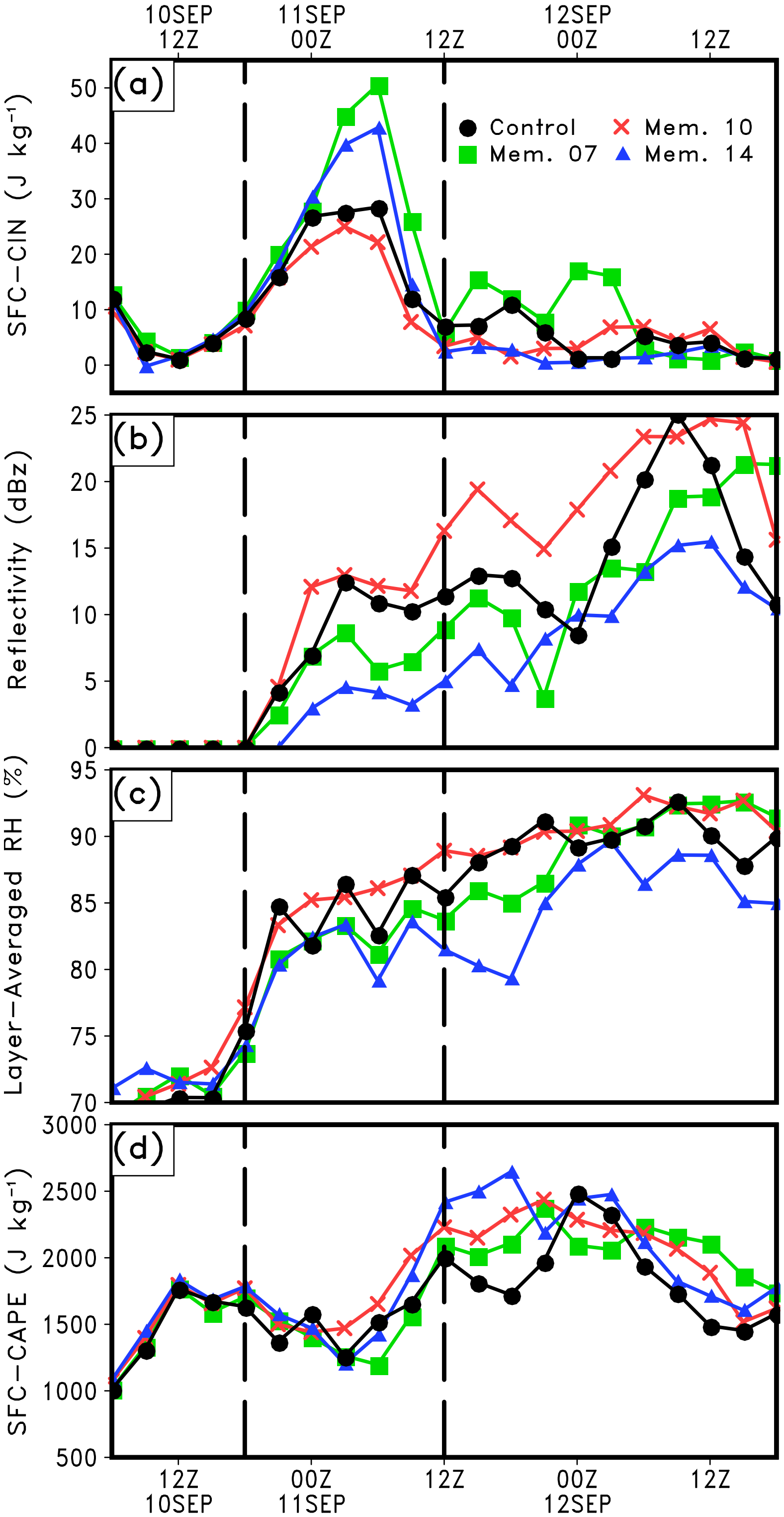
10SEP
12Z
11SEP
00Z
12Z
12SEP
00Z
12Z
(a)
SFC-CIN (J kg⁻¹)
50
40
30
20
10
0
● Control
🟩 Mem. 07
× Mem. 10
▲ Mem. 14
(b)
Reflectivity (dBz)
25
20
15
10
5
0
(c)
Layer-Averaged RH (%)
95
90
85
80
75
70
(d)
SFC-CAPE (J kg⁻¹)
3000
2500
2000
1500
1000
500
12Z
10SEP
00Z
11SEP
12Z
00Z
12SEP
12Z

Figure 3.13: Time series of (a) surface-based convective inhibition (CIN, J kg^{-1}), (b) simulated composite radar reflectivity (dBz), (c) 550-500 hPa layer-averaged relative humidity (%), and (d) surface-based convective available potential energy (CAPE, J kg^{-1}) that are averaged over an area of 200 km × 200 km around the storm center from ensemble members 7 (green, best), 10 (red, strongest), and 14 (blue, weakest) and the control simulation (black) valid from 0600 UTC 10 to 1800 UTC 12 Sep from the 9-km resolution domain. The vertical dashed lines encompass the period where convective development is limited in all members.

mixing of the PBL tends to remove any possible nocturnal inversion. However, the larger the CIN (e.g., inversion), the longer it takes to erode, and thus the members with greater CIN (members 7 and 14) show the suppression of new convective development (Figs. 3.14m,o,q,s). Member 10 with its weaker CIN near the AEW pouch center reinvigorates the MCS off the coastline between 11/1200 and 11/1800 (Figs. 3.14n,r), in a fashion similar to the control (Figs. 3.14p,t). Delayed convective initiation persists in the non-developer (member 14), with average composite reflectivity returns well below member 10 from 11/1800 to the end of the simulation (Fig. 3.13b). The development of the meso-β-scale P_{MIN} in member 10 is found where the strongest reflectivity returns over water occur, in a region characterized by temperatures greater than -52.5°C at 200 hPa (circled area in Fig. 3.14r). Such a finding is consistent with the results discussed previously with respect to the outflow layer (see red lines, Figs. 3.11a-c).

The mid-tropospheric moisture content also exhibits differences between the members, as shown by the layer-averaged 550-500 hPa relative humidity (hereafter RH; Fig. 3.13c). As convection develops between 10/1800 and 11/000 (Figs. 3.13b

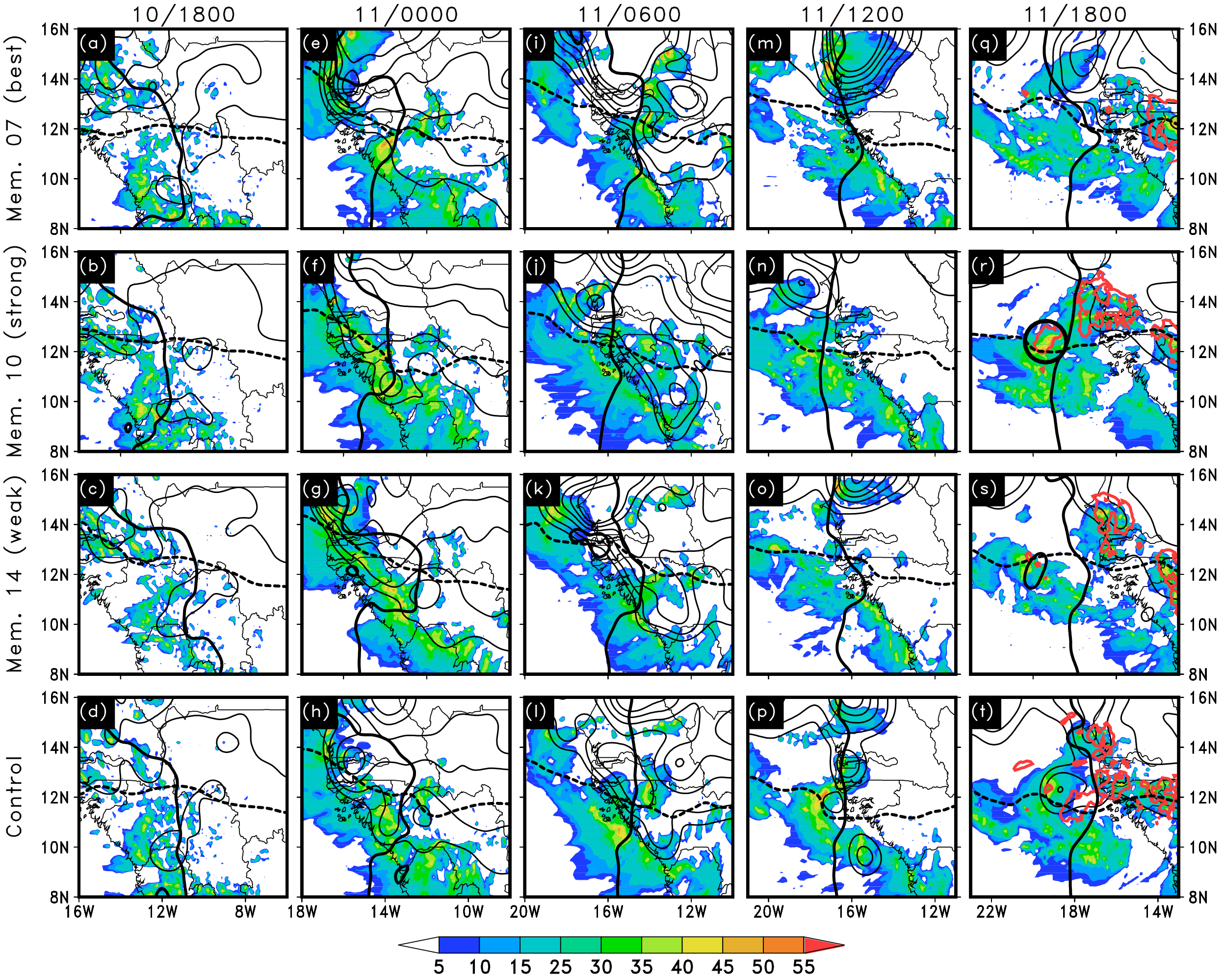

Figure 3.14: Comparison of the composite radar reflectivity (shaded, dBz) and surface-based CIN (contoured at 10, 20, 40, 60, 80, and 100 J kg^{-1}) from ensemble members 7 (first row), 10 (second row), 14 (third row) and the control simulation (fourth row) valid at 1800 UTC 10, 0000 UTC, 0600 UTC, 1200 UTC, and 1800 UTC 11 Sep, respectively. The 600-hPa AEW trough axis and critical latitude are shown with the thick solid and dashed lines, respectively. The -52.5°C isotherm at 200 hPa is contoured bold red at 1800 UTC 11 Sept in (q-t) to demonstrate the relationship between the warming and deep convection. The circle in (r) encompasses the location of the first closed MSLP contour from member 10. Data from the 9-km resolution domains are used.

and 3.14), all members show an increase in layer-averaged RH values with member 10 having the largest increase of nearly 10%. A slow (but variable) increase in the layer-averaged RH occurs between 11/0000 and 11/1200 as new convection struggles to develop (Figs. 3.13a,c). The differences in RH between the members become most notable between 11/1200 and 12/0000, as convective development increases and CIN is reduced. Member 10 shows a consistent increase in midlevel RH to above 90% by 12/0000, while members 7 and 14 show a delayed response in the midlevel moistening directly after 11/1200. This delay in development until roughly 11/1800 can be attributed to having to overcome larger CIN in the previous 12-h period (Figs. 3.13 and 3.14). After 12/0000, every member except for member 14 has sufficient midlevel moisture with RH values nearing 90% (Fig. 3.13c). Such a difference is readily explained by the lack of convective development near the storm center in member 14, as seen in Figs. 3.14b and 3.13.

Surprisingly, surface-based CAPE exhibits little differences between the developers and non-developers. This result does not agree with that of Komaromi (2012) who found that non-developing storms had substantially larger CAPE than developing storms when calculated from composite soundings during the PREDICT campaign. Our findings also somewhat disagree with Sippel and Zhang (2008), who noted CAPE as an important initial condition for the early 6-h to 12-h period of integration in developers, in contrast to the findings of Komaromi (2012). We state that the results disagree “somewhat” with Sippel and Zhang (2008) since they do explicitly mention that (i) their results are specific to the storm investigated; (ii) their results do not imply that CAPE is directly correlated to occurrence of TCG;

and (iii) they believe it is possible for CAPE to speed up TCG, given a favorable large-scale environment. Even so, CAPE is only a measure of energy *available* to the parcel and may be useful after overcoming CIN. Thus, we believe that CAPE differences are secondary to the ability to generate and sustain deep convection, which relies on reduced CIN and development along the low-level AEW critical latitude near the AEW pouch center (Dunkerton et al. 2009). Overall though, the general idea from Sippel and Zhang (2008) that convective development and coverage are important for TCG is agreed upon with our findings. This overarching characteristic of developing disturbances is also supported by Hopsch et al. (2010).

Our results indicate that the predisposition of larger CIN in members 7 and 14 suppresses convective development and thus the vertical moisture transport needed to precondition the atmosphere prior TCG. This result is consistent with Hopsch et al. (2010), who notes that non-developing AEWs are more likely to have drier air in the middle- and upper-levels. The results allude to the need for fast-developing waves (Hopsch et al. 2010) to also have lower CIN in close proximity to their pouch center, so that convection can develop and persistently moisten the midtroposphere. These CIN values could possibly tie to the time of day for the coastline passage, which if at night, would enhance the CIN due to the development of a nocturnal inversion. The diurnal nature of convection has been shown to be linked to TCG by Ventrice et al. (2012a) and thus, similar variations in CIN could be the limiting factor of convective development. Overall, the strongest developer (member 10) had less CIN to overcome early in the simulation, allowing for faster development of a persistent MCS. This in turn preconditions the middle and upper troposphere with moisture and also allows for the faster development and expansion of the storm-scale outflow and thus, upper-tropospheric warming.

3.4.4 Summary and discussion

The preceding investigated the TCG of Hurricane Julia (2010) using a suite of WRF-LETKF ensemble simulations and the differences between them. It is evident from the 20 ensemble simulations that the TCG of simulated Julia is highly predictable with 18 out of 20 members having $\mathrm{P_{MIN}}$ deeper than the NHC estimated 1007 hPa at 12/0600. This result indicates that the NHC estimated storm could have been stronger by 2-3 hPa at this time, though this difference is within the range of acceptable error for intensity estimates of early-stage storms. We focused on two important factors for TCG: convective initiation and upper-level warming. Both of these are strongly tied together since persistent deep convection and its maturation along the low-level AEW critical latitude during TCG allows for (i) the development of the storm-scale outflow; (ii) a reduction of $\mathrm{L_R}$; and (iii) the depositional heating of the upper troposphere.

It is shown that the strongest member has the most prominent upper-level warming over a larger spatial area prior to and at TCG, which induces similar-sized meso-α MSLP falls and the development of a meso-β surface low into a TD. In particular, the meso-β-scale surface low is consistently located with the warmest temperatures in the upper troposphere, demonstrating that TCG is resultant of locally-induced surface pressure falls from the warming aloft. The opposite is true for the weakest member. The warming of the upper troposphere has been proposed to occur by the depositional growth of ice particles and freezing, in addition to compensating subsidence once a mature MCS is present. This notion is supported by the findings that the strongest member has cloud ice content nearly double that of weaker members.

Initiation of deep convection is found to be tied to the magnitude CIN earlier in the simulations. The member with weaker CIN early in the simulation shows the faster development of convection after coastal passage, and has the faster-developing TD. This is consistent with previous work such that fast developing waves have higher midtropospheric moisture content and stronger convection during coastal passage. Supplementing this idea, the faster development and aggregation of deep convection over the ocean allows for the upper-level warming to intensify and expand faster with time, inducing MSLP falls earlier in comparison to the other members. Thus, we believe that fast-developing AEWs might also have an appreciable difference in the magnitude of CIN during coastal passage. No appreciable differences are found to take place between developing and non-developing members with respect to surface-based CAPE. This result, however, is believed to be secondary to the importance of weak CIN values prior to TCG, since parcels cannot use CAPE before CIN is overcome. While this somewhat contradicts the results of previous work, the notion of persistent deep convection and higher tropospheric moisture content for developing disturbances agrees with the results found previously. This lends us to believe that convective initiation is an important factor for TCG, and it remains to be seen whether CIN, CAPE or both have a lasting impact on the presence of deep convection prior to and during TCG.

In conclusion, we may state that the fundamental ensemble member differences for the TCG of Julia involve convective initiation near the core region and the development of storm-scale upper-tropospheric warming. Given that the synoptic scale environment was favorable for TCG, the slight differences in the initiation and persistence of storm-scale deep convection could be responsible for the occurrence of TCG. This might or might not be true for other TCG cases, however, as each case includes a multitude of factors that must come together for TCG to occur.

3.5 Ensemble sensitivity analyses

3.5.1 Methodology

While the previous subsections provided meaningful results from utilizing only 4 simulations, the following focuses on expanding the investigation beyond a handful of ensemble members. To this end, our approach herein investigates the uncertainty associated with the TCG of Julia by utilizing the whole complement of ensemble members (i.e., 20 members). Using the full complement of ensemble members, sensitivity analyses are conducted.

The ensemble sensitivity analyses performed herein employ EOFs and related PCs as forecast metrics, following those used by Chang et al. (2013) and Zheng et al. (2013). Typically, EOFs are created in temporal and spatial dimensions, with the PCs representing the time series of the EOF pattern. Alternatively, we calculate EOFs using the ensemble dimension in lieu of the time dimension. Essentially, anywhere the time dimension is used is replaced with the ensemble dimension in the EOF calculation, ranging from $1 \ldots M$, where $M = 20$ (i.e., the number of ensemble members). Thus, the 20 values of a PC (hereafter referred to as "PC values") represent how strongly a particular ensemble member projects on to the particular phase of the related spatial EOF pattern. We generate EOFs at two important stages in the evolution of Julia: (i) pre-TD: 11/1800, and 12/0000; and (ii) TD: 12/0600. These times are chosen based on the emergence of MSLP disturbances in some faster developing members in addition to being times when the ensemble spread nears or exceeds 1 hPa (Fig. 3.5a). These times correspond to 42, 48, and 54 h integration times from the ensemble forecasts. We create the EOFs over a 10° longitude × 6° latitude domain encapsulating the storm centers of each ensemble member at each respective time using simulation data from the 27-km resolution domain. The 27-km resolution domain is used to ensure that a coherent ensemble difference signal can be identified by the EOFs. Higher resolution domains (e.g., 3 km) would have too much variance in the system such that intensity and position disagreements between the ensemble members would not be identified by the EOFs, or the EOFs would explain substantially less variance. The sensitivity analyses will focus on the PCs from one of the two leading EOF patterns, as these explain the largest portion of the total variance of the respective parameter, while the third and beyond EOFs explain substantially less total variance (typically less than 10% for the respective parameter).

While assessing these EOF patterns, care needs to be taken in understanding their physical significance. The EOF spatial pattern carries the same unit as the forecast variable (e.g., hPa for MSLP) with the amplitude representing the amount of the ensemble sample standard deviation explained by the EOF. The sign of the pattern *does not* matter, but the spatial characteristics of the pattern do have physical significance. That is, the spatial patterns of the EOFs can represent intensity and position differences of a cyclone (Chang et al. 2013; Gombos et al. 2012; Zheng et al. 2013), which for our use, will be the intensity and position ensemble differences of the pre-TD and TD phases of Julia. Since TCG denotes the transition of a non-developing tropical disturbance into a developing one, the PC of the EOF pattern representing an intensity disagreement is used preferentially in the sensitivity analyses.

As previously mentioned, the PC of either the leading EOF pattern (EOF 1) or second EOF pattern (EOF 2) will act as a forecast metric for our sensitivities. Following Chang et al. (2013) and Zheng et al. (2013), ensemble sensitivity is defined as:

$$Sensitivity = \frac{Cov(x,p)}{s_x s_p} \tag{3.1}$$

where p represents the PC, x is a meteorological parameter, and $Cov(x,p)$ is the covariance, defined by:

$$Cov(x,p) = \frac{1}{M-1}\sum_{i=1}^{M}[(x_i - \bar{x})(p_i - \bar{p})]$$

where $(x_i - \bar{x})$ and $(p_i - \bar{p})$ represent departures from the ensemble mean of x and p, respectively. The sample standard deviations, s_x and s_p, are defined as:

$$s = \left[\frac{1}{M-1}\sum_{i=1}^{M}(x_i - \bar{x})^2\right]^{1/2}$$

with the range $1 \ldots M$ representing the ensemble dimension, where $M = 20$. The calculation of Eq. (3.1) is generated at every grid point over a 20° longitude × 15° latitude domain surrounding the ensemble cluster, identifying the PC's sensitivity to various meteorological parameters. It is evident that Eq. (3.1) is simply the Pearson's correlation between the PC and a specific meteorological parameter at every grid point. Caution must be taken when using such a parameter, since non-linearity between variables is not captured by the correlation. We select meteorological parameters for Eq. (3.1) that have already been demonstrated to have physical significance with the parameter whose ensemble disagreements were deconstructed via the EOF process. By ensuring the existence of this physical significance, the sensitivities calculated also have physical meaning, even if the relationship is not strictly linear. In this regard, Gombos et al. (2012) explicitly mentioned the dilemma for using model sensitivities to make dynamical inferences about the real atmosphere. Such inferences can only be made when the ensembles realistically represent the true atmospheric state. Since we already demonstrated that the ensemble forecasts represent reasonable atmospheric states, dynamical inferences can be made using ensemble sensitivities. Furthermore, keeping consistency with our previous investigations, we preferentially examine MSLP, upper-tropospheric warming, and deep convection to gain a further understanding of their interconnectedness during the TCG of Julia.

3.5.2 Dominant ensemble variances during the pre-TD stage

Twelve and six hours respective before the NHC declared Julia a TD, noteworthy variability (or spread) in several meteorological parameters exists between the ensemble members. This spread is especially pronounced in P_{MIN} estimates, with ensemble sample standard deviation of near 1 hPa at 11/1800 and exceeding 1 hPa at 12/0000. While seemingly small in comparison to ensemble forecasts spreads for mature TCs or midlatitude disturbances, a spread of 1 hPa could mean the difference between a TD and a non-developing tropical disturbance. Thus, it is desirable for us to characterize the MSLP spread into patterns in order to see what "kind" of disagreements exist between the ensemble members. These disagreements may also be isolated in other meteorological parameters, such as upper-tropospheric temperature anomalies and radar reflectivity. Using these isolated patterns of ensemble spread, links between the parameters can be implied, both subjectively and statistically (e.g., through ensemble sensitivity analyses). Furthermore, the evolution of the parametric ensemble spread and associated EOF patterns demonstrate how the pre-TD Julia evolves in the ensemble members, and what processes might be responsible for the changes in the patterns of disagreements. In the following subsections, we show the ensemble spreads of MSLP, low-level absolute vorticity, upper-level temperature anomalies, and deep convection, in addition to ensemble sensitivity analyses.

3.5.2.1 Variability in MSLP

Figs. 3.15 and 3.16 show the ensemble spread, ensemble mean, and the two leading EOFs of MSLP that are identified as the dominant spatial patterns in the ensemble spread at 11/1800 and 12/0000, respectively. We see three regions of heightened spread with respect to the ensemble mean field at 11/1800. The spread associated with faster developing ensemble members (or fast developers for short) is marked by "M_1", and symbolizes the creation of pre-TD MSLP disturbances in some members as demonstrated by the cluster of P_{MIN} centers (Fig. 3.15a). Unlike 11/1800, a bull's-eye of enhanced spread exists at 12/0000, with the sample standard deviation exceeding 1 hPa ("M_1", Fig. 3.16a). The overall structure of the ensemble sample standard deviation evolves into a monopole pattern by 12/0000, but with enhanced spread extending eastward back toward the west African coastline ("M_2") in close proximity to M_2 from 11/1800. This eastward spread is supported by the ensemble mean MSLP, which depicts an elongated closed 1008-hPa isobar extending from the bull's-eye center back to the coastline (Fig. 3.16a).

The largest mode in the ensemble spread at 11/1800 is depicted by the leading EOF (EOF 1), which explains 29.4% of the variance with a weak monopole pattern centered near M_1 (Fig. 3.15b). This monopole pattern is a characteristic of an intensity disagreement between the ensemble members as demonstrated in previous studies (Chang et al. 2013; Zheng et al. 2013). Thus, the pattern of most disagreement between ensemble members at 11/1800 is the intensity of the pre-TD Julia. Since we are looking at the "negative" phase of EOF 1, which happens to

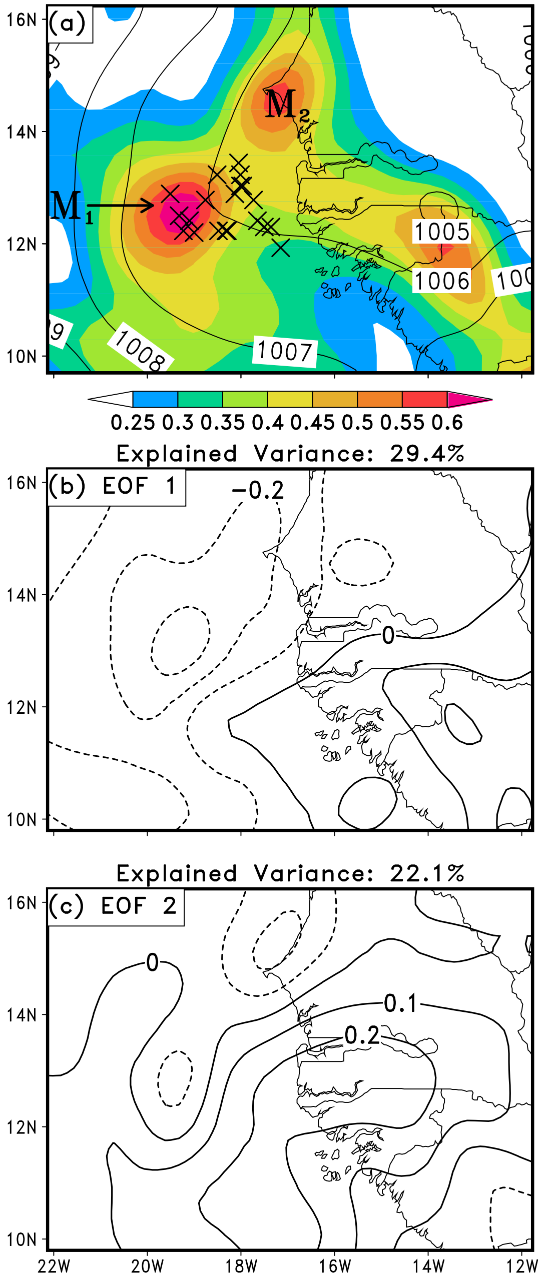

Figure 3.15: Spatial distributions, valid at 1800 UTC 11 Sep, of (a) ensemble MSLP standard deviation (shaded, hPa) and ensemble mean MSLP (contoured at intervals of 1 hPa); (b) the most reoccurring spatial pattern of MSLP anomalies (i.e., the leading EOF; EOF 1) contoured at intervals of 0.1 hPa; and (c) the second most reoccurring spatial pattern of MSLP anomalies (EOF 2) contoured at intervals of 0.1 hPa. The explained variance for EOF 1 (b), and EOF 2 (c) are 29.4% and 22.1%, respectively. "M_1" and "M_2" in (a) represent a maximum in the MSLP ensemble spread associated with the faster developing members and coastal variance, respectively. Each ensemble member's P_{MIN} center at 1800 UTC 11 Sep is marked by an ×.

represent negative MSLP anomalies, this pattern alludes to the presence of ensemble members with stronger pre-TD disturbances at 11/1800. This intensity disagreement becomes increasingly evident at 12/0000 as the leading EOF explains 47.3% of the ensemble spread with a monopole pattern clearly situated within the ensemble cluster and M_1 (Fig. 3.16b). The leading EOFs from both times are supported by findings previously, which depicted intensity differences when assessing the time series of ensemble P_{MIN} disturbances (Fig. 3.5a). Another common pattern shown previously by Chang et al. (2013), and Zheng et al. (2013) is depicted in the second EOF at 12/0000 (Fig. 3.16c). This dipole pattern is associated with positional disagreements between the ensemble members, which is consistent with the enhanced spread eastward from the bull's-eye in Fig. 3.16a.

It is evident from the EOFs at both times that the most dominant difference between ensemble members is related to the intensity of the pre-TD Julia (Figs. 3.15b and 3.16b). As ensemble solutions evolve in time and some members develop pre-TD disturbances in terms of P_{MIN}, the second leading EOF evolves into the positional ensemble differences for the P_{MIN} location (Fig. 3.16c). Recall that the sign of the EOF pattern is not relevant. Even though EOF 1 represents a stronger storm with negative MSLP anomalies at both times, its sign can be changed to represent the other phase, a weaker storm with positive MSLP anomalies. Moreover, it is worth noting that EOFs can contain more than one pattern (e.g., monopole, dipole, etc.), and thus, care needs to be taken to elucidate what possible pattern(s) exist in any given EOF. This being said, since we are dealing with TCG the sign of intensity EOFs will always represent the stronger storm phase (e.g., negative MSLP

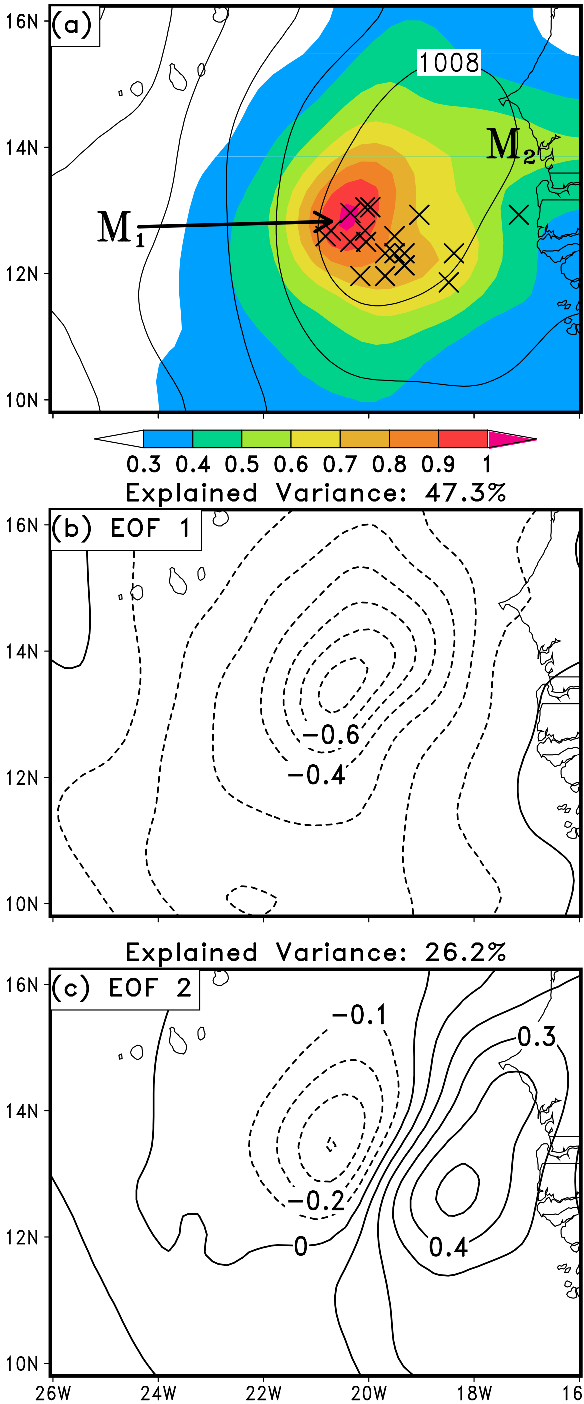

Figure 3.16: As in Fig. 3.15, but valid for 0000 UTC 12 Sep.

anomalies), as we are interested in seeing a stronger TD Julia.

3.5.2.2 Variability in 925-hPa absolute vorticity

Since the growth of the LLV is an important part of TCG (Hendricks et al. 2004; Montgomery et al. 2006), Fig. 3.17 shows the 925-hPa absolute vorticity ensemble spread, ensemble mean and related EOF patterns at 12/0000. At this time, it is expected that a large variability exists between the members, since the process by which the LLV forms is through the merging of numerous mesovortices and enhancement by deep convection. The control simulated TCG of Julia depicted that two main mesovortices merge just prior to and after the TCG time of 12/0600 (see chapter 2). Thus, it is expected that significant ensemble member differences exist for the location and strength of the main mesovortices that become the LLV in each member at 12/0000. These disagreements are in turn expected to reduce the variance explained for each of the 925-hPa absolute vorticity ensemble spread EOF patterns.

Similar to the MSLP ensemble spreads at 12/0000, the 925-hPa absolute vorticity spread has two centers of heightened variance, one located over water, the other along on the coastline, marked by "V_1" and "V_2", respectively (Fig. 3.17a). The ensemble mean 925-hPa positive absolute vorticity center exceeds 9×10^{-5} s^{-1}, representing an elongated, weak vortex centered near V_1. Given the weakness of the ensemble mean vortex with an ensemble spread exceeding 6×10^{-5} s^{-1} near the ensemble mean center, it is believed that the mean is averaging through many ensemble

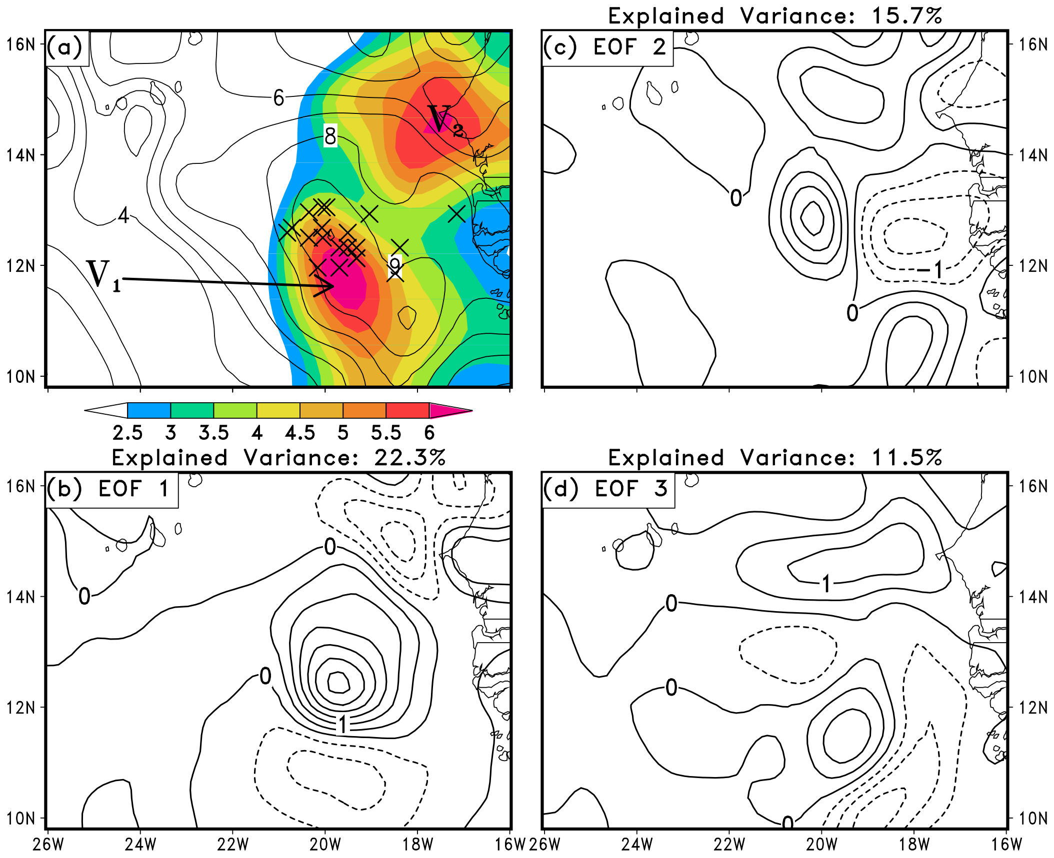

Figure 3.17: As in Fig. 3.15, but valid for 925-hPa absolute vorticity anomalies ($\times 10^{-5}$ s^{-1}) at 0000 UTC 12 Sep including an additional EOF, EOF 3 (d), which explains 11.5% of the total variance.

member mesovortices near V_1, reducing the positive absolute vorticity magnitude in some areas, while increasing it in the others. The location of the spread near V_2 is similar to that of M_2 in Fig. 3.16a, though the pattern of vorticity variance is much more pronounced in comparison to its MSLP counterpart.

The leading EOF pattern only explains 22.3% of the variance, representing the low-level vorticity ensemble differences associated near V_1. Comparing the leading EOFs of MSLP and 925-hPa absolute vorticity anomalies (cf. Figs. 3.16b and

3.17b), the EOFs are nearly collocated with each other, though the MSLP variance is slightly more westward than the vorticity field. As with EOF 2 of MSLP, EOF 2 of the low-level vorticity field represents a west-east dipole, demonstrating positional disagreements with the developing LLV. Since the first two EOFs explain only 38% of the variance, the third EOF is examined for any meaningful patterns. While much less clear than the leading two EOFs, EOF 3 does hint at intensity uncertainty centered on V_2 and complements the west-east elongated variance exhibited of MSLP (cf. Figs. 3.17d and 3.16a).

3.5.2.3 Variability in upper-tropospheric thermal anomalies

Complementing the disagreements in MSLP and low-level vorticity, similar patterns of ensemble member differences exist for the 400-150 hPa layer-averaged temperature anomalies shown in Figs. 3.18 and 3.19. At 11/1800, three maximum in the upper-tropospheric ensemble spread exist with the spread associated with the fast developers marked by "U_1" (Fig. 3.18a). The pattern seen in the ensemble spread at 11/1800 has similar characteristics to those of the MSLP ensemble spread, alluding to the two parameters' variability being linked (cf. Figs. 3.15a and 3.18a). These three centers of enhanced upper-tropospheric temperature variance morph into a pattern with two maximums in the ensemble spread at 12/0000, one over water with a magnitude exceeding 0.45°C ("U_1", Fig. 3.19a), and the other a slightly weaker maximum near the west African coast with a magnitude of near 0.4°C ("U_2"). As with 11/1800, these two maximums at 12/0000 closely resemble the locations of the two maximum variances in MSLP and low-level vorticity (cf. Figs. 3.16a, 3.17a, and 3.19a), further alluding to some interconnectedness of the parameters. The ensemble spread center at U_1 is collocated with an ensemble mean warm region with magnitude greater than -41.4°C, while a meso-α area of warming in excess of -41.8°C encompasses both ensemble spread centers (Fig. 3.19a).

The first EOF pattern of 400-150 hPa temperature anomalies at 11/1800 represents positive temperature anomalies associated the heightened variance near U_1 (Fig. 3.18b). This pattern explains 28.4% of the variance with a north-south elongated monopole pattern. The second EOF represents an unbalanced dipole in the north-south direction (Fig. 3.18c) and explains slightly less variance than EOF 1 but with smaller amplitude compared to the leading EOF (e.g., 0.2°C versus 0.15°C). Most importantly, the leading EOF evolves into a monopole representing positive upper-tropospheric temperature anomalies centered with the enhanced ensemble spread near U_1 at 12/0000 (Fig. 3.19b). Unlike its counterpart at 11/1800, EOF 2 at 12/0000 represents positive temperature anomalies along the coastline, consistent with the ensemble spread centered near U_2 (cf. Figs. 3.16c, 3.17d, and 3.19c). The enhanced variance associated with EOF 2 can be explained partially by disagreements in deep convection shown in the next subsection.

3.5.2.4 Variability in convection anomalies

Previous studies have mentioned the important role of persistent deep convection in TCG through preconditioning the midtroposphere with moisture and its role

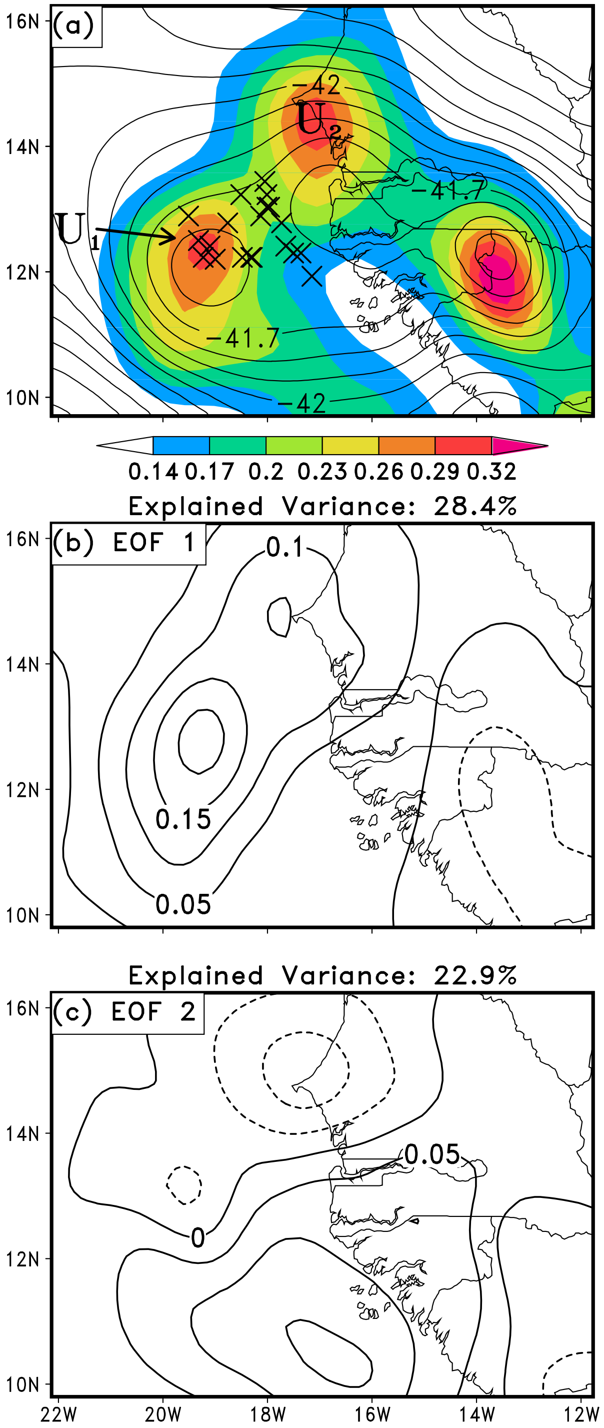

Figure 3.18: As in Fig. 3.15, but valid for 400-150 hPa layer-averaged temperature anomalies (°C) at 1800 UTC 11 Sep.

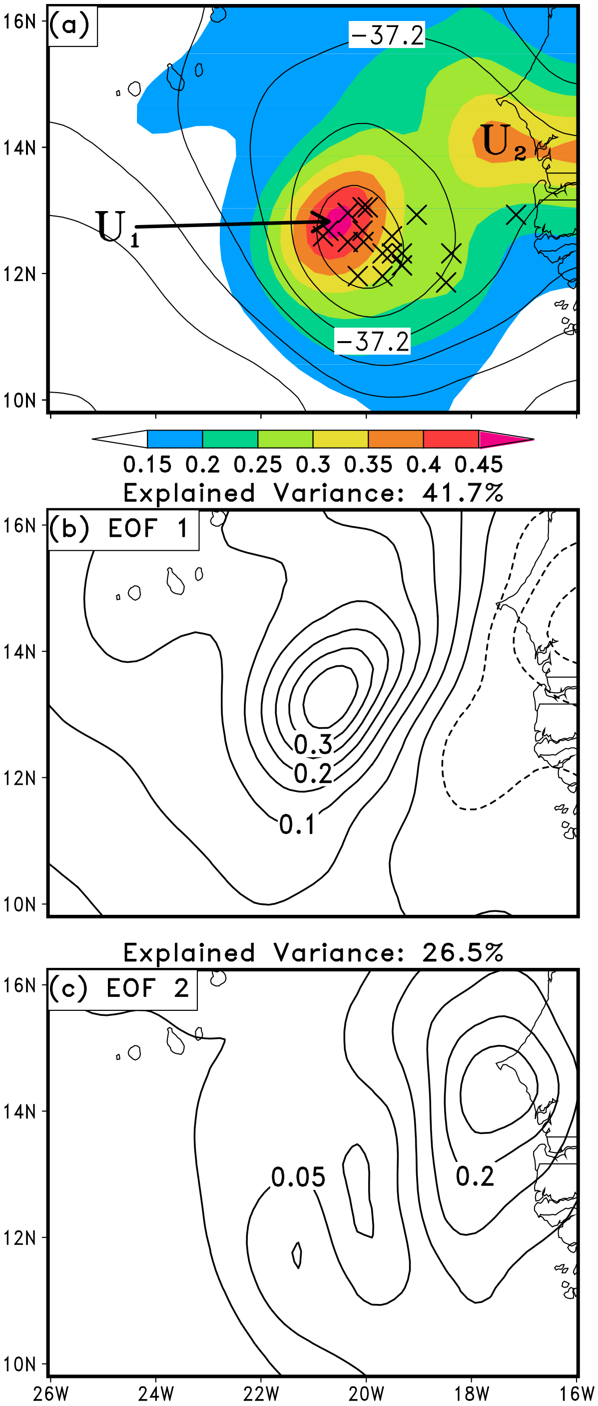

Figure 3.19: As in Fig. 3.15, but for 400-150 hPa layer-averaged temperature anomalies (°C) valid at 0000 UTC 12 Sep.

in upper-tropospheric warming (Dunkerton et al. 2009; Hopsch et al. 2010). Thus, it is desirable to evaluate the general convective structure disagreements in the hours prior to TCG. One should keep in mind that substantial variances appear in the location, magnitude, and extent of deep convection during TCG when ensemble member differences are assessed. In this regard, we previously have demonstrated the large differences in deep convection between developers and non-developers from the ensemble. As a result, dominant patterns and modes of variability could be much "noisier" than other parameters, such as MSLP.

At 12/0000, the ensemble spread of composite radar reflectivity exceeds 7 dBZ for an area larger than that encompassed by the ensemble mean composite radar reflectivity, signifying large disagreements between ensemble members for the placement and intensity of convection associated with the pre-TD disturbance (Fig. 3.20a). Even with the large variability, the ensemble mean depicts a weak MCS with reflectivity returns exceeding 25 dBZ centered to the south of the P_{MIN} cluster. Interestingly, the P_{MIN} cluster is closely collocated with ensemble spread exceeding 14 dBZ, hinting at ensemble disagreements with convective development near the storm center's of each member.

Decomposing the ensemble variance reveals two main EOF patterns, each explaining 33.8% and 18.7% of the total variance, respectively (Figs. 3.20b,c). The leading EOF represents a dipole with positive reflectivity anomalies centered to the northeast of the P_{MIN} cluster and ensemble mean composite radar reflectivity. Such a pattern alludes to the presence of enhanced (or decreased) convection to the north of the ensemble member centers at 12/0000 in addition to positional

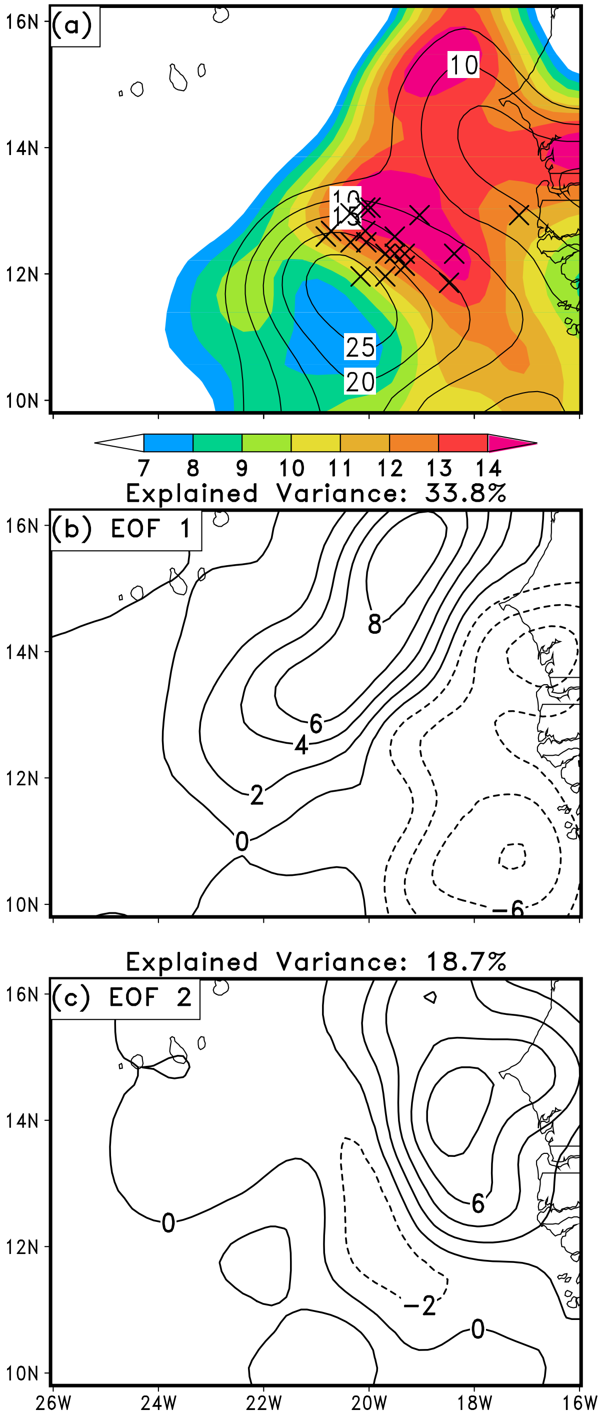

Figure 3.20: As in Fig 3.15, except for composite radar reflectivity anomalies (dBZ) valid at 0000 UTC 12 Sep.

uncertainties given the location of the gradient of the ensemble mean reflectivity in relation to the explained variance. The second EOF, however, with its positive composite reflectivity returns over the coastline, closely mimics the location of the second EOF of upper-tropospheric temperature spread (cf. Figs. 3.19c and 3.20c), as well as MSLP and low-level positive absolute vorticity (cf. Figs. 3.16c, 3.17d, and 3.20c).

3.5.3 Ensemble sensitivity analyses during the pre-TD stage

Given the presence of ensemble disparity in MSLP during pre-TD Julia's evolution, it is desirable to examine which parameter(s) these disagreements are sensitive to. Previously we demonstrated the importance of upper-tropospheric warming for meso-α-scale MSLP falls during the TCG of Julia. We have alluded to the importance of deep convection and coherent storm-scale outflow for the development of upper-level warming. To supplement these findings, an ensemble sensitivity analysis with Eq. (3.1) is used below to identify the mechanisms responsible for the patterns of differences in MSLP and upper-tropospheric temperature anomalies. Of particular interest to this study is the transition from storm-scale MSLP falls induced by upper-tropospheric thermodynamic changes to storm-scale MSLP falls induced by the WISHE. We separate the former method from the latter since the upper-tropospheric warming during TCG typically results from latent heating and not as a response due to balanced flow through thermal wind balance. It is obvious that TCG is itself a process characterized by imbalance, as it is merely a transition state.

Thus, while WISHE helps a balanced TC intensify, hydrostatically induced MSLP falls are necessary for TCG to occur. The upper-level warming is complemented by the development of a storm-scale outflow beyond the Rossby radius of deformation that traps the warming near the storm center. Finally, we investigate if there is any meaningful correlation between upper-level warming and deep convection.

3.5.3.1 MSLP 12/0000 EOF 1 Sensitivity

Since we are concerned with intensity differences in the forecasts of pre-TD Julia, the PC of EOF 1 of the MSLP variance (Fig. 3.16b) is used as the forecast metric in Eq. (3.1), while the 400-150 hPa layer-averaged temperature anomalies and surface latent heat flux anomalies are employed as the meteorological parameter ("x") to assess the sensitivity of EOF 1 to upper-tropospheric warming and WISHE, respectively. The sensitivity to both parameters is traced back to 11/1200 at 6 h intervals. Given the similarities of the MSLP and low-level vorticity EOF patterns, we decide to choose the MSLP EOFs for sensitivity analyses given our previous research predominately focusing on the MSLP disturbance. Further, we have shown the formation of a coherent MSLP disturbance on the meso-α scale prior to the existence of a coherent LLV, and obviously, lower MSLPs enhances PBL convergence which can enable subsequent growth of the LLV.

As expected, a large positive sensitivity exists between the PC and upper-tropospheric temperature anomalies (Fig. 3.21a), exceeding 0.6 for the Pearson's correlation. That is, to reproduce the negative MSLP anomalies shown in EOF 1

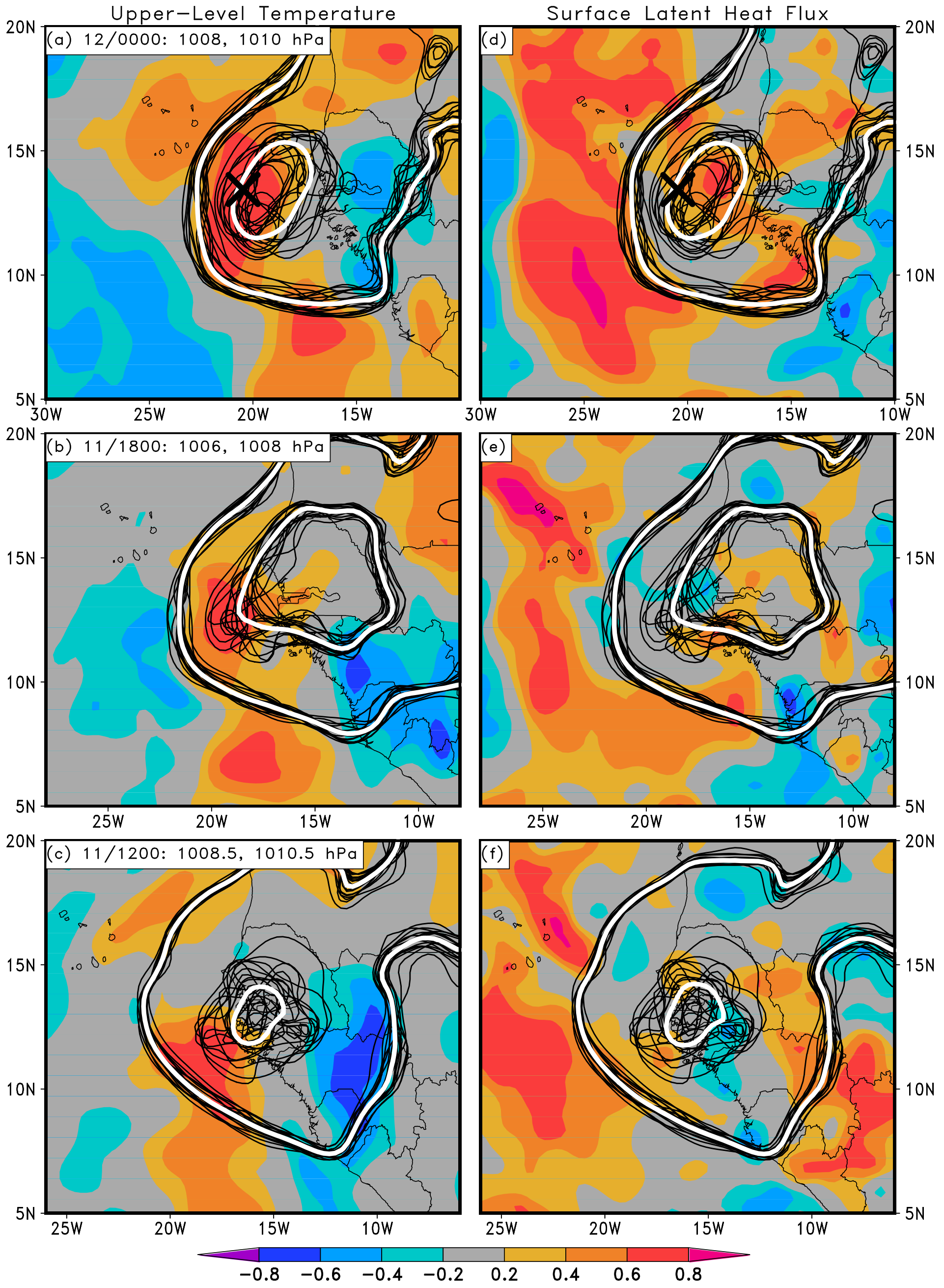

Figure 3.21: Ensemble sensitivity [Eq. (3.1), shaded] of the 0000 UTC 12 Sep MSLP EOF 1 (Fig. 3.16b) PC values to (a) – (c) the 400-150 hPa layer-averaged temperature anomalies; and (d) – (f) surface latent heat flux anomalies (±0.42 is statistically significant at the 95% confidence interval). Spaghetti plots for each member's MSLP (black contours, hPa) and ensemble mean (bold white contour) are overlaid for various isobars. The sensitivities are given at (a) and (d) 0000 UTC 12 Sep (i.e., the time at which the EOF pattern is valid); (b) and (e) 1800 UTC 11 Sep; and (c) and (f) 1200 UTC 11 Sep. The maximum amplitude location of the respective EOF pattern is marked in (a) and (d) by an ×.

(Fig. 3.16b), the upper-tropospheric temperatures must increase accordingly. The cluster of ensemble members whose MSLP minimum are directly collocated with the statistically significant correlations supports the importance of upper-tropospheric temperature anomalies for MSLP falls during TCG, as well as the faster developers at 12/0000 (cf. Figs. 3.16a,b and 3.21a).

In contrast, the correlation between the PC and surface latent heat flux anomalies is weaker near the peak amplitude of EOF 1, though still reaching statistically significant correlations in collocation with the cluster of ensemble members (Fig. 3.21d). Much larger correlations with the surface heat flux exist well away from the developing MSLP centers, suggesting stronger winds on the fringes of the developing low-level circulation (Fig. 3.21d). Additionally, this correlation should be thought in the context of that the winds associated with the pre-TD Julia in all members are not capable of employing the WISHE for intensification. Thus, the association can be thought of as substantial variance in the low-level wind speed within the ensemble.

Tracing the sensitivities back in time, it is evident that the upper-tropospheric temperature anomalies at 11/1800 correlate well with the MSLP EOF 1 variance explained at 12/0000 (Fig. 3.21b). This is contrasted by the surface latent heat flux anomalies whose correlation with the PC quickly diminishes prior to 12/0000 near the ensemble cluster (Figs. 3.21e,f). This reduction is as expected, however, as prior to 12/0000, the sustained surface winds associated with the pre-TD Julia are mostly below 10 m s^{-1} in all ensemble members and they occur mainly over land. A stronger correlation to surface latent heat flux anomalies still exists well west from the storm centers, again implying increased winds on the fringes of the developing circulation (Figs. 3.21e and 3.21f). The positive correlation between the upper-tropospheric temperature anomalies and the PC continues at 11/1200 with a slight eastward shift towards the coastline (Fig. 3.21c).

3.5.3.2 Upper-tropospheric Temperature 12/0000 EOF 1 Sensitivity

Fig. 3.22 shows the sensitivity of the leading EOF of upper-level temperature anomalies to the 400-150 hPa layer-averaged relative divergence and composite radar reflectivity anomalies. We see that near and to the north of the ensemble cluster center of -36.9°C isotherms strong positive sensitivities occur between the PC of the leading EOF and 400-150 hPa relative divergence (Fig. 3.22a). This result indicates that to reproduce EOF 1 and its positive 400-150 hPa layer-averaged positive temperature anomalies, enhanced divergence in the same layer must occur (e.g., an enhanced storm-scale outflow). This sensitivity near the storm cluster is the largest magnitude correlation within the domain that the sensitivities are calculated within, suggesting that there is a physical mechanism behind the correlation, and thus, do not represent a “false” sensitivity. In a similar fashion to the relative divergence, strong positive correlations exist between the PC and composite radar reflectivity (Fig. 3.22d). Such a positive correlation alludes to the need for enhanced convection (positive composite reflectivity anomalies) to reproduce the positive temperature anomalies of EOF 1 (cf. Figs. 3.19b and 3.22d). These connections are consistent with our findings previously, which noted that enhanced deep convection enabled a more coherent storm-scale outflow, and thus, an accumulation of warmth in the upper-troposphere as the Rossby radius of deformation shrinks.

At 11/1800, the sensitivity of the upper-tropospheric temperature variance to upper-level divergence and deep convection becomes much less clear. While strong positive correlations between the leading EOF and divergence appear just off the coastline (Fig. 3.22b), weak correlations, if any, exist further east near the ensemble cluster. Given that the maximum amplitude of the EOF is purely situated over water, it is believed that the positive correlations seen off the coastline in Fig. 3.22b do represent the propagation of statistically significant correlations eastward back in time, e.g., with the propagation of the convective activity. This is further supported by the statistically significant correlations just off the coastline at 11/1200 (Figs. 3.22c and 3.22f), consistent with progression of the AEW and embedded convection off the west African coast.

3.5.4 Dominant ensemble differences during the TD stage

As the ensemble solutions evolve, differences between the ensemble members become increasingly evident. A schism between developers and non-developers was alluded to earlier in this chapter and also demonstrated distinct differences in the ensemble when comparing the MSLP disturbances with upper-tropospheric warming. Even with such a dichotomy, 18 of the 20 ensemble members generate a storm with a $\mathrm{P_{MIN}}$ greater than the NHC estimate of 1007 hPa. Furthermore, the ensemble mean $\mathrm{P_{MIN}}$ of 1004 hPa is 1 hPa stronger than the control simulation. This

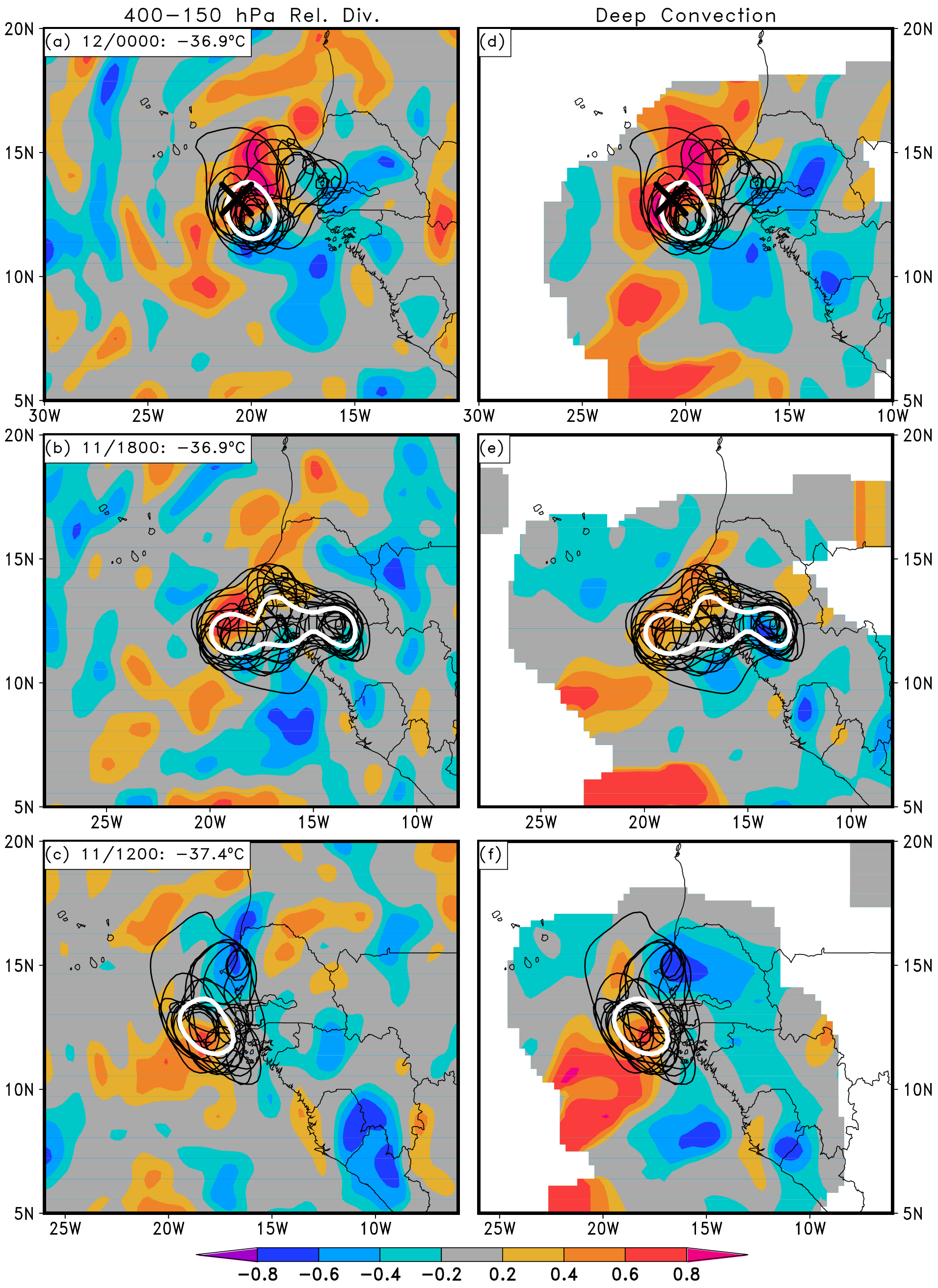

Figure 3.22: As in Fig. 3.21, except for the leading EOF of the 0000 UTC 12 Sep upper-tropospheric temperature anomalies (Fig. 3.19b) and its sensitivity to (a) – (c) 400-150 hPa layer-averaged relative divergence anomalies; and (d) – (f) the composite radar reflectivity anomalies (d-f). The sensitivities depicted in (d) – (f) are only plotted for radar reflectivities greater than 0 dBZ for all ensemble members and the ensemble mean. Otherwise, the sensitivities are masked out since convection does not exist (i.e., composite radar reflectivities at or below 0 dBZ). Spaghetti plots for each member's 400-150 hPa layer-averaged temperature (black contours, °C) and ensemble mean (bold white contour) are overlaid for various isotherms.

increase in storm intensity spread co-exists with fundamental changes in the spread of upper-tropospheric temperatures and meso-α-scale variability in deep convection.

3.5.4.1 Variability in MSLP

The MSLP ensemble spread, ensemble mean and the leading patterns of spread for 12/0600 are given in Fig. 3.23, showing that the ensemble spread evolves from its 12/0000 spread pattern into a single monopole ("M_1") centered near the ensemble mean and the cluster of $\mathrm{P}_{\mathrm{MIN}}$ centers with little extension back towards the coastline. As expected, the magnitude of ensemble spread further increases from that at 12/0000, demonstrating the divergence of the ensemble member solutions.

As with 12/0000, the leading EOF pattern depicts that the main disagreement between ensemble members is the intensity of the developing Julia (Fig. 3.23b). However, this pattern only explains 45% of the total spread, a reduction of 2.3% from the similar monopole pattern at 12/0000 (cf. Figs. 3.23b and 3.16b). This change is complemented by an increase in variance explained by EOF 2, which portrays a dipole of positional disagreements centered near M_1 with an explained variance of 30.9%. This represents an increase of 4.7% over the positional differences EOF at 12/0000. Even with the change in the amount of total variance explained, the dominant mode of ensemble disagreements between ensemble members regarding TD Julia is storm intensity, followed by a northwest-southeast positional disagreements.

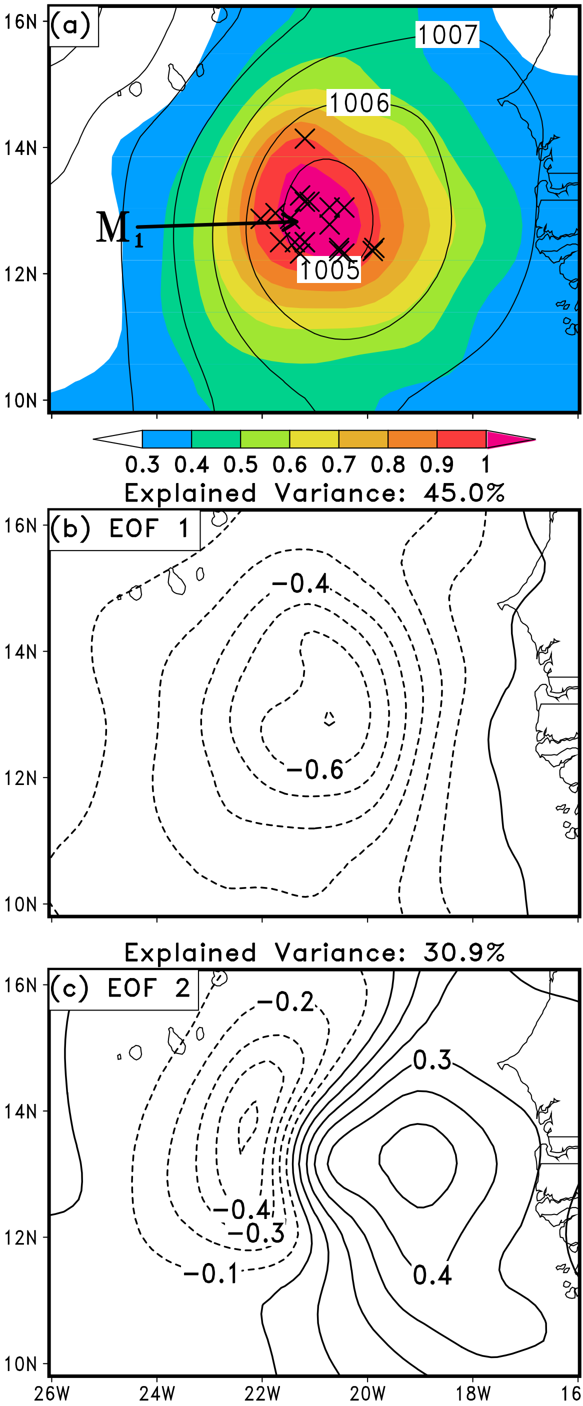

Figure 3.23: As in Fig. 3.15, but valid for 0600 UTC 12 Sep.

3.5.4.2 Variability in 925-hPa absolute vorticity

In a similar fashion to the MSLP variance, the transformation from the two maximum spread centers at 12/0000 to one center at 12/0600 appears in the 925-hPa absolute vorticity as well ("V_1", Fig. 3.24a). This spread exceeds 8×10^{-5} s^{-1} with the ensemble mean exceeding 12×10^{-5} s^{-1} centered on the heightened spread. They represent increases of 2×10^{-5} s^{-1} and 5×10^{-5} s^{-1} from their 12/0000 magnitudes, respectively, exemplifying the divergence in ensemble solutions for the development of the LLV. Enhanced ensemble spread extends north of V_1, suggesting some member disagreements extending to the north of the ensemble cluster. In addition to this northward spread, the maximized spread at V_1 is nearly collocated with the locations of maximum spread of MSLP intensity (cf. Figs. 3.23a and 3.24a).

The leading EOF pattern represents east-west positional uncertainties associated with the developing LLV, explaining 27.4% of the variance (Fig. 3.24b). This pattern is followed by intensity disagreement shown in EOF 2, which has a monopole centered near V_1 and explains 18.1% of the variance. Finally, EOF 3 shows the north-south positional disparity that the ensemble spread alluded to (cf. Figs. 3.24a and 3.24d). Using these EOF patterns, it is clear that the development of the LLV is underway in the majority of ensemble members with positional and intensity differences that are isolated in the leading EOF patterns.

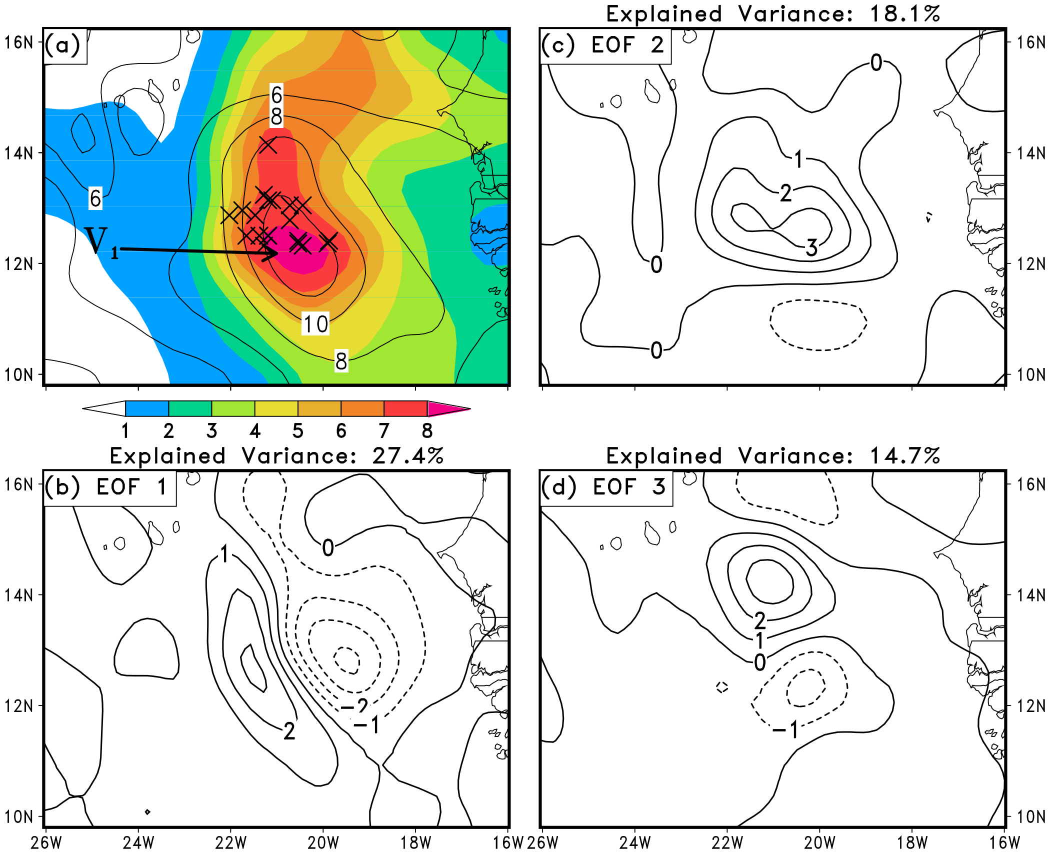

Figure 3.24: As in Fig. 3.15, except for the 925-hPa absolute vorticity ($\times 10^{-5}$ s^{-1}) valid for 0600 UTC 12 Sep, including an additional EOF, i.e., EOF 3 (d), which explains 14.7% of the total variance.

3.5.4.3 Variability in upper-tropospheric thermal anomalies

An increase in the upper-tropospheric temperature variability complements the storm intensity disagreements at 12/0600, as shown in Fig. 3.25a. The ensemble spread of upper-tropospheric temperature exceeds 0.5°C, an increase of 0.05°C from the pre-TD stage (cf. Figs. 3.19a and 3.25a). While this increase in spread is notable, the changes to the spatial characteristics of the spread allude to more significant disagreements in the 400-150 hPa layer-averaged temperature field between ensemble members. Instead of the two maximums seen at 12/0000 (Fig. 3.19a), a single maximum appears at 12/0600 (see "U_1" in Fig. 3.25a), suggesting that the main disagreement between the ensemble members is related to the magnitude of the upper-tropospheric temperature anomalies. Additionally, the maximum at U_1 is directly collocated with the maximum ensemble spread of MSLP anomalies (cf. Figs. 3.23a and 3.25a) and P_{MIN} cluster, which is consistent with the interconnectedness seen at 12/0000. The ensemble mean 400-150 hPa layer-averaged temperatures show a warming of approximately 0.5°C from 12/0000, with a meso-α-scale region of warmth centered on the ensemble spread (Fig. 3.25a).

The leading EOF pattern of upper-tropospheric temperature anomalies at 12/0600 describes ensemble differences on the eastern portion of the ensemble cluster, with a monopole pattern displaced just east of the maximum of ensemble spread (Fig. 3.25b). This pattern explains 42.5% of the total variance, an increase over the 41.7% explained by the leading EOF at 12/0000. EOF 2, explaining 29.2% of the total variance, resembles an uneven dipole with positive magnitude pole displaced

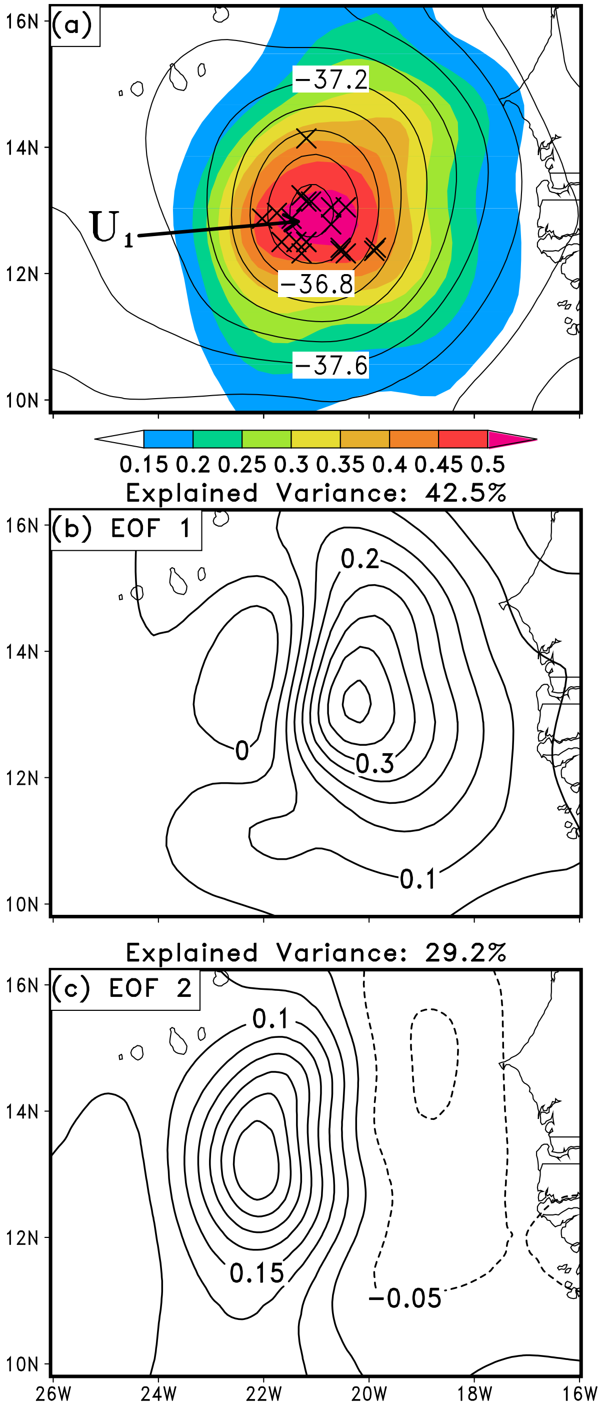

Figure 3.25: As in Fig. 3.15, except for the 400-150 hPa layer-averaged temperature anomalies (°C) valid at 0600 UTC 12 Sep.

westward of U_1 (Fig. 3.25c). While technically a dipole, it is clear that EOF 2 resembles more a monopole feature just west of the center of the largest total variance. The superposition of these two EOF patterns represents both the intensity and positional differences associated with the 400-150 hPa layer-averaged temperature anomalies, with some members displaying an eastward shift in the positive upper-tropospheric temperature anomalies, while others depict a westward shift from the center of maximum total variance. Without the decomposition of the total variance field using EOFs, these characteristics of the ensemble spread would remain unknown, and important features of the ensemble differences would remain overlooked.

3.5.4.4 Variability in convection anomalies

As compared to the pre-TD stage, it is evident that the ensemble mean composite radar reflectivity exhibits a weak MCS with maximum radar reflectivity returns exceeding 30 dBZ, increasing the peak reflectivity by roughly 5 dBZ from 12/0000 (cf. Figs. 3.20a and 3.26a). A major difference from 12/0000 is that the ensemble cluster of P_{MIN} is collocated at the center of the ensemble mean MCS, demonstrating the possibility of substantial convective development near the storm centers of some ensemble members (Fig. 3.26a). However, in a fashion similar to that at 12/0000, the ensemble spread is maximized to the north of the ensemble mean center and exceeds 14 dBZ, signifying substantial disagreement between the ensemble members on the northern extent of convective development.

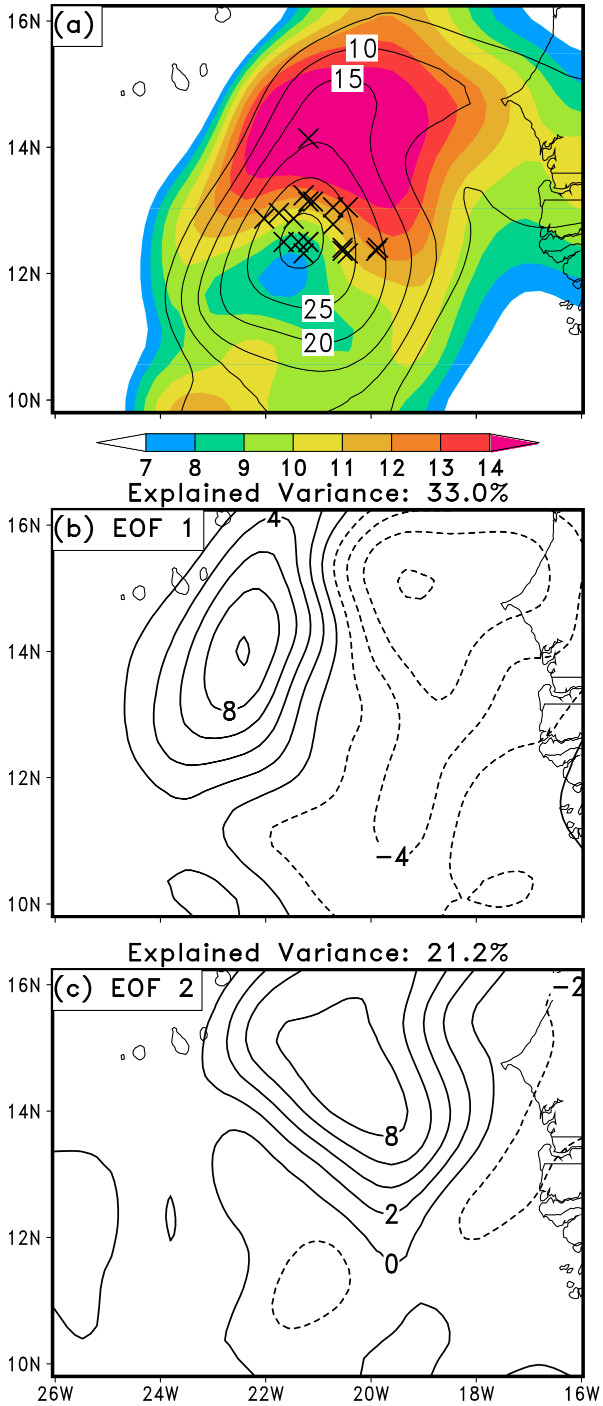

Figure 3.26: As in Fig. 3.15, except for the composite radar reflectivity anomalies (dBZ) valid at 0600 UTC 12 Sep.

Pulling out the leading EOF yields that the most reoccurring disagreement between ensemble members for composite radar reflectivity anomalies represents predominately positional disagreements (Fig. 3.26b). Even though weak, the uneven magnitude of the dipole depicts that the EOF pattern is not purely positional and includes some intensity differences between ensemble members. EOF 2 depicts intensity disagreement centered on the maximum of ensemble spread with a magnitude exceeding 8 dBZ (Fig. 3.26c). These two patterns demonstrate that the main ensemble spreads of deep convection are related to the west-east position as well as the strength of deep convection to the north of the ensemble mean. Additionally, the patterns of spread and EOFs match the variance and EOFs of the low-level vorticity (cf. Figs. 3.24 and 3.26), suggesting the possible roles of convectively-generated vortices in the formation of the LLV.

3.5.5 Ensemble sensitivity analyses at the TD stage

3.5.5.1 MSLP 12/0600 EOF 1 sensitivity

Fig. 3.27 presents the ensemble sensitivity analysis for PC 1 of MSLP anomalies (Fig. 3.23b). The instantaneous sensitivity (Figs. 3.27a,d) is strongly positive near the 1006-hPa ensemble cluster with correlations exceeding 0.8 for both parameters. A notable increase from 12/0000 in the instantaneous sensitivity between the PC and surface latent heat flux anomalies occurs with correlations exceeding 0.6 for the majority of the ensemble cluster. This is further evidenced by the substantially larger region of statistically significant correlations, alluding to the increase in intensity and spatial extent of the low-level circulation field as exemplified 1009-hPa ensemble cluster (Fig. 3.27d). The strongest correlations between the PC and upper-tropospheric temperature exist to the southwest of the ensemble cluster, suggesting enhanced MSLP variance resulting from the upper-tropospheric temperatures downstream of the greatest MSLP variance (Fig. 3.27a). The ensemble mean surface maximum wind exceeds 12 m s^{-1}, and thus, WISHE can be employed for generating MSLP falls in the stronger ensemble members. Since PC 1 is strongly correlated with both parameters within the ensemble cluster at 12/0600, we may state that both hydrostatically-induced and WISHE-induced MSLP falls are occurring and are dependent on the strength of the ensemble member disturbance.

Tracing the sensitivities back in time, statistically significant positive correlations between PC 1 and upper-tropospheric temperature anomalies exist back until 11/1800 near the ensemble cluster and within the general larger-scale disturbance encompassed by the 1010 hPa isobar cluster at 12/0000 (Figs. 3.27b,c). On the other hand, the positive correlations between PC 1 and surface latent heat flux anomalies diminish quickly, with an indiscernible correlation at 11/1800 (Figs. 3.27e,f). The most notable reduction of statistically significant positive correlation exists between 12/0600 and 12/0000 as the most robust correlations are confined to the edges of the developing low-level circulation (Fig. 3.27e). Some statistically significant correlations exist with the latent heat flux anomalies near the ensemble cluster, but is much less meaningful when compared to the upper-tropospheric temperatures (cf. Figs. 3.27b and 3.27e). The reduction in correlations with surface latent heat flux anomalies makes physical sense, however, as the ensemble mean surface maximum

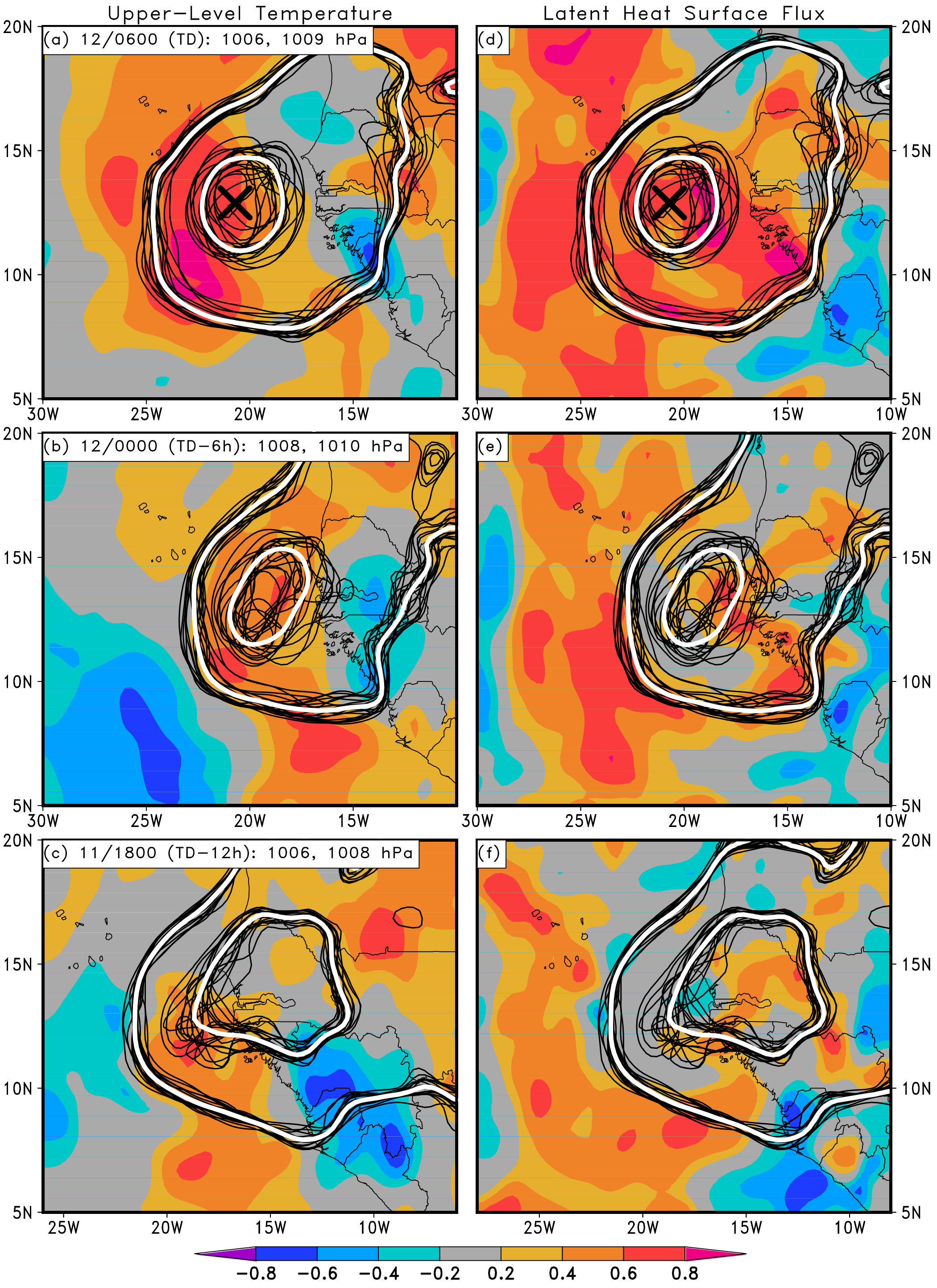

Figure 3.27: As in Fig. 3.21, except for the sensitivity of the 0600 UTC 12 Sep MSLP EOF 1 (Fig. 3.23b) PC values.

sustained wind speed is below 10 m s^{-1} at 11/1800, and thus, the MSLP variance at 12/0600 is unlikely to be caused by positive surface latent heat flux anomalies via WISHE at 11/1800.

3.5.5.2 Upper-tropospheric temperature 12/0600 EOF 1 and 2 sensitivities

Since both EOFs patterns depicted in Figs. 3.25b and 3.25c represent important features of the upper-temperature ensemble spread, it is of interest to examine the sensitivity of both EOFs to the 400-150 hPa layer-averaged relative divergence and composite radar reflectivity anomalies.

Fig. 3.28 shows the sensitivity of EOF 1 to upper-level divergence and deep convection. As at 12/0000, a strong positive instantaneous sensitivity exists between the PC of the EOF and both meteorological parameters near the ensemble cluster and maximum amplitude of the EOF pattern (see "×" in Figs. 3.28a and 3.28d). These positive sensitivities shift eastward back in time as the upper-tropospheric temperatures at 12/0600 are well correlated with enhanced deep convection and divergence propagating off the west African coastline. Similar patterns and correlations are seen for the second EOF (Fig. 3.25c) with relevant positive correlations with divergence and composite radar reflectivity anomalies near the ensemble cluster and maximum amplitude location of the EOF (Fig. 3.29). While other sensitivities exist for both EOFs away from the ensemble clusters, they are generally of less magnitude than those of the sensitivities near the cluster, and thus, yield little, if

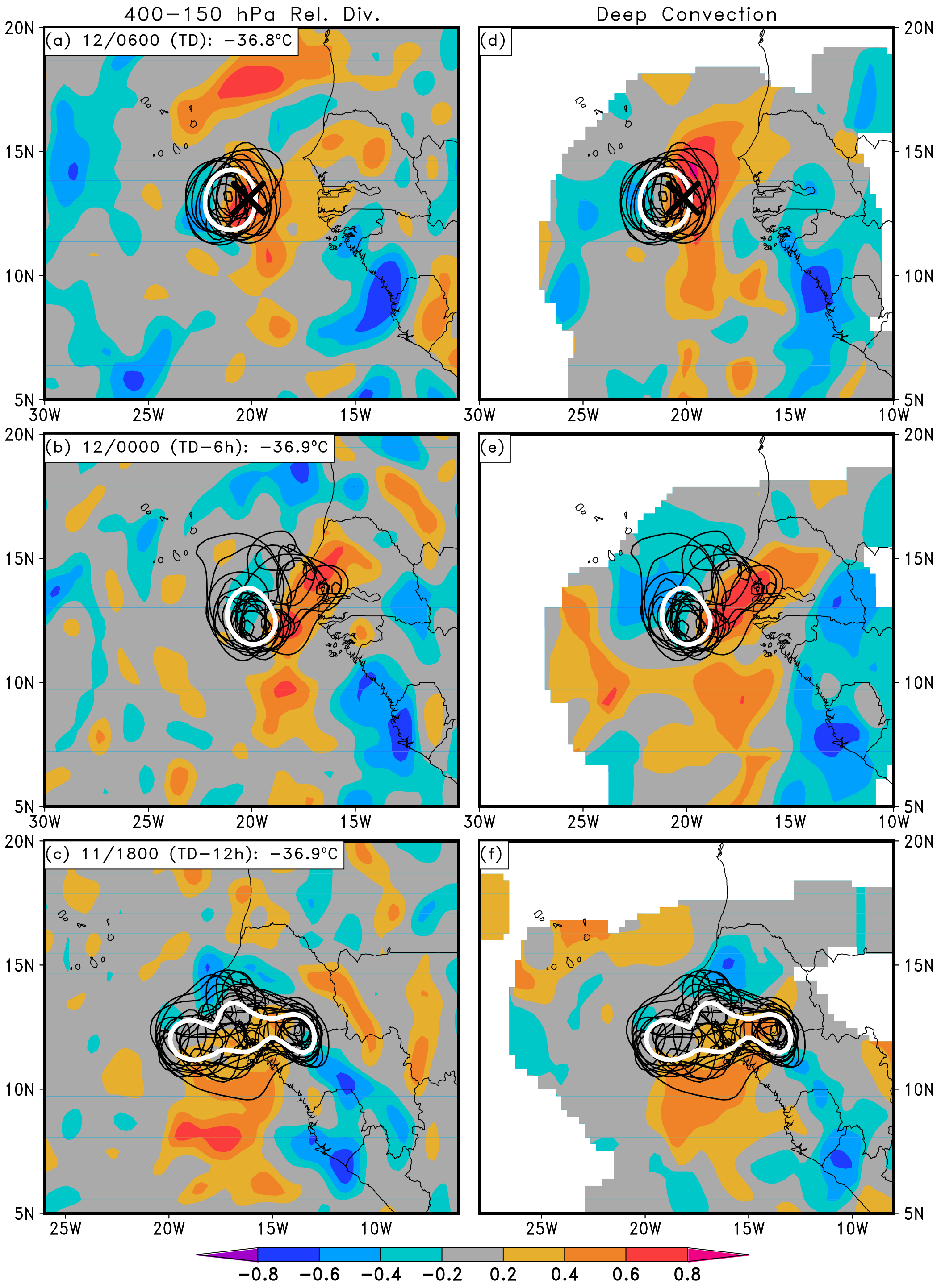

Figure 3.28: As in Fig. 3.22, except for the sensitivity of the 0600 UTC 12 Sep upper tropospheric temperature EOF 1 PC values (Fig. 3.25b).

any, meaningful information on the implications for the EOF patterns examined.

3.5.6 Summary and discussion

The previous constructed EOFs for multiple parameters to identify the dominant patterns of ensemble spreads for the TCG of Hurricane Julia (2010). Using these parametric patterns of differences, we are able to make inferences for the dominant mechanisms responsible for the ensemble spreads, and for how each of the spread of the multiple parameters are connected. Two main stages were investigated for parametric ensemble differences: i) pre-TD stage; and ii) TD stage.

It is found that the dominant pattern of MSLP disagreements is related to the intensity of the pre-TD and TD Julia, explaining nearly half of the total ensemble variance at both times. The second leading mode of variance for MSLP is related to the position of the developing TD Julia, demonstrating the difference between faster and slower developing members. Similar patterns are found in the variance of 925-hPa absolute vorticity, though with much less explained variance per EOF.

The ensemble spread in MSLP and low-level absolute vorticity is complemented by similar patterns of variance in upper-tropospheric temperatures, suggesting that the variance of the variables are linked. At the pre-TD stage, the maximum of multiple MSLP variance centers are collocated with centers of the maximum upper-tropospheric temperature variance. As the MSLP variance pattern morphs into a monopole pattern during the TD stage, so does the upper-level temperature variance, closely located to the cluster of ensemble member storm cen-

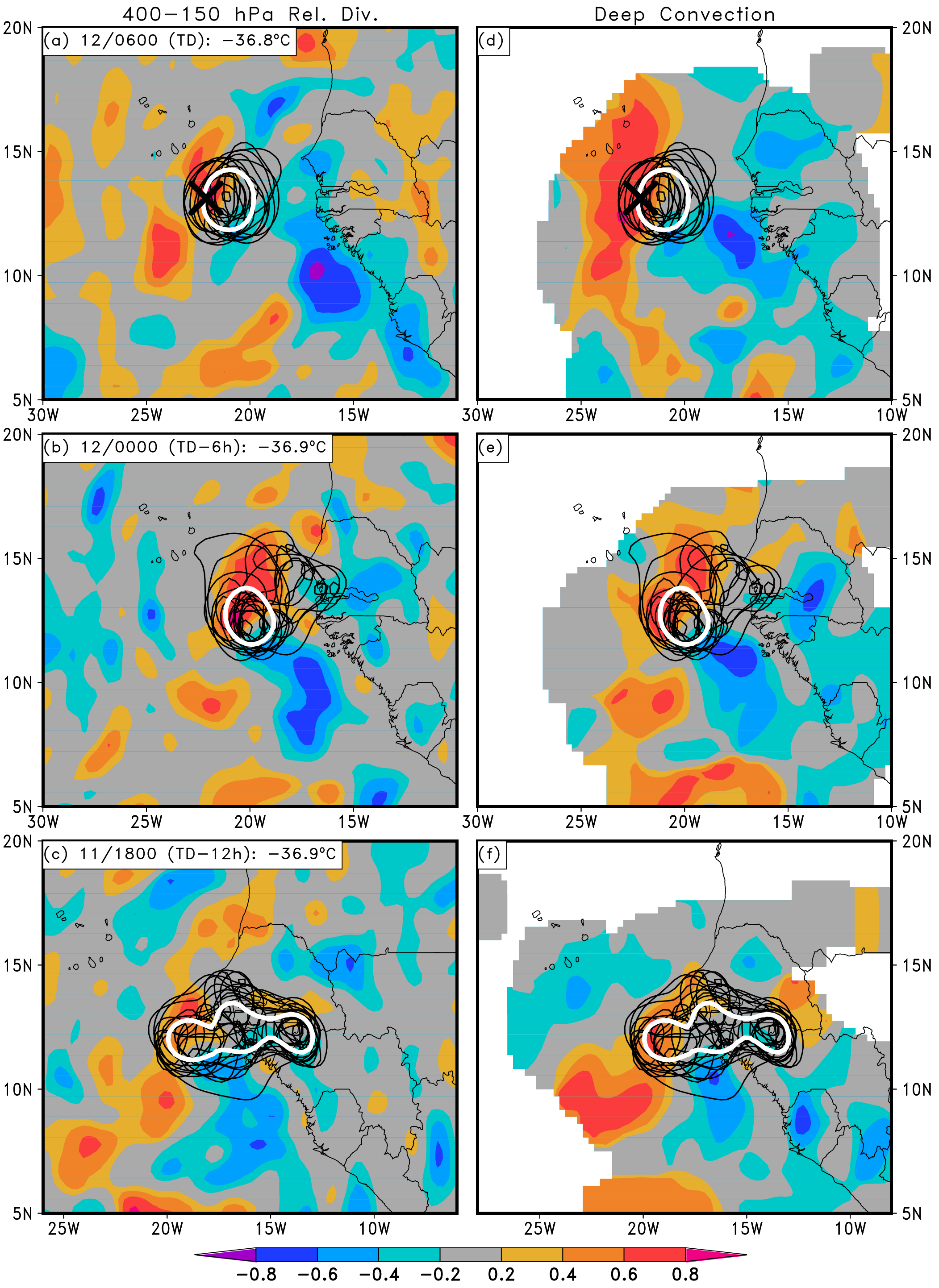

Figure 3.29: As in Fig. 3.22, except for the sensitivity of the 0600 UTC 12 Sep upper tropospheric temperature EOF 2 PC values (Fig. 3.25c).

ters. Consistent with the pre-TD stage, the EOFs at the TD stage depict the same characteristics, but characteristic patterns representing faster and slower developing members, instead of just one group of ensemble members.

To examine what causes the MSLP changes during TCG, ensemble sensitivity analyses were performed to compare if upper-tropospheric temperature anomalies or WISHE are responsible for the MSLP changes at both stages. At the pre-TD stage, strong positive sensitivities exist between the upper-tropospheric temperature anomalies and the EOF representing negative MSLP anomalies (e.g., a stronger pre-TD Julia). This sensitivity is coherent and traceable back in time, suggesting that to make the pre-TD Julia stronger, increases in upper-tropospheric temperatures must occur in the hours prior and at 12/0000. Contrasting this result, the sensitivity of the EOF pattern to surface latent heat flux anomalies at the pre-TD stage is less robust. While some positive correlation exists instantaneously, the sensitivity quickly diminishes back in time. Links between upper-tropospheric temperature anomalies and deep convection are illustrated through further ensemble sensitivity analyses. It is evident that the strength of the upper-level warming during TCG is positively correlated to enhanced composite radar reflectivity anomalies (e.g., enhanced deep convection) and its divergent outflow.

Overall, the EOF and ensemble sensitivity results paint a more holistic picture describing the predictability of TCG of Hurricane Julia through a variety of statistical inferences of important meteorological parameters for the occurrence of TCG. The methods herein would benefit other studies using ensembles to investigate particular meteorological phenomena, including TCs. Identifying the dominate characteristics of the ensemble as a whole can provide a much more robust analysis than investigating and comparing individual ensemble members. That being said, the method does have its deficiencies, mainly that statistical inferences of dynamical processes can yield unrealistic conclusions, or ones that do not adhere to the governing equations. Regardless of this shortcoming, the results of this section provide insight on the dominant modes of variability occurring during TCG and elucidate how the variability of multiple parameters is woven together.

Chapter 4: The impacts of ice cloud microphysics on genesis

4.1 Introduction

While numerous studies have investigated the impacts of cloud microphysical processes on track and intensity changes of mature TCs, little work has identified any impacts of these processes on TCG, defined as the transition of a non-developing tropical disturbance into a developing one. Given the range of scales that TCG takes place across, it seems intuitive that cloud microphysical processes play an important role in aiding (or deterring) the development of a pre-TD disturbance.

The impacts of microphysical processes on the intensity of mature TCs has been studied extensively for several decades now, dating back to a study by Lord et al. (1984), who studied the use of a 3-class ice microphysics scheme versus a no-ice scheme for the development of an idealized TC. Obviously, the use of ice microphysical processes created a more realistic representation of the idealized TC, while the results set the stage for discussion on the roles of cold-cloud microphysics for TC development. More recently, other studies have used advanced models and idealized experiments to show significant changes to TC intensity as a result of modifications to the microphysics scheme (e.g., McFarquhar et al. 2006; Wang 2002; Zhu and Zhang 2006). Notably, the study by Zhu and Zhang (2006) found significant differences for the intensity of Hurricane Bonnie (1998) and the inner-core structure of the storm by modifying certain parameters of the microphysics scheme used in the control simulation. Specifically, they removed various processes (such as the melting of ice, snow and graupel) and compared the results to a control simulation. The results demonstrated that removing all ice microphysics produced the weakest storm of the sensitivity simulations, exemplifying the importance of water phase changes to the intensity of a mature TC.

Of particular interest to this study is how TCG is impacted by ice microphysics and related heating. We previously have alluded to and demonstrated that the intensity of pre-TD disturbances inspected in chapters 2 and 3. This warming hydrostatically induces meso-α-scale MSLP falls that lead to the development of the MSLP $\mathrm{P_{MIN}}$ disturbance, and subsequent LLV. Furthermore, we have postulated that the upper-tropospheric warming during TCG results partly from depositional heating due to persistent deep convection and storm-scale outflow expanding the warm air out over a meso-α-scale region. From the large magnitudes of cloud ice mixing ratios collocated with the upper-level warming shown previously, we concluded that the warming resulted from depositional growth of cloud ice within strong convective vertical motions (e.g., CBs) found during the TCG process. Expanding upon our previous results, the following will investigate the role of cloud microphysical processes in the TCG of Hurricane Julia.

4.2 Experimental design and model details

To conduct the sensitivity experiments, this study modifies the WRF model setup used to create the control simulation described in chapter 2. Version 3.2.1 of the fully compressible, nonhydrostatic mesoscale WRF model with ARW core (Skamarock et al. 2005) is used with three nests (9/3/1 km) as depicted by the boxes given in Fig. 2.3 (D1, D2, and D3, respectively). The sensitivity simulations are initialized at 10/0000 and end at 12/1800, when the NHC center declared Julia a TS, in the same fashion as the control. Thus, the simulations are integrated for a total of 66 h with TCG taking place 54 h into the integration at 12/0600. As with the control, the lateral boundary and initial conditions are supplied by the ERA-Interim analysis except for SSTs. Instead, SSTs are obtained from the NOAA Optimal Interpolation high-resolution SST data set (Reynolds et al. 2007) valid at 10/0000, and remain fixed for entire integration. The 9- and 3-km resolution domains incorporate simultaneously the Kain-Fritsch convection parameterization scheme (Kain 2004; Kain and Fritsch 1990), while this scheme is bypassed in the 1-km resolution domain. The sensitivity simulations also utilize the the Rapid Radiative Transfer Model (RRTM) longwave radiation scheme (Mlawer et al. 1997), the Dudhia (1989) shortwave radiation scheme, and the Yonsei University (YSU) planetary boundary layer (PBL) scheme (Noh et al. 2003).

The control and sensitivity simulations employ the Thompson graupel 2-moment microphysics scheme (Thompson et al. 2008, 2004). This scheme predicts the mass tendencies of cloud water, rain water, cloud ice, snow, and graupel, while also predicting the number tendencies of cloud water and ice. As mentioned previously, the study herein focuses on the warming of the upper troposphere during TCG. Thus, the modifications made to the Thompson scheme are simple yet yield substantial changes to upper troposphere thermodynamic characteristics, and in turn, the development of the pre-TD disturbance.

A summary of the experimental design is given in Table 4.1. The first experiment, named “No Fusion”, removes the latent heat of fusion in depositional growth and sublimation to study the impacts of fusion heating during TCG. Since we have shown a large accumulation of cloud ice content aloft during the TCG of Hurricane Julia, this experiment will remove the heating associated with cloud ice generation. The Thompson scheme defines the enthalpy of sublimation, vaporization, and fusion using standard values found at 0°C: enthalpy of vaporization ($\mathrm{L_V}$) = 2.5×10^{6} J kg^{-1}; enthalpy of sublimation ($\mathrm{L_S}$) = 2.834×10^{6} J kg^{-1}, and enthalpy of fusion ($\mathrm{L_F}$) = 3.34×10^{5} J kg^{-1}. Examining $\mathrm{L_S}$, it is obvious that the enthalpy released into the environment from deposition is just the sum of the enthalpy of vaporization and fusion: $\mathrm{L_S} = \mathrm{L_V} + \mathrm{L_F}$. Thus, the sensitivity experiment removes the latent heat of fusion from this sum, still allowing for condensational heating and evaporational cooling: $\mathrm{L_S} = \mathrm{L_V} = 2.5\times10^{6}$ J kg^{-1}. The modification still allows for the portion of cloud water mass to become cloud ice and only reduces the amount of heating released into the environment during this process by that of $\mathrm{L_F}$.

In addition to deposition, it is possible that homogeneous freezing aids in the upper-tropospheric warming given the strong vertical motions (i.e., CBs) during TCG. Thus, it is worthwhile to investigate if any rapid transport of cloud water

Table 4.1: Summary of the experimental design.

Experiment	Description
Control	Control simulation with Thompson microphysics scheme
No Fusion	As in the control but with $L_S = L_V$
No HFRZ	As in control but with no homogeneous freezing

to upper troposphere and subsequent homogeneous freezing occurs during TCG. In the Thompson scheme, the temperature at which all cloud water must be frozen to become cloud ice is 235.16K. At or below this temperature, the scheme recalculates the tendencies of cloud ice mixing ratio and number concentration, then calculates the new temperature tendency based on the mass of cloud water remaining below 235.16K. To test the impacts of homogeneous freezing on the upper-tropospheric warming, the second sensitivity experiment removes any homogeneous freezing and is called experiment "No HFRZ" (Table 4.1). To remove homogeneous freezing, the temperature at which cloud water must turn to cloud ice is changed from 235.16K to 100K. This temperature effectively turns off any homogeneous freezing as the temperatures will never get to or below 100K during the model integration.

4.3 Results

The following will describe the results of each sensitivity experiment in relation to the control. Obviously, the main focus is on the changes to the thermodynamic structure of the upper troposphere, and in turn, the implications for the developing pre-TD MSLP disturbance. Before going in depth on the simulation differences, we will examine the first-order results (e.g., track and P_{MIN} intensity) to determine any notable differences. These results will be followed by a more holistic look at the changes to the upper troposphere, deep convection, and other pertinent variables for TCG.

4.3.1 Track and intensity differences

As shown in Fig. 4.1a, very minimal track differences exist between the ensemble members. These minimal differences include the phase speed of the system and its period of coastal transition. While little track differences exist, the same is not true for the P_{MIN} of the developing disturbance. When compared to the control, the two sensitivity experiments have nearly similar P_{MIN} as the control prior until 11/1200, albeit with some variability (Fig. 4.1b). After this time, the No Fusion solution starts to diverge from the control and No HFRZ simulations in concurrence with differences in the development and extent of deep convection at 11/1800 (cf. Figs. 4.1b and 4.2a-c).

By 12/0000, the No Fusion simulation depicts a P_{MIN} disturbance approximately 2 hPa weaker than the control and a much less coherent mesoscale convective system (MCS; cf. Figs. 4.1b and 4.2d-f). These differences between No Fusion and the control continue at 12/0600 with the No Fusion experiment exhibiting a less spatially expansive and weaker MCS (Fig. 4.2g) and weaker MSLP disturbance (Fig. 4.1b). By the end of the 66-h integration, the No Fusion simulation never develops a TD while the other simulations go onto strengthen the TD into a TS at

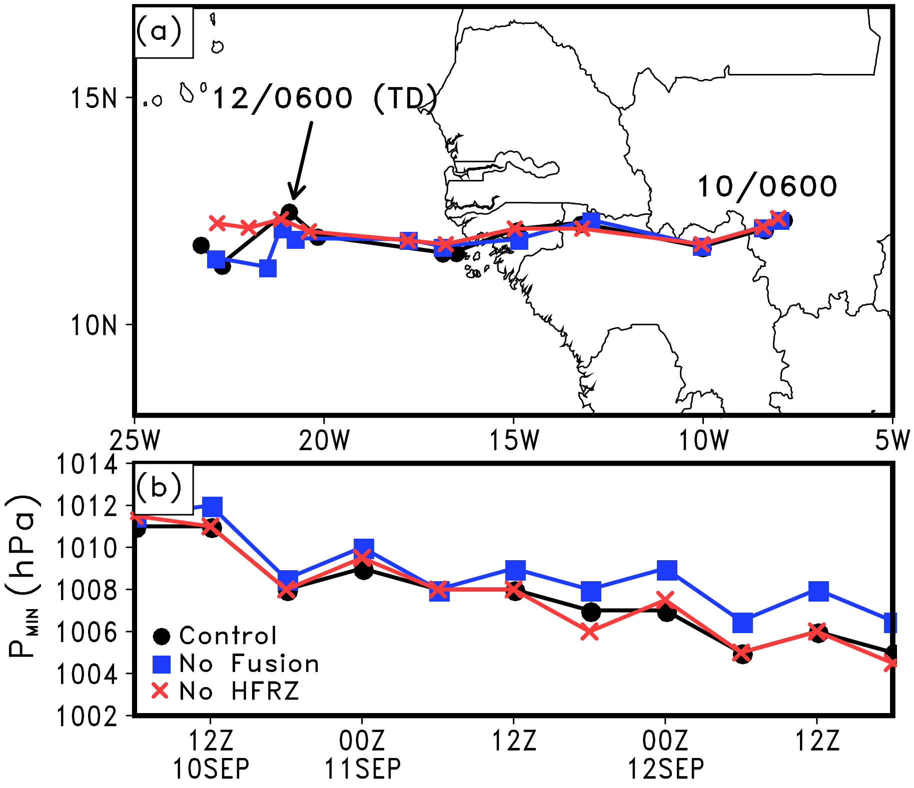

Figure 4.1: Comparison of sensitivity simulations for: (a) track and (b) storm intensity in terms of minimum central pressure (P_{MIN}) from 0600 UTC 10 to 1800 UTC 12 Sep. The control, simulation without fusion heating in deposition, and simulation without homogeneous freezing are given by the black circles, blue squares, and red ×s, respectively.

12/1800. Clearly, the main differences between No HFRZ and the control are much less substantial than the comparison of No Fusion and the control, as demonstrated in the progression of the P_{MIN} disturbances as well as the progression of the MCS (cf. Figs. 4.2b,e,h to 4.2c,f,i).

4.3.2 Upper level and MSLP differences

Given the differences as evidenced in Figs. 4.1 and 4.2, the following will examine the disparity between the simulations in the upper troposphere as well as their connections to differences in the developing MSLP disturbance. Fig. 4.3 depicts the 200 hPa temperature and co-moving wind fields in relation to the MSLP field. Beginning at 11/1800 when the differences between the simulations start to emerge (Fig. 4.1b), it is evident that the control and No HFRZ have 200 hPa temperatures greater than -53°C for a large region just off the west African coast (Figs. 4.3b,c). In contrast, the No Fusion simulation exhibits a much weaker and sporadic area of 200-hPa temperatures greater than -53°C. Such a difference results in a contraction of the 1007 hPa isobar closer to the coastline in comparison to the other simulations (cf. Figs. 4.3a-c).

As deep convection starts to develop in the control and No HFRZ at 12/0000 (Figs. 4.2e,f), 200-hPa temperatures warm in a mesoscale region collocated with the deep convection and a notable mesoscale P_{MIN} disturbances emerge below the upper-tropospheric warming in each simulation (Figs. 4.3e,f). While convective development still occurs in the No Fusion simulation, no warming of the 200-hPa tem-

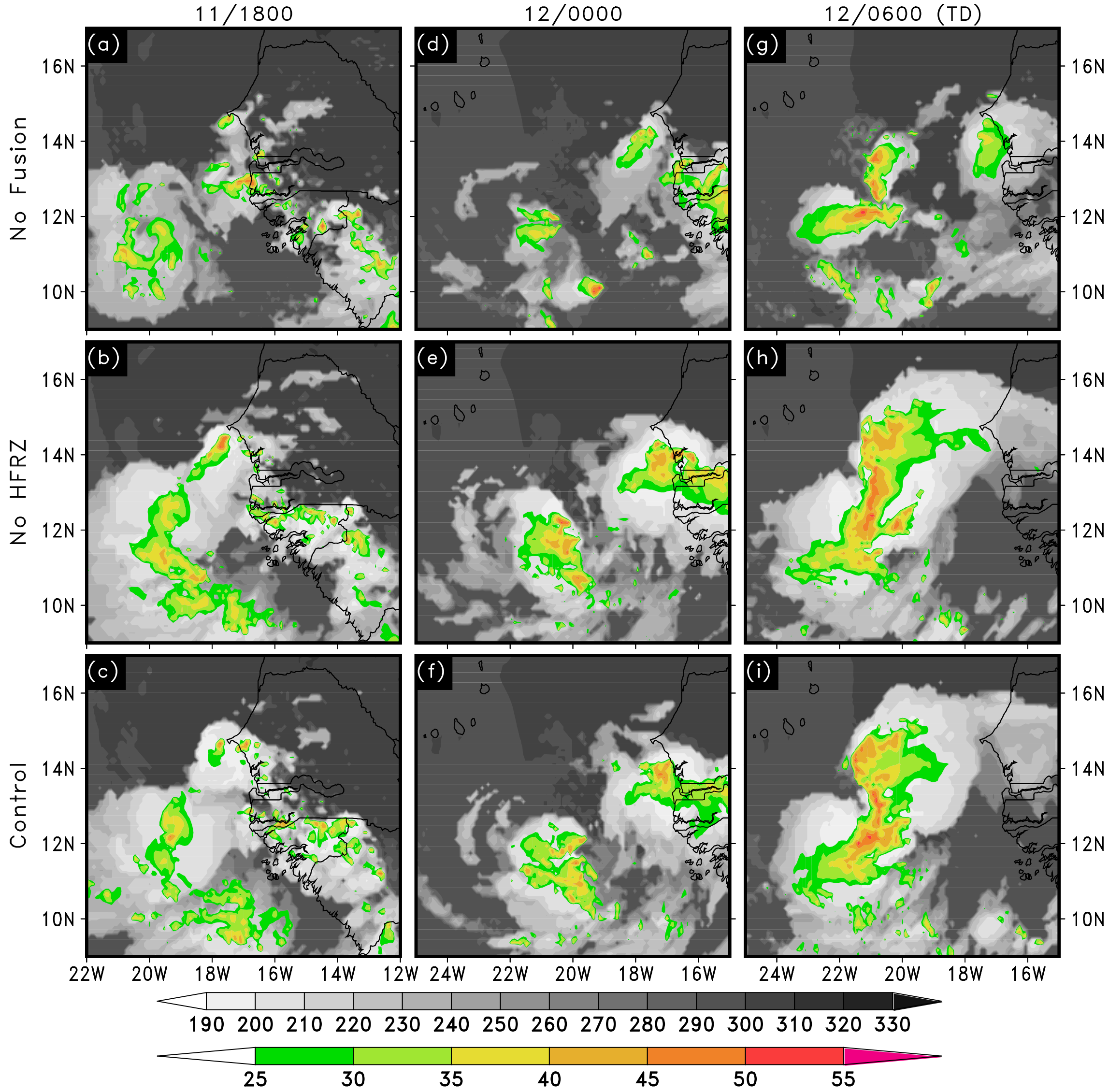

Figure 4.2: Comparison of the top of atmosphere brightness temperature (gray shades, K) and composite radar reflectivity (color shades greater than 25 dBZ) from the simulation without fusion heating in deposition (top row), without homogeneous freezing (middle row), and the control simulation (bottom row) that are valid at 1800 UTC 11, 0000 UTC, 0600 UTC 12 Sep, respectively.

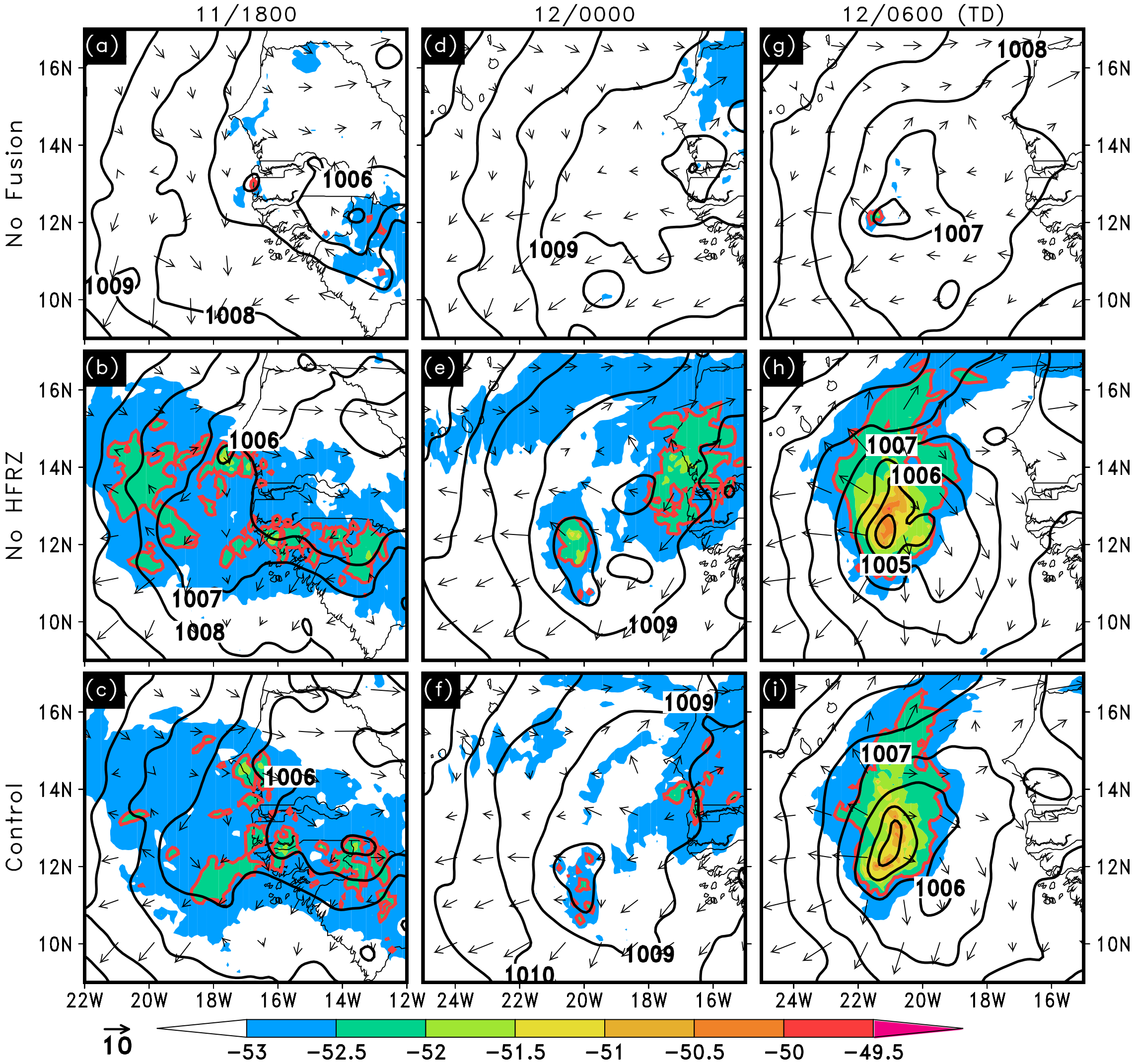

Figure 4.3: Comparison of the 200-hPa temperature (shaded, °C), MSLP (contoured at intervals of 1 hPa), and co-moving wind vectors (reference vector is 10 m s^{-1}) from the simulation without fusion heating in deposition (top row), without homogeneous freezing (middle row), and the control simulation (bottom row) that are valid at 1800 UTC 11, 0000 UTC, 0300 UTC, 0600 UTC 12 Sep, respectively. The -52.5°C isotherm at 200 hPa is contoured bold red to show areal changes of the warming with time. Data from the 9-km resolution simulation are used.

perature field above -53°C exists in collocation with deep convection (cf. Fig. 4.2d and 4.3d). The most notable differences between No Fusion, No HFRZ, and the control exist in terms of upper-tropospheric temperatures at 12/0600 (cf. Figs. 4.3g-i). As the deep convection depicted in Fig. 4.2 invigorates into a more pronounced MCS, substantial warming of the 200-hPa temperatures occur in the control and No HFRZ while such features never form in the No Fusion experiment. The only temperatures above -53°C seen in No Fusion at 12/0600 exist in collocation with the highest model-derived composite reflectivity returns, suggesting the rapid transport of cloud water to temperatures less than 235.16K, and thus, enabling homogeneous freezing (cf. Figs. 4.2g and 4.3g).

Comparing each simulation's warming within a 100 km × 100 km area around each storm's center, Fig. 4.4 depicts the time-height evolution of warming from 11/0600, cloud ice mixing ratio, and absolute vorticity. Focusing on No Fusion (Fig. 4.4a), it is evident that most warming takes place near 275 hPa, or the level at which the 235.16K isotherm resides for the majority of the integration. Thus, it is presumed that the most substantial time-differenced warming (e.g., those in excess of 1°C) are due to homogeneous freezing. This warming is noticeably weaker when compared to the other simulations (cf. Figs. 4.4a,b,c) though, with the differences between the control and No Fusion reaching in excess of 1°C just prior to 12/0600 (Fig. 4.5a). The absolute vorticity field in No Fusion is of weaker magnitude as well, with the midlevel cyclonic circulation associated with the AEW not as pronounced as compared to its counterparts (cf. Figs. 4.4a,b,c). This is complemented by a noticeable difference in the development of the LLV just prior to and after 12/0600, which never takes place in No Fusion (Figs. 4.4a and 4.5a).In contrast to No Fusion, little differences exist between No HFRZ and the control in terms of area-averaged warming. While No HFRZ is more expansive in the warmer 200-hPa temperatures and generates a slightly stronger MSLP disturbance (cf. Figs. 4.3h and 4.3i), its upper-tropospheric warming is only between 0.1 and 0.4°C warmer than that of the control (Fig. 4.5b).

4.3.3 Meso-β-scale structural differences

While the previous section depicted structural differences on the meso-α and synoptic scales, the following will address the disparities on the smaller meso-β and meso-γ scales. As shown in Fig. 4.3, 12/0000 marks a critical time in the development as the MSLP disturbance begins to evolve from a meso-β entity. Investigating this time, Figs. 4.6 and 4.7 highlight the mesoscale features and their differences between each of the simulations. It is worth noting that both figures use a ± 30-min time average centered on 12/0000 in an attempt to eliminate any transient features while isolating on more persistent features. Additionally, the cross sections in Fig. 4.7 use a 3-slice average to ensure that the cross sections capture the most relevant features of the upper troposphere.

At 12/0000, all simulations depict a meso-β-scale MSLP disturbance though it is evident that the No Fusion simulation has the weakest and smallest disturbance being characterized by $\mathrm{P}_{\mathrm{MIN}}$ of just below 1009 hPa and a spatial area of approximately 50 km × 50 km (Figs. 4.6a-c). While notable differences exist for the MSLP

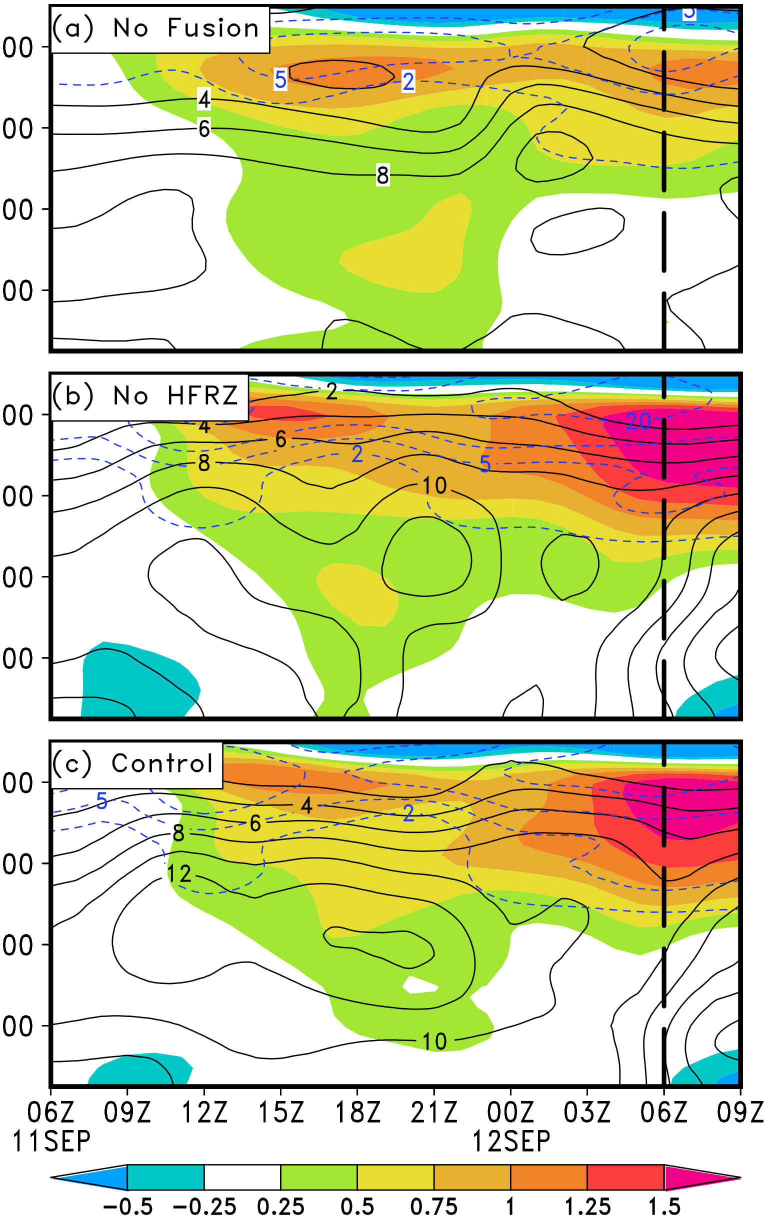

Figure 4.4: Time-height cross section of the temperature differences from the 30-h simulated values (valid at 0600 UTC 11 Sep, shaded, °C), absolute vorticity (contoured every 2×10^{-5} s−1), and cloud ice mixing ratio (contoured in blue at 2, 5, 10, and 20 $\times10^{-4}$ g kg^{-1}) averaged over an area of 100 km × 100 km surrounding the storm center for the simulation without fusion heating in deposition (a), without homogeneous freezing (b), and the control simulation (c). The vertical dashed lines in (a-c) represent the time of TCG as estimated by the NHC.

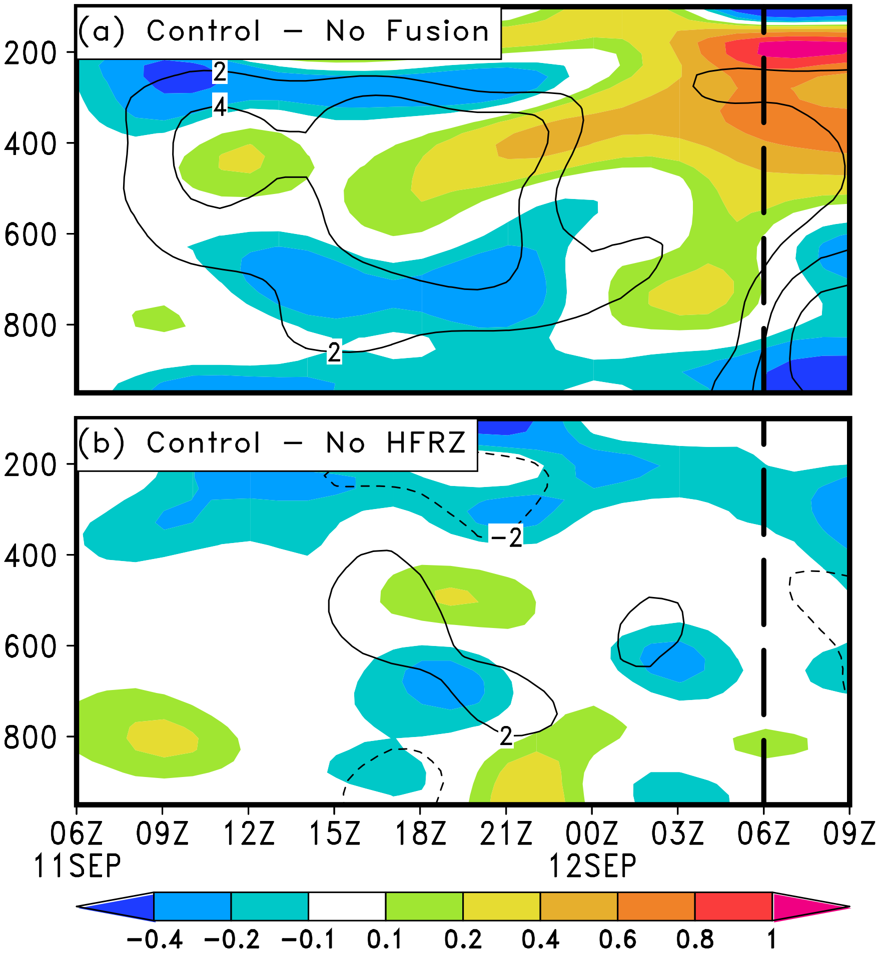

Figure 4.5: Time-height cross section of the simulation differences between the control and simulation without fusion heating in deposition (a) and without homogeneous freezing (b) for temperature difference from the 30-h simulated values (shaded, °C) and absolute vorticity (contoured every 2×10^{-5} s^{-1}) using a 100 km × 100 km area average around each simulation's respective storm center. The vertical dashed lines in (a) and (b) represent the time of TCG as estimated by the NHC.

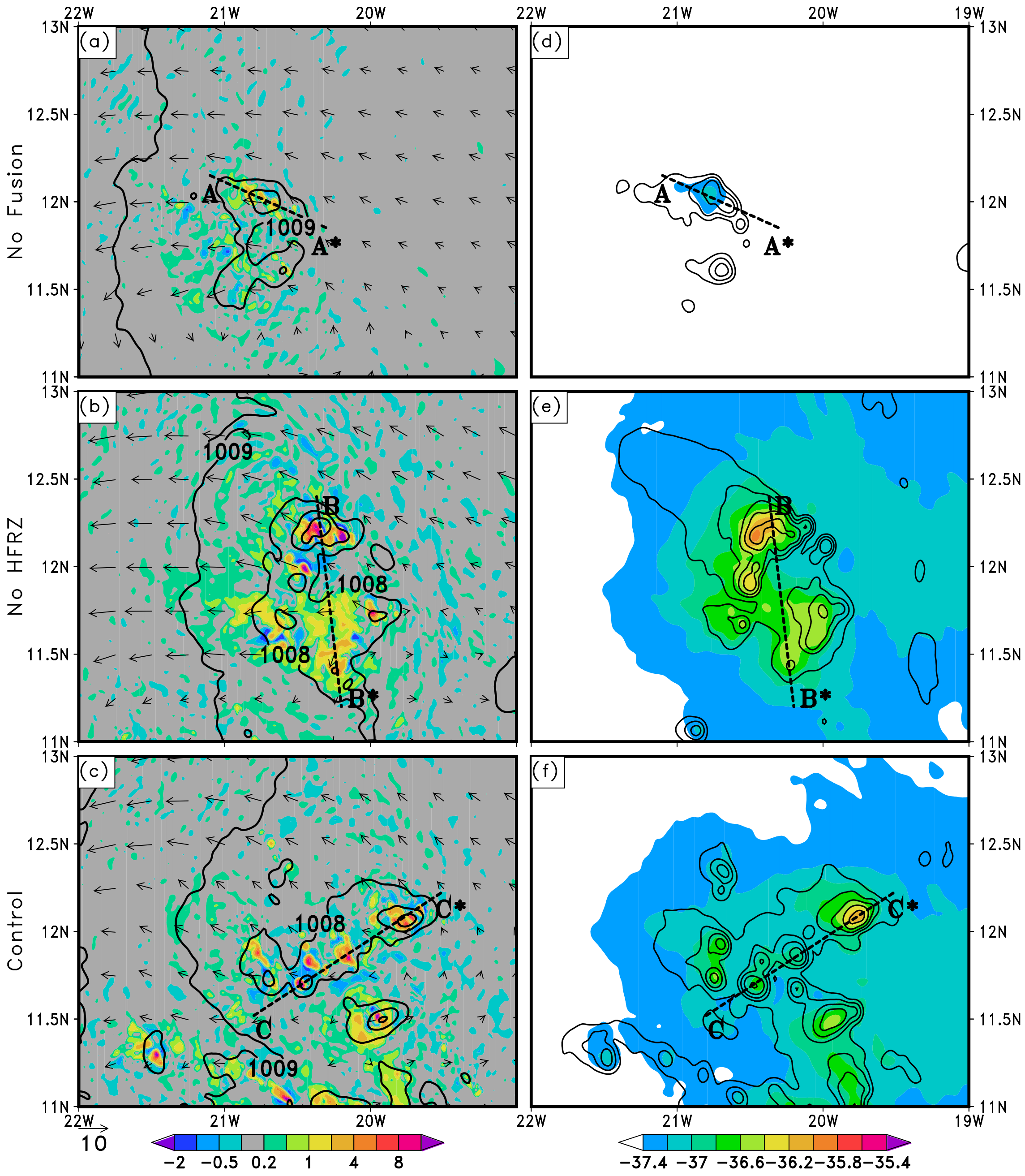

Figure 4.6: Comparisons of: (a-c) the 400-150 hPa layer-averaged vertical motion (shaded, m s^{-1}) and co-moving wind vectors (reference vector is 10 m s^{-1}) with MSLP (contoured at intervals of 1 hPa) overlaid; and (d-f) the 400-150 hPa layer-averaged temperature (shaded, °C) and cloud ice mixing ratio (contoured at 0.1, 0.25, 1, 2, 4, 10, and 20 $\times 10^{-4}$ g kg^{-1}) using a ± 30-min time average centered on 0000 UTC 12 Sep. The top, middle and bottom rows represent the simulations without fusion heating in deposition, without homogeneous freezing, and the control, respectively. The dashed lines in (a-f) show the locations of the vertical cross sections depicted in Fig. 4.7. Data from the 1-km domain are used.

field, it is obvious that the most striking difference between the simulations is related to the 400-150 hPa layer-averaged temperature field (shadings in Figs. 4.6d-f). While the majority of the 400-150 hPa layer has temperatures greater than -37°C in No HFRZ and the control (Figs. 4.6e and 4.6f), the No Fusion simulation only depicts a meso-γ region of warming that barely exceeds -37.4°C in the 400-150 hPa layer (Fig. 4.6d).

Complementing these temperature differences, it is evident that vertical motion field within the same layer is much more coherent and of larger positive magnitude when comparing No Fusion with its counterparts (cf. Figs. 4.6a-c). Both the control and No HFRZ have several convective cores with vertical motions exceeding 4 m s^{-1} in addition to CBs[1]. It is clear that these regions of enhanced positive vertical motion are collocated with warmer 400-150 hPa temperatures and increased cloud ice mixing ratios (cf. Figs. 4.6a-c and 4.6d-f). That is, these convective motions are transporting cloud water to the 400-150 hPa layer where depositional growth of cloud ice is occurring, enabling the heating of the layer via $\mathrm{L_S}$. Removing $\mathrm{L_F}$ from $\mathrm{L_S}$ (simulation No Fusion) eliminates the majority of the heating in the 400-150 hPa layer (cf. Figs. 4.6d and 4.6f), succinctly demonstrating the importance of depositional heating for the thermodynamic changes of the upper troposphere just prior to TCG.

Fig. 4.6 is supported by the cross sections created in Fig. 4.7, depicting that the No Fusion simulation has much weaker vertical motions in the 650-100 hPa layer

---

[1] We define a CB herein as a vertical motion that exceeds 8 m s^{-1}, similar to the definition used in chapter 2.

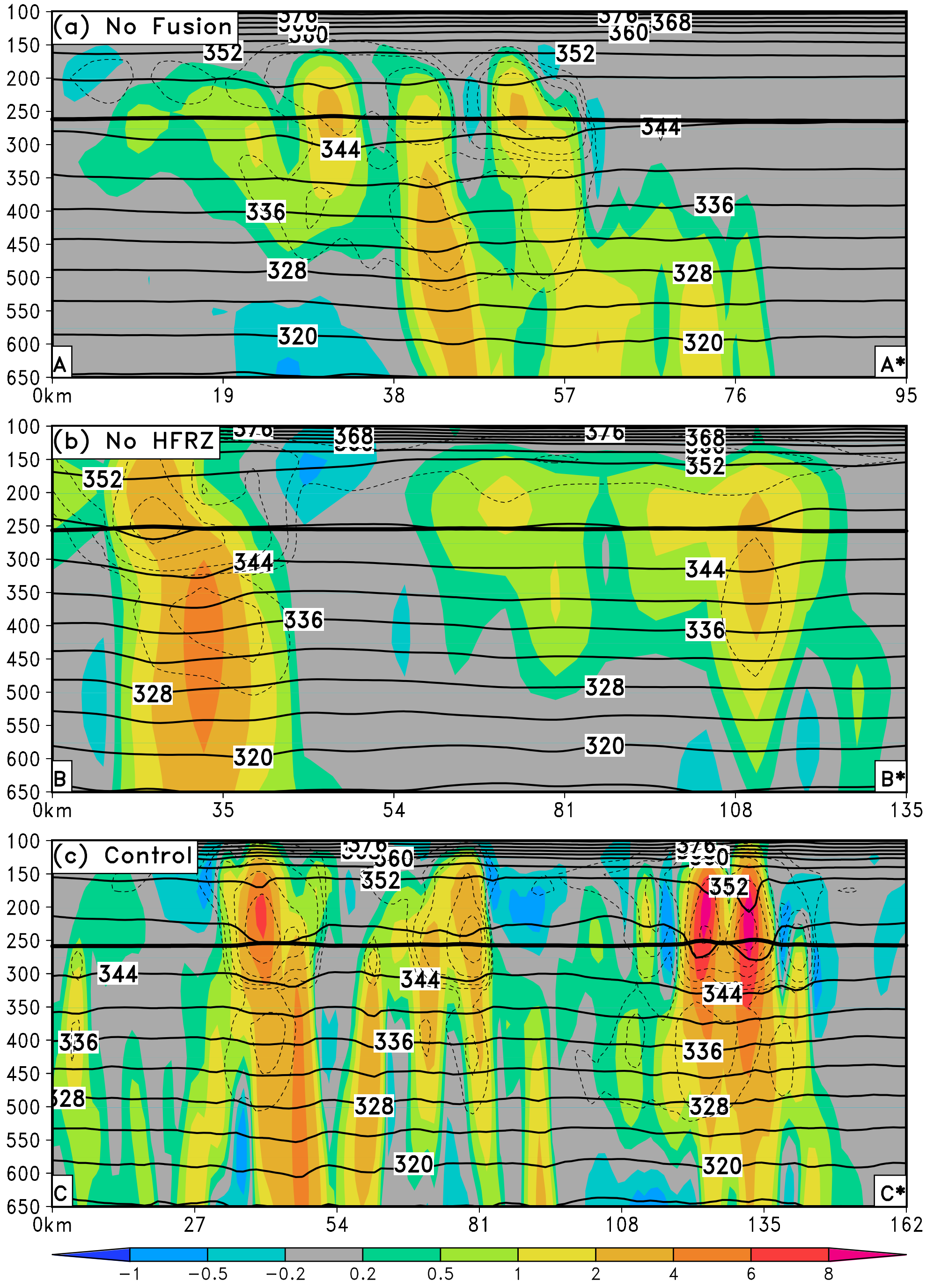

Figure 4.7: Vertical cross sections using a ± 30-min time average centered on 0000 UTC 12 Sep of vertical motion (shaded, m s^{-1}), potential temperature (contoured at intervals of 4K), and cloud ice mixing ratio (dash contours at 0.1, 0.25, 1, 2, 4, 10, and 20 $\times 10^{-4}$ g kg^{-1}) for (a) the simulation without fusion heating in deposition, (b) the simulation without homogeneous freezing, and (c) the control simulation. The cross section locations for (a-c) can be found in Fig. 4.6, respectively. The thick solid line represents the homogeneous freezing temperature (235.16K). Three volume slices were utilized in creating the cross section from the 1-km domain data set.

in comparison to the control. The level of maximum vertical motion is also lower in No Fusion when compared to the control, with maximum updrafts generally located between 325 and 225 hPa in contrast to the control whose maximum updrafts are between 275 and 125 hPa (cf. Figs. 4.7a and 4.7c). Further comparisons reveal that the No Fusion experiment has little warming of the upper troposphere as evidenced by the lack of dip in the potential temperature (θ) surfaces.

Six hours later, i.e., 12/0600, both the control and No HFRZ runs undergo TCG while the No Fusion simulation lacks a distinguishable meso-α-scale MSLP disturbance (Fig. 4.8). The control continues to show warming in the 400-150 hPa layer (cf. Figs. 4.6f and 4.8f), while little changes exist between the times for No Fusion with the exception of slight warming (cf. Figs. 4.6d and 4.8d). It is evident that the intensification of the control and No HFRZ are complemented by changes in the vertical motion field, cloud ice content and temperatures in the 400-150 hPa layer. Specifically, a coherent area of upward vertical motion exists with embedded CBs and large cloud ice mixing ratios. Further, the expansion of the warm 400-150 hPa layer temperatures occur in the presence of a more coherent storm-scale outflow (Figs. 4.8b and 4.8c). These changes can be linked to the development of a more coherent MCS in these simulations (Fig. 4.2), as the convective development enables more pronounced upward vertical motions and divergent outflow just below the tropopause. While the No Fusion experiment shows these traits, they develop on a scale localized to that of the convective development, alluding to the lack of convective growth and increased static stability in the upper troposphere.

The volume of atmosphere from 650-100 hPa above the storm centers confirms

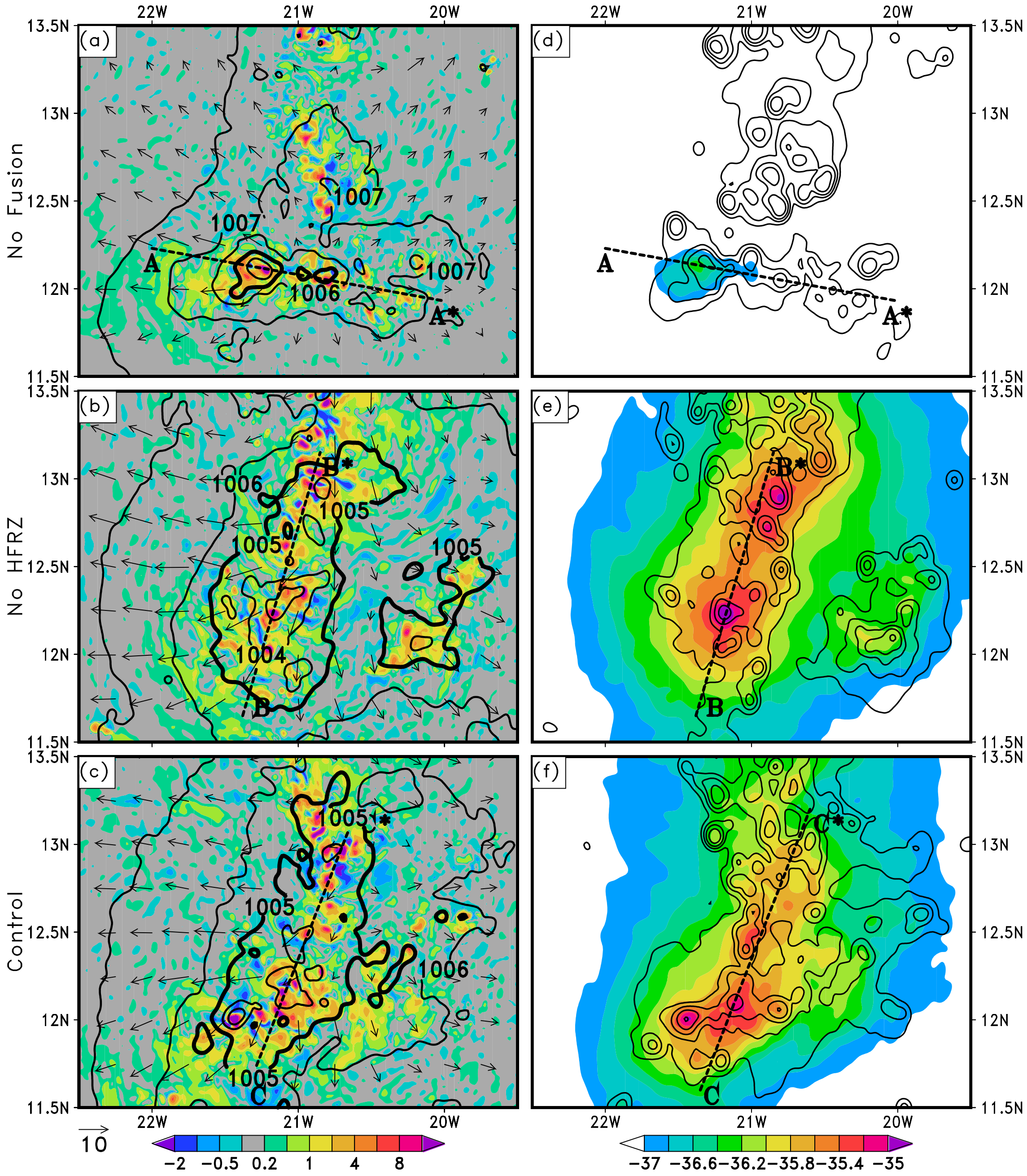

Figure 4.8: The same as Fig. 4.6, except valid at 0600 UTC 12 Sep. The bold black contour represents the spatial extent of the 1005 hPa isobar.

that significant warming occurs in the control and No HFRZ experiments, while minimal warming occurs in No Fusion (cf. Figs. 4.8 and 4.9). Noting the vertical locations of the 352K θ-surfaces in each simulation, it is clear that the No Fusion simulation shows minimal warming as the 352K θ-surface meanders around 150 hPa. In contrast, the control and no HFRZ simulations show the 352K θ-surface dip to or beyond 250 hPa, depicting a warmer upper troposphere and reduced static stability. The most pronounced thermodynamic changes in No Fusion exist at pressures at or below 250 hPa, hinting that these changes are caused by homogeneous freezing (Fig. 4.9a). It is still expected that some warming and enhanced vertical motions exist in No Fusion due to heat associated with fusion (L_F). However, these changes are less than that found in the control, whose cross section depicts much stronger vertical motions and upper troposphere with lesser static stability (Fig. 4.9c).

4.3.4 Updraft variability

Quantifying the changes in the vertical motion field, Fig. 4.10 is a count of the updrafts exceeding various thresholds within a 100 km × 100 km area around each simulation's storm center. The methodology for updraft count is as follows. First, a grid point (referred to reference point hereafter) at a particular pressure level (e.g., 650 hPa) on the 1-km domain is tested to see if the vertical motion exceeds x m s^{-1} (where x =1, 2, etc. m s^{-1}). If so, the point at the layer above the reference point (e.g., 625 hPa) is checked to see if x is exceeded at this point. This constraint is employed to ensure the updraft had vertical coherency. If the updraft

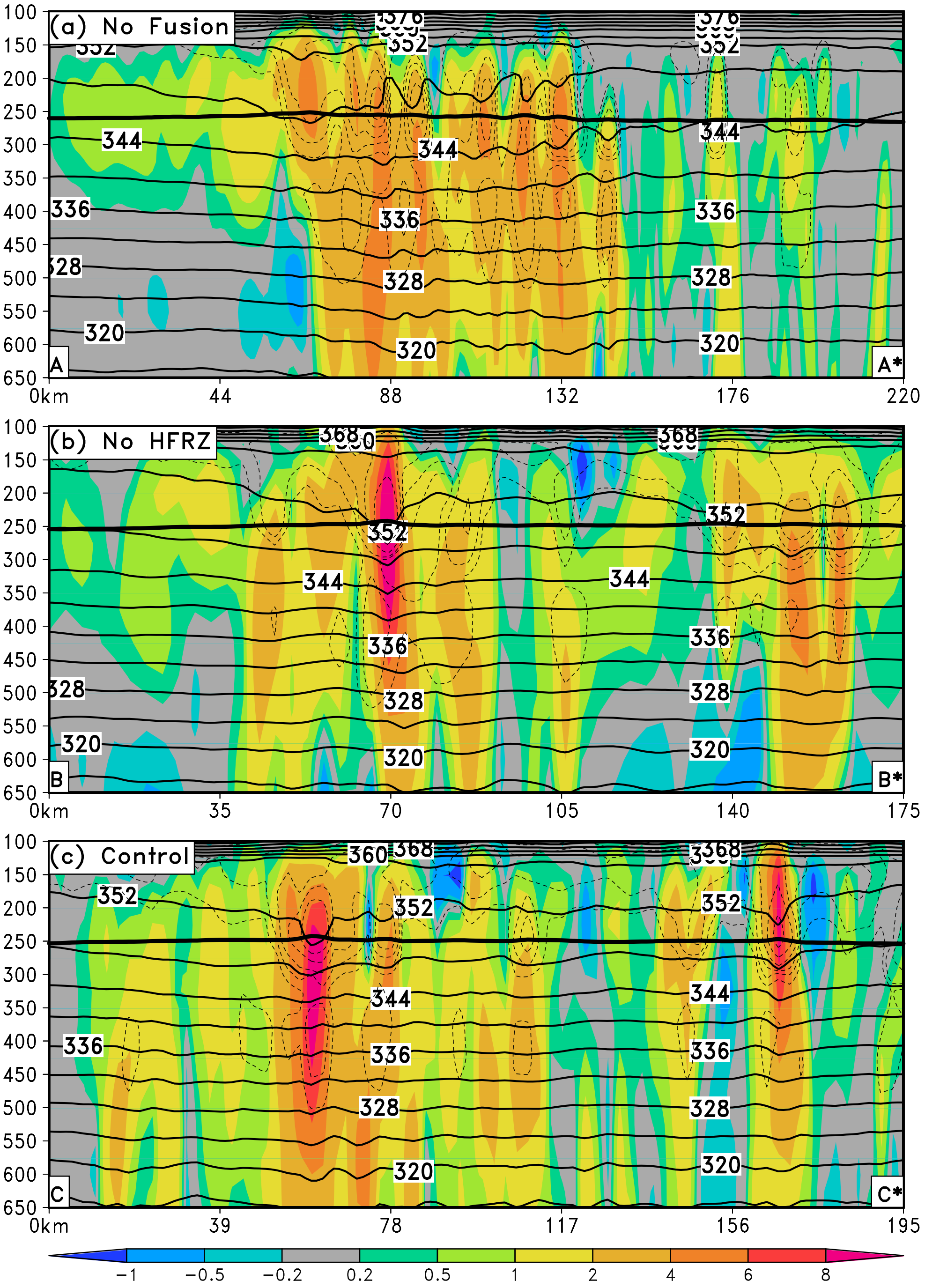

Figure 4.9: The same as Fig. 4.7, except valid at 0600 UTC 12 Sep.

demonstrates vertical coherency, then the surrounding points to the reference point, both longitudinally and latitudinally, are checked to see if they exceed $0.25 * x$. If these 4 points exceed that value, the count for the reference level is increased by 1. In short, the count of updrafts is restricted to a volume consisting of 2 km area with a minimum depth of 25 hPa, eliminating the possibility of double counting updrafts in comparison to just counting grid points whose values exceed x at each vertical level.

Focusing on the weakest updrafts first (Fig. 4.10a,b), it is clear that all simulations show counts increasing just before and at 12/0600 in the 650-150 hPa layer. The No Fusion run exhibits a large count of updrafts of at least 1.0 m s^{-1}, but the number is significantly reduced as the threshold increases to 2.0 m s^{-1} (cf. blue bars in Figs. 4.10a and 4.10b). In contrast, the control still exhibits a large number of updrafts exceeding 2.0 m s^{-1} just prior to and at 12/0600.

When investigating the stronger updrafts, the No Fusion run shows little, if any, updrafts exceeding 4.0 m s^{-1} (Fig. 4.10c). While seemingly contradictory to the cross sections discussed prior, it is worthwhile to mention that those cross-sections included a time and slice average while the counts do not invoke such a method. As a result, it is possible that the counting misses some updrafts whose maximum magnitudes are not at hourly intervals, but are instead off hour (e.g., 30 minute intervals). Regardless, it is clear that the control shows pronounced convective activity just prior to and at 12/0600, with roughly 25 updrafts exceeding 8.0 m s^{-1} at the time of TCG. In contrast, No HFRZ has a minimal number of updrafts exceeding 8.0 m s^{-1}, but instead shows updrafts exceeding this threshold at 12/0600

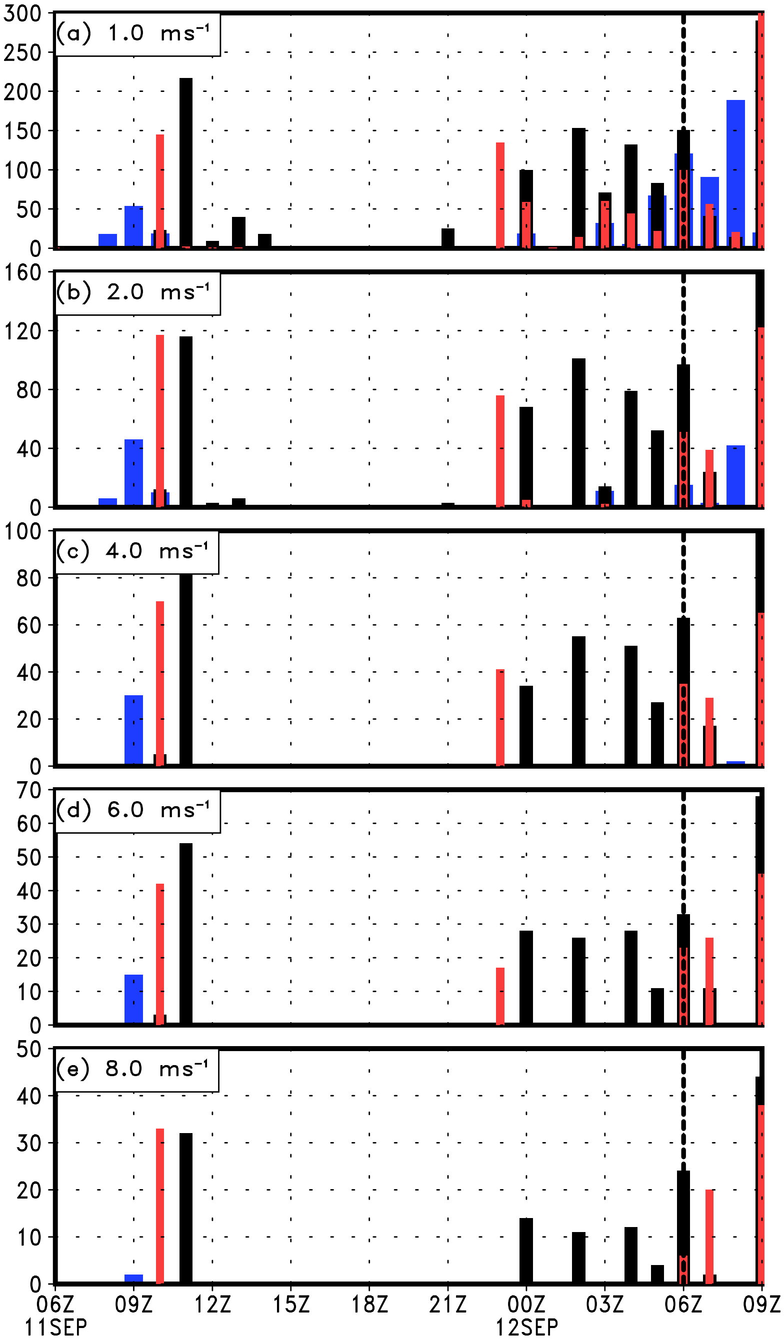

Figure 4.10: Count of updrafts exceeding various upward vertical motion thresholds summed through the 650-150 hPa layer. The number of bursts were counted in a 100 km × 100 km area surrounding each member's respective storm center. Black, blue, and red bars correspond to the counts for the control, No Fusion, and No HFRZ, respectively.

(Fig. 4.10e).

Overall, the counts of updrafts in Fig. 4.10 support the convective evolution depicted in Fig. 4.2. It is seen that both the control and No HFRZ develop a coherent MCS by 12/0600 with embedded enhanced convective activity. In contrast, the No Fusion has a much less pronounced MCS, and thus, less potent updrafts near the storm center.

4.3.5 Storm structural changes

While it is evident that the No Fusion simulation fails to undergo TCG, it has not been shown in any detail as to why this failure occurs. We previously developed a framework for the TCG of Julia which focused on the importance of: i) upper-tropospheric warming; ii) persistent storm-scale outflow (resulting from persistent deep convection within the AEW protective circulation); and iii) a shrinking L_R (which partially results from the warming of the upper troposphere). Thus, the keys to this mechanism are clearly rooted in the reduction of static stability of the upper troposphere in addition to the persistent development and amplification of deep convection.

Connecting the meaningful features together, Fig. 4.11 shows various storm attributes that are averaged using a 200 km × 200 km area around each storm's center. The first parameter of interest is the Brunt Väisälä frequency of the 400-150 hPa layer as a measure of the upper-tropospheric static stability. Clearly, the No Fusion experiment shows greater static stability when compared to its counterparts,

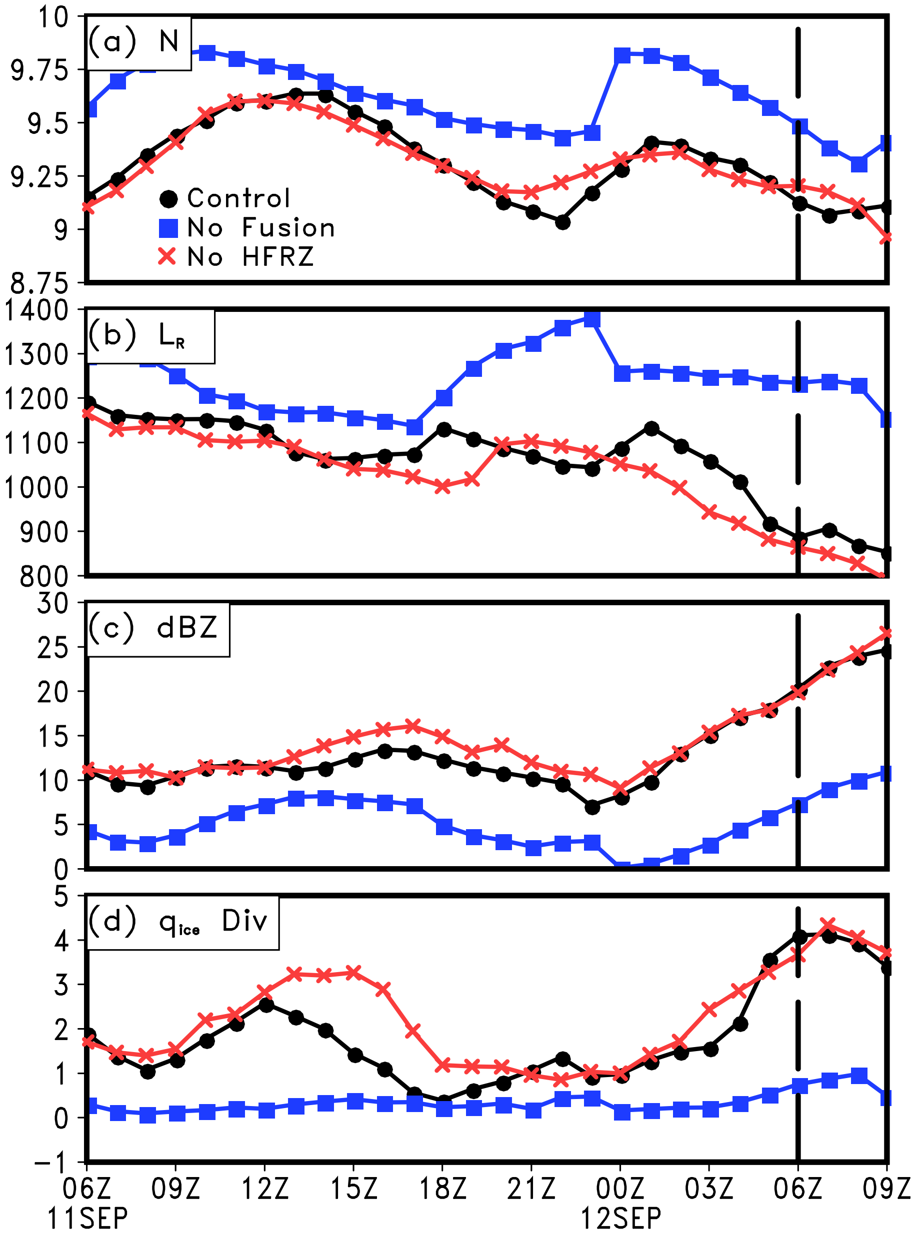

Figure 4.11: Hourly time series of the 200 km × 200 km area-averaged (a) 400-150 hPa Brunt Väisälä frequency ($\times 10^{-3}$ s^{-1}), (b) Rossby radius of deformation (km), (c) composite radar reflectivity (dBZ), and (d) 400-150 hPa layer-averaged cloud ice convergence ($\times 10^{-11}$ s^{-1}), valid from 0600 UTC 11 to 0900 UTC 12 Sep.

resulting from the upper-tropospheric warming being inhibited from to the lack of depositional heating (Fig. 4.11a). In turn, $\mathrm{L_R}$ is larger in No Fusion, requiring that the storm-scale outflow must extend further from the center of the developing disturbance in order to enable the accumulation of upper-tropospheric warming (Fig. 4.11b). However, since there is less warming of the upper troposphere, the updrafts of developing convection are accelerated less. This results in less convective development and generally weaker convection within the AEW circulation (Figs. 4.2 and 4.11c). With less and weaker convective development, the storm-scale outflow is weaker and cannot extend to $\mathrm{L_R}$ (Fig. 4.11d). With less divergent outflow and minimal convective development, the upper-tropospheric warming never becomes a meso-α-scale feature and thus, cannot induce similarly sized hydrostatic pressure falls that would enable TCG to occur (Fig. 4.3).

4.4 Summary and conclusions

This chapter investigates the role of depositional and homogeneous freezing for the TCG of Hurricane Julia (2010). Using the WRF model, sensitivity simulations are conducted by modifying the microphysics scheme and comparing the results to the control simulation created in chapter 2. The first modification made was the removal of the latent heat of fusion from the latent heat of sublimation such that the heat released during deposition was only related to the latent heat of vaporization (e.g., $\mathrm{L_S} = \mathrm{L_V}$). The second modification disabled any homogeneous freezing by setting the homogeneous freezing temperature to an unphysical value of 100K.

Results show that removing fusion heating in depositional growth inhibits the TCG of Julia. Instead of developing a coherent meso-α-scale MSLP disturbance like the control, the simulation removing fusion heating from deposition fails to develop any meaningful MSLP falls on the meso-α scale. The lack of MSLP falls results from the lack of hydrostatically induced pressure falls due to pronounced upper-tropospheric warming during TCG. This warming is all but removed in the No Fusion simulation with substantially weaker vertical motion in the 650-150 hPa layer. The intensity and spatial extent of the deep convection is also impacted when removing depositional heating as the convective updrafts are not as intense and fail to develop a coherent storm-scale outflow.

While mature TCs develop a warm core due to thermal wind balance, it is clear that the upper-tropospheric warming during TCG enables the formation of the meso-α-scale MSLP falls, and in turn, the LLV via enhanced PBL convergence. Since TCG is clearly just a transition state, it is characterized by unbalanced flow (with the exception of the large-scale AEW). This imbalance is manifested in the depositional heating that occurs in the upper troposphere as a result of convective development. With persistent deep convection within the pouch of the AEW, the upper-level warming is able to become a storm-scale feature and enable persistent MSLP falls. As clearly shown in the No Fusion simulation, the removal of depositional heating negates the series of events leading to TCG, as convective activity is less rigorous and smaller spatially.

Since our results showed that TCG is sensitive to ice microphysics, one must be careful when utilizing a complex ice microphysics scheme to investigate the development of a TD. The simple modification made in the No Fusion simulation yielded significant developmental differences for the TCG of Julia and to the structure and intensity of the simulated deep convection. Obviously, there are more uncertainties in ice microphysics than warm microphysics given the complex processes that lead to the growth and evolution of cloud ice, graupel, snow, and hail. To investigate the results found herein further, more observational studies will be needed to help quantify the magnitude of cloud ice in the upper troposphere during TCG. Further, there should be a larger focus on observational studies relating to the representativeness of cloud microphysics schemes in numerical weather models.

Chapter 5: Concluding remarks and future work

5.1 Concluding remarks

In this thesis research, we investigate the TCG of Hurricane Julia (2010) using an analysis of large-scale reanalysis data, observations, and most importantly, a plethora of cloud-resolving high-resolution WRF simulations. Given the multi-scale processes that are unresolvable via observational platforms, our work focuses on studying TCG preferentially via high-resolution numerical weather simulations. In particular, our results aid in understanding these multi-scale interactions while depicting a clear path to the development of TD Julia. The mechanisms associated with the TCG of Julia are investigated several different ways, including the use of ensemble simulations and novel statistical analyses.

Specifically, our work supplements and confirms the role of the AEW during TCG under the marsupial pouch paradigm. It is shown that mesoscale perturbations do have a predisposition for growth along the low-level AEW critical latitude and make radial entrance into the AEW pouch center via this defining characteristic of the AEW. Further, the growth of low-level cyclonic vorticity during the TCG of Julia does occur via bottom-up mechanisms, with the aggregation of two main mesovortices and invigoration via enhanced PBL convergence. The growth of the LLV that becomes TD Julia shows significant interaction with the vorticity field of the AEW, alluding to the multi-scale interactions of TCG that are difficult to observe.

Most importantly, while the wave pouch hypothesis is valid for TCG, it does not seem to be sufficient to generate an intense TC without favorable conditions in the upper outflow layer. Our research thoroughly connects upper-tropospheric thermodynamic changes to the genesis of Hurricane Julia. The influences of upper-tropospheric processes for TCG have not been investigated with much detail in previous studies. Without upper tropospheric warming during the TCG of Julia, meso-α-scale MSLP falls would have not occurred and the growth of the LLV would have been inhibited. For the development of the MSLP disturbance, persistent upper-level warming most occur on the meso-α-scale. This warming results from depositional heating through persistent deep convection that forms within the protective circulation of the AEW. As deep convection initiations and intensifies along the AEW low-level critical latitude, a coherent storm-scale outflow develops, expanding the upper-level warmth into a storm-scale feature. While this expansion occurs, the reduction in the static stability of the upper-troposphere enables the reduction of the Rossby radius of deformation. Thus, the storm-scale outflow is able to expand beyond the circumference defined by the Rossby radius of deformation and the momentum field begins to adjust to the mass field, allowing for the accumulation of pronounced upper-level warming on the meso-α-scale.

The genesis of Julia is reproduced in 20 ensemble simulations in an attempt to diagnose the key dynamical mechanisms during the transition. Such a method has been seldom used previously due to computational resource limits when trying to conduct high-resolution ensemble integrations. Our work has set the stage for future studies to investigate TCG using high-resolution model simulations by providing a reproducible method and useful statistical analyses to describe the ensemble results. It is found that the TCG of Julia is highly predictable. Even so, the seemingly minimal spread between ensemble solutions results in large dynamical and thermodynamical differences. The most obvious differences between ensemble members are related to the development of persistent deep convection near the AEW pouch center, the warming of the upper troposphere, and the reduction in the Rossby radius of deformation. These differences confirm our development hypotheses that upper-tropospheric warming is important for the TCG of Julia while also confirming that persistent deep convection is essential for TCG.

The connections between the upper-troposphere and low-level development proposed using the control simulation are validated via the ensemble through both parametric differences as well as ensemble sensitivity analyses. Using the novel approach of ensemble sensitivity analyses and EOFs in the ensemble dimension, the patterns of MSLP disagreements between ensemble members could be isolated and linked to upper-tropospheric temperature anomalies. Without investigating these patterns of ensemble differences, the ensemble would have never yielded such innovative details on the predictability of TCG.

Our work also investigates the sensitivity of TCG to ice microphysics, an untouched area of investigation in previous studies. Modifications to the microphysics scheme confirms that depositional heating of the upper troposphere is important for the TCG of Julia. Removing the latent heat of fusion from the depositional process results in a delayed and much weaker MSLP disturbance as the upper-tropospheric warming is unable to induce meaningful hydrostatic surface pressure falls. Of course, this result supports the notion that the uncertainty of numerical weather prediction is cemented in cloud microphysics. Thus, we believe that future observational campaigns should be focused on investigating upper-tropospheric warming of tropical disturbances, the cloud ice content within these disturbances, and how to improve the cloud ice microphysics of current microphysics parametrization schemes.

Overall, our work supplements the work related to the marsupial pouch paradigm with the addition of upper-tropospheric processes and the development of mesoscale features within the parent AEW. While the paradigm has provided an idealized location for genesis to occur, it lacked information on the mesoscale processes during TCG and relied on the bottom-up theory for vorticity growth of the LLV. While the growth of the LLV is essential, previous work was biased to processes of the lower and middle troposphere. Thus, our work focuses on connecting the upper-tropospheric changes into these paradigms while using novel techniques to isolate new important mechanisms for TCG within an AEW in the north Atlantic basin.

5.2 Future work

To investigate the series of events described herein further, we would like to perform this experiment again on several different TCG cases for storms in the north

Atlantic basin. While we have derived a robust theoretical construct based on the TCG of Hurricane Julia, it is worthwhile to see if the sequence of events hold true for other TCG cases within AEWs.

While still in the early stages, WRF-LETKF ensemble simulations have been conducted for the TCG of Hurricane Debby (2006). There are significant differences between the TCG of Debby and that of Julia, mainly with the strength of the parent AEW. Thus, the TCG of Hurricane Debby will assuredly provide an excellent comparison storm. Given the computational resources needed for such a study, it remains to be seen how many cases we can test our theories with. Obviously, the first step will be to derive meaningful quantitative and qualitative comparisons between Debby and Julia. Beyond these two storms, other storms of interest will be those with enhanced observational data, e.g., from observational campaigns with weather data from flights into developing disturbances.

Appendix A: WRF-LETKF System Details

The code used for the WRF-LETKF data assimilation system was developed by Miyoshi (2005) and adapted for the WRF model by Miyoshi and Kunii (2012). A four-dimensional ensemble Kalman Filter (4D-EnKF; Hunt et al. 2004) allows for the system to ingest asynchronous observations and includes spatial covariance localization with a physical distance (Miyoshi et al. 2007) as well as temporal covariance localization. The assimilation cycle in the WRF-LETKF system uses observational data produced every 6 hours (0000, 0600, 1200, and 1800 UTC) in the PREPBUFR format (Keyser 2013) from NCEP's GDAS. The PREPBUFR data are used within a 6-h window centered on the analysis time with the observation time rounded to the hour for hourly input into the 4D-LETKF (Miyoshi and Kunii 2012). WRF first-guess forecasts are integrated forward for 9-h periods, beginning 6 h prior to the analysis time. The system conducts the assimilation using the following three-dimensional prognostic variables: temperature (T), water vapor mixing ratio (q_v), pressure (P), geopotential height (ph), and wind components (u, v, w). Additionally, surface pressure (ps), 2-m temperature (T_2) and 2-m water vapor mixing ratio (q_2) are used in the observational operators. Similar localization parameters to those of Miyoshi and Kunii (2012) are used in the cycle, including a 400-km horizontal, 0.4-

ln(P) vertical, and 3-h time localization parameter. The choice for these values stems from the success of assimilating real-time observations in previous studies (Miyoshi et al. 2010). This cycle does not use adaptive covariance inflation (Miyoshi 2011), but uses a fixed, domain-constant, 20% covariance multiplicative inflation (e.g., a 1.20 inflation parameter). This global constant is used since this method closely resembles the results of the adaptive inflation technique for a 96-h cycle (see Fig. 3 of Miyoshi and Kunii 2012).

Bibliography

Ancell, B. and G. J. Hakim, 2007: Comparing ajoint– and ensemble–sensitivity analysis with applications to observation targeting. *Mon. Wea. Rev.*, **135**, 4117–4134.

Berry, G. J. and C. Thorncroft, 2005: Case study of an intense African easterly wave. *Mon. Wea. Rev.*, **133**, 752–766.

Beven, J. L. and C. L. Landsea, 2010: Tropical cyclone report Hurricane Julia (al122010) 12 – 20 September 2010. Tropical Cyclone Report, National Hurricane Center, 17 pp. Available online at `http://www.nhc.noaa.gov/pdf/TCR-AL122010_Julia.pdf`.

Bister, M. and K. A. Emanuel, 1997: The genesis of Hurricane Guillermo: TEXMEX analyses and a modeling study. *Mon. Wea. Rev.*, **125**, 2662–2682.

Braun, S. A., et al., 2013: NASAs Genesis and Rapid Intensification Processes (GRIP) field experiment. *Bull. Amer. Meteor. Soc.*, **94**, 345–363.

Burpee, R. W., 1972: The origin and structure of easterly waves in the lower troposphere of North America. *J. Atmos. Sci.*, **29**, 77–90.

Cecelski, S. F., T. Miyoshi, and D.-L. Zhang, 2014a: Genesis of Hurricane Julia (2010) within an African easterly wave: Developing and non-developing members from WRF-LETKF ensemble forecasts. *J. Atmos. Sci.*, in press.

Cecelski, S. F. and D.-L. Zhang, 2013: Genesis of Hurricane Julia (2010) within an African easterly wave: Low-level vortices and upper-level warming. *J. Atmos. Sci.*, **70**, 3799–3817.

Cecelski, S. F. and D.-L. Zhang, 2014b: Genesis of Hurricane Julia (2010) within an African easterly wave: Sensitivity analyses of WRF-LETKF ensemble forecasts. *J. Atmos. Sci.*, conditionally accepted.

Chang, E. K. M., M. Zheng, and K. Raeder, 2013: Medium–range ensemble sensitivity analysis of two extreme Pacific extratropical cyclones. *Mon. Wea. Rev.*, **141**, 211–231.

Charney, J. G. and M. E. Stern, 1962: On the stability of internal baroclinic jets in a rotating atmosphere. *J. Atmos. Sci.*, **19**, 159–172.

Chen, H. and D.-L. Zhang, 2013: On the rapid intensification of Hurricane Wilma (2005). Part II: Convective bursts and the upper-level warm core. *J. Atmos. Sci.*, **70**, 146–172.

Dudhia, J., 1989: Numerical study of convection observed during the winter monsoon experiment using a mesoscale two-dimensional model. *J. Atmos. Sci.*, **46**, 3077–3107.

Dunkerton, T. J., M. T. Montgomery, and Z. Wang, 2009: Tropical cyclogenesis in a tropical wave critical layer: Easterly waves. *Atmos. Chem. Phys.*, **9**, 5587–5646.

Emanuel, K. A., J. D. Neelin, and C. S. Bretherton, 1994: On large-scale circulations in convecting atmospheres. *Quart. J. Roy. Meteor. Soc.*, **120**, 1111–1144.

Enomoto, T., M. Hattori, T. Miyoshi, and S. Yamane, 2010: Precursory signals in analysis ensemble spread. *Geophys. Res. Lett.*, **37**, doi:10.1029/2012GL053140.

Frank, N. L., 1970: Atlantic tropical systems of 1969. *Mon. Wea. Rev.*, **98**, 307–314.

Frank, W. M., 1987: Tropical cyclone formation. *Global View of Tropical Cyclones*, R. L. Elsberry, Ed., Office of Naval Research, 53–90.

Gombos, D., R. N. Hoffman, and J. A. Hansen, 2012: Ensemble statistics for diagnosing dynamics: Tropical cyclone track forecasts sensitivities revealed by ensemble regression. *Mon. Wea. Rev.*, **140**, 2647–2669.

Gray, W. M., 1968: Global view of the origin of tropical disturbances and storms. *Mon. Wea. Rev.*, **67**, 37–69.

Harr, P. A., R. L. Elsberry, and J. C. L. Chan, 1996: Transformation of a large monsoon depression to a tropical storm during TCM–93. *Mon. Wea. Rev.*, **124**, 2625–2643.

Hawblitzel, D. P., F. Zhang, Z. Meng, and C. A. Davis, 2007: Probabilistic evaluation of the dynamics and predictability of the mesoscale convective vortex of 10-13 June 2003. *Mon. Wea. Rev.*, **135**, 1554–1563.

Hendricks, E. A., M. T. Montgomery, and C. A. Davis, 2004: The role of vortical hot towers in the formation of Tropical Cyclone Diana (1984). *J. Atmos. Sci.*, **61**, 1209–1232.

Hogsett, W. and D.-L. Zhang, 2010: Genesis of Typhoon Chanchu (2006) from a westerly wind burst associated with the MJO. Part I: Evolution of a vertically tilted precursor vortex. *J. Atmos. Sci.*, **67**, 3774–3792.

Hong, S.-Y., J. Dudhia, and S.-H. Chen, 2004: A revised approach to ice microphysical processes for the bulk parameterization of clouds and precipitation. *Mon. Wea. Rev.*, **132**, 103–120.

Hopsch, S. B., C. D. Thorncroft, and K. R. Tyle, 2010: Analysis of African easterly wave structures and their role in influencing tropical cyclogenesis. *Mon. Wea. Rev.*, **138**, 1399–1419.

Houze, R. A., W.-C. Lee, and M. M. Bell, 2009: Convective contribution to the genesis of Hurricane Ophelia (2005). *Mon. Wea. Rev.*, **137**, 2778–2800.

Hoxit, L. R., C. Chappell, and J. Fritch, 1976: Formation of mesolows or pressure troughs in advance of cumulonimbus clouds. *Mon. Wea. Rev.*, **104**, 1419–1428.

Hunt, B. R., E. J. Kostelich, and I. Szunyogh, 2007: Efficient data assimilation for spatiotemporal chaos: A Local Ensemble Transform Kalman Filter. *Physica D*, **230**, 112–126.

Hunt, B. R., et al., 2004: Four-dimensional ensemble Kalman filtering. *Tellus*, **56A**, 273–277.

Kain, J. S., 2004: The Kain–Fritsch convective parameterization: An update. *J. Appl. Meteor.*, **43**, 170–181.

Kain, J. S. and J. M. Fritsch, 1990: A one-dimensional entraining/detraining plume model and its application in convective parameterization. *J. Atmos. Sci.*, **47**, 2784–2812.

Karyampudi, V. M. and H. F. Pierce, 2002: Synoptic-scale influence of the Saharan air layer on tropical cyclogenesis over the eastern Atlantic. *Mon. Wea. Rev.*, **130**, 3100–3128.

Keyser, D., 2013: PREPBUFR processing at NCEP. Tech. rep., National Centers for Environmental Prediction. Available online at `http://www.emc.ncep.noaa.gov/mmb/data_processing/prepbufr.doc/document.htm`.

Kieu, C. Q. and D.-L. Zhang, 2009: Genesis of Tropical Storm Eugene (2005) from merging vortices associated with ITCZ breakdowns. Part II: Roles of vortex merger and ambient potential vorticity. *J. Atmos. Sci.*, **66**, 1980–1996.

Komaromi, W., 2012: An investigation of composite dropsonde profiles for developing and non-developing tropical waves during the 2010 PREDICT field campaign. *J. Atmos. Sci.*, doi:10.1175/JAS-D-12-052.1.

Li, T. and B. Fu, 2006a: Tropical cyclogenesis associated with Rossby wave energy dispersion of a preexisting typhoon. Part I: Satellite data and analyses. *J. Atmos. Sci.*, **63**, 1377–1389.

Li, T., X. Ge, B. Wang, and Y. Zhu, 2006b: Tropical cyclogenesis associated with Rossby wave energy dispersion of a preexisting typhoon. Part II: Numerical simulations. *J. Atmos. Sci.*, **63**, 1390–1409.

Lord, S. J., H. E. Willoughby, and J. M. Piotrowicz, 1984: Role of a parameterized ice-phase microphysics in an axisymmetric nonhydrostatic tropical cyclone model. *J. Atmos. Sci.*, **41**, 2836–2848.

McFarquhar, G. M., G. Heymsfield, R. Hood, J. Dudhia, J. B. Halverson, and F. Marks, 2006: Factors affecting the evolution of Hurricane Erin (2001) and the distributions of hydrometeors: Role of microphysical processes. *J. Atmos. Sci.*, **63**, 127–150.

Miyoshi, T., 2005: Ensemble Kalman filter experiments with a primitive-equation global model. Ph.D. thesis, University of Maryland, 197 pp.

Miyoshi, T., 2011: The Gaussian approach to adaptive covariance inflation and its implementation with the Local Ensemble Transform Kalman Filter. *Mon. Wea. Rev.*, **139**, 1519–1535.

Miyoshi, T. and M. Kunii, 2012: The Local Ensemble Transform Kalman Filter with the weather research and forecasting model: Experiments with real observations. *Pure Appl. Geophys.*, **169**, 321–333.

Miyoshi, T., Y. Sato, and T. Kadowaki, 2010: Ensemble Kalman filter and 4D-Var inter-comparison with the Japanese operational global analysis and prediction system. *Mon. Wea. Rev.*, **138**, 2846–2866.

Miyoshi, T., S. Yamane, and T. Enomoto, 2007: Localizing the error covariance by physical distances within a Local Ensemble Transform Kalman Filter (LETKF). *SOLA*, **3**, 89–92.

Mlawer, E. J., S. J. Taubman, P. D. Brown, M. J. Iacono, and S. A. Clough, 1997: Radiative transfer for inhomogeneous atmospheres: RRTM, a validated correlated-k model for the longwave. *J. Geophys. Res.*, **102**, 16 663–16 682.

Montgomery, M. T., L. L. Lussier III, R. W. Moore, and Z. Wang, 2010: The genesis of Typhoon Nuri as observed during the Tropical Cyclone Structure 2008 (TCS–08) field experiment – Part 1: The role of the easterly wave critical layer. *Atmos. Chem. Phys.*, **10**, 9879–9900.

Montgomery, M. T., M. E. Nicholls, T. A. Cram, and A. B. Saunders, 2006: A vortical hot tower route to tropical cyclogenesis. *J. Atmos. Sci.*, **63**, 355–386.

Montgomery, M. T., et al., 2012: The Pre–Depression Investigation of Cloud–systems in the Tropics (PREDICT) experiment: Scientific basis, new analysis tools and some first results. *Bull. Amer. Meteor. Soc.*, **93**, 153–172.

Noh, Y. W., W. G. Cheon, S. Y. Hong, and S. Raasch, 2003: Improvement of the k-profile model for the planetary boundary layer based on large eddy simulation data. *Bound. -Layer Meteor.*, **9**, 401–427.

Nolan, D. S., 2007: What is the trigger for tropical cyclogenesis? *Aust. Meteor. Mag.*, **56**, 241–266.

Olson, D. A., N. W. Junker, and B. Korty, 1995: Evaluation of 33 years of quantitative precipitation forecasting at the NMC. *Wea. Forecasting*, **10**, 498–511.

Reynolds, R. W., T. M. Smith, C. Lui, D. B. Chelton, K. S. Casey, and M. G. Schlax, 2007: Daily high-resolution blended analyses for sea surface temperature. *J. Climate*, **20**, 5473–5496.

Riehl, H. and J. S. Malkus, 1958: On the heat balance in the equatorial trough zone. *Geophysica*, **6**, 503–538.

Ritchie, E. A. and G. J. Holland, 1997: Scale interactions during the formation of Typhoon Irving. *Mon. Wea. Rev.*, **125**, 1377–1396.

Rogers, R. R. and M. K. Yau, 1989: *A Short Course in Cloud Physics.* 3d ed., Butterworth-Heinemann, 290 pp.

Schreck, C. J., J. Molinari, and A. Aiyyer, 2012: A global view of equatorial waves and tropical cyclogenesis. *Mon. Wea. Rev.*, **140**, 774–788.

Simpson, J., J. B. Halverson, B. S. Ferrier, W. A. Petersen, R. H. Simpson, R. Blakeslee, and S. L. Durden, 1998: On the role of "hot towers" in tropical cyclone formation. *Meteor. Atmos. Phys.*, **67**, 15–35.

Sippel, J. A., J. W. Nielsen-Gammon, and S. E. Allen, 2006: The multiple–vortex nature of tropical cyclogenesis. *Mon. Wea. Rev.*, **134**, 1796–1814.

Sippel, J. A. and F. Zhang, 2008: The probabilistic analysis of the dynamics and predictability of tropical cyclogenesis. *J. Atmos. Sci.*, **65**, 3440–3459.

Skamarock, W. C., J. B. Klemp, J. Dudhia, D. O. Gill, D. M. Barker, W. Wang, and J. G. Powers, 2005: A description of the advanced research WRF version 2. NCAR.

Snyder, A. D., Z. Pu, and Y. Zhu, 2010: Tracking and verification of east Atlantic tropical cyclone genesis in the NCEP global ensemble: Case studies during the NASA African monsoon multidisciplinary analyses. *Wea. Forecasting*, **25**, 1397–1411.

Thompson, G., P. R. Field, R. M. Rasmussen, and W. D. Hall, 2008: Explicit forecasts of winter precipitation using an improved bulk microphysics scheme. Part II: Implementation of a new snow parameterization. *Mon. Wea. Rev.*, **136**, 5095–5115.

Thompson, G., R. M. Rasmussen, and K. Manning, 2004: Explicit forecasts of winter precipitation using an improved bulk microphysics scheme. Part I: Description and sensitivity analysis. *Mon. Wea. Rev.*, **132**, 519–542.

Thorncroft, C. and K. Hodges, 2000: African easterly wave variability and its relationship to Atlantic tropical cyclone activity. *J. Climate*, **14**, 1166–1179.

Torn, R. D. and D. Cook, 2013: The role of vortex and environment errors in the genesis forecasts of hurricanes Danielle and Karl (2010). *Mon. Wea. Rev.*, **136**, 232–251.

Torn, R. D. and G. J. Hakim, 2008: Ensemble–based sensitivity analysis. *Mon. Wea. Rev.*, **141**, 663–677.

Ventrice, M. J., C. D. Thorncroft, and M. A. Janiga, 2012a: Atlantic tropical cyclogenesis: A three-way interaction between an African easterly wave, diurnally varying convection, and a convectively coupled atmospheric Kelvin wave. *Mon. Wea. Rev.*, **140**, 1108–1124.

Vizy, E. K. and K. H. Cook, 2009: Tropical storm development from African easterly waves in the eastern Atlantic: A comparison of two successive waves using a regional model as part of NASA AMMA 2006. *J. Atmos. Sci.*, **66**, 3313–3334.

Wang, Y., 2002: An explicit simulation of tropical cyclones with a triply nested movable mesh primative equation model: TCM3. Part II: model refinements and sensitivity to cloud microphysics parameterization. *Mon. Wea. Rev.*, **130**, 3022–3036.

Wang, Z., 2012: Thermodynamic aspects of tropical cyclone formation. *J. Atmos. Sci.*, **69**, 2433–2451.

Wang, Z., M. T. Montgomery, and T. J. Dunkerton, 2010a: Genesis of pre-Hurricane Felix (2007). Part I: The role of the easterly wave critical layer. *J. Atmos. Sci.*, **67**, 1711–1729.

Wang, Z., M. T. Montgomery, and T. J. Dunkerton, 2010b: Genesis of pre-Hurricane Felix (2007). Part II: Warm core formation, precipitation evolution, and predictability. *J. Atmos. Sci.*, **67**, 1730–1744.

Wang, Z., M. T. Montgomery, and C. Fritz, 2012: A first look at the structure of the wave pouch during the 2009 PREDICT-GRIP dry runs over the Atlantic. *Mon. Wea. Rev.*, **140**, 1144–1163.

Zhang, D.-L. and N. Bao, 1996: Oceanic cyclogenesis as induced by a mesoscale convective system moving offshore. Part II: Genesis and thermodynamic transformation. *Mon. Wea. Rev.*, **124**, 2206–2226.

Zhang, D.-L. and J. M. Fritsch, 1987: Numerical simulation of the meso-beta-scale structure and evolution of the 1977 Johnstown flood. Part II: Inertially stable warm-core vortex and the mesoscale convective complex. *J. Atmos. Sci.*, **44**, 2593–2612.

Zhang, D.-L. and L. Zhu, 2012: Roles of upper-level processes in tropical cyclogenesis. *Geophys. Res. Lett.*, **39**, L17 804.

Zheng, M., E. K. M. Chang, and B. A. Colle, 2013: Ensemble sensitivity tools for assessing extratropical cyclone intensity and track predictability. *Wea. Forecasting*, **28**, 1133–1156.

Zhu, T. and D.-L. Zhang, 2006: Numerical simulation of Hurricane Bonnie (1998). Part II: Sensitivity to varying cloud microphysical processes. *J. Atmos. Sci.*, **63**, 109–126.